

# Printing of functional materials in 2D and 3D structures

Halevi, Oded

2019

Halevi, O. (2019). Printing of functional materials in 2D and 3D structures. Doctoral thesis, Nanyang Technological University, Singapore.

<https://hdl.handle.net/10356/142937>

<https://doi.org/10.32657/10356/142937>

---

This work is licensed under a Creative Commons Attribution-NonCommercial 4.0 International License (CC BY-NC 4.0).

*Downloaded on 13 Mar 2024 17:33:58 SGT*

## Statement of Originality

I hereby certify that the work embodied in this thesis is the result of original research, is free of plagiarised materials, and has not been submitted for a higher degree to any other University or Institution, except for Nanyang Technological University (NTU), Singapore and the Hebrew University of Jerusalem (HUI), Israel, under the NTU-HUI joint PhD program.

.... 08/07/2020 ....  
Date

  
.....  
Oded Halevi

## Supervisor Declaration Statement

I have reviewed the content and presentation style of this thesis and declare it is free of plagiarism and of sufficient grammatical clarity to be examined. To the best of my knowledge, the research and writing are those of the candidate except as acknowledged in the Author Attribution Statement. I confirm that the investigations were conducted in accord with the ethics policies and integrity standards of Nanyang Technological University and that the research data are presented honestly and without prejudice.

.... 08/07/2020 ....  
Date



.....  
Prof. Lee Pooi See



.....  
Prof. Shlomo Magdassi

## Authorship Attribution Statement

This thesis contains materials from 4 papers published in the following peer-reviewed journals:

Chapter 1 is published as:

Halevi O., Tan J.M.R., Lee P.S., Magdassi S. **Hydrolytically Stable MOF in 3D-Printed Structures**. Advanced Sustainable Systems 2, 1700150 (2018).

The contributions of the co-authors are as follows:

- Prof. S. Magdassi and Prof. P.S. Lee supervised the work on this project.
- I developed the printing methodology, the ink formulation, and performed the MOF synthesis, adsorption measurements, analysis and characterization.
- I wrote the manuscript drafts.
- Dr. J.M.R. Tan contributed in performing and the SEM measurements.

Chapter 2 is published as:

Halevi O., Chen T.Y., Lee P.S., Magdassi S., Hriljac J.A. **Nuclear wastewater decontamination by 3D-Printed hierarchical zeolite monoliths**. RSC Advances 10, 5766 (2020).

The contributions of the co-authors are as follows:

- O. Halevi and T.Y. Chen are equal contributors.
- I developed the printing methodology, the ink formulation, and performed the characterization of the printed materials and structures by Powder-XRD, BET and SEM.
- My work was done under the supervision of Prof. S. Magdassi and Prof. P.S. Lee.
- Dr. T.Y. Chen performed the zeolites synthesis, ion-exchange measurements, and the Powder-XRD after ion exchange, under the supervision of Prof. J.A. Hriljac.



Chapter 3 is published as:

Halevi O., Chen J., Thangavel G., Morris S. A., Ben-Uliel T., Tichler Y., Lee P.S. and Magdassi S. **Synthesis through 3D Printing: Formation of 3D Coordination Polymers**. RSC Advances 10, 14812 (2020).

The contributions of the co-authors are as follows:

- I developed the printing methodology, ink preparation, monomer synthesis, coordination polymer preparation and performed the characterization of the monomer and the printed coordination polymer.
- My work was done under the supervision of Prof. S. Magdassi and Prof. P.S. Lee.
- Dr. J. Chen contributed in performing and analyzing the EDX and XPS measurements and in discussions, under the supervision of Prof. P.S. Lee.
- Dr. G. Thangavel contributed in performing and analyzing the NMR measurements and in discussions, under the supervision of Prof. P.S. Lee.
- Dr. S. A. Morris contributed in measuring the single crystal X-ray diffraction and solving the single crystal structure.
- T. Ben-Uliel contributed in performing the Raman measurements, under the supervision of Prof. Y. Tichler.

Chapter 4 is published as:

Halevi O., Jiang H., Kloc C., Magdassi S. **Additive manufacturing of micrometric crystallization vessels and single crystals**. Scientific Reports 6, 36786 (2016).

The contributions of the co-authors are as follows:

- I developed the printing and crystallization methodology, ink preparation, and performed the characterization of the printed crystals.
- Dr. H. Jiang contributed in fabricating and characterizing the OFET.
- All the work was performed under the supervision of Prof. S. Magdassi and Prof. C. Kloc.

... 08/07/2020 ...  
Date

  
.....  
Oded Halevi

# **Printing of Functional Materials in 2D and 3D Structures**

Thesis for the degree of "Doctor of Philosophy"

**By Oded Halevi**

Submitted to the Senate of the Hebrew University of Jerusalem

September 2019



# **Printing of Functional Materials in 2D and 3D Structures**

Thesis for the degree of "Doctor of Philosophy"

**By Oded Halevi**

Submitted to the Senate of the Hebrew University of Jerusalem

September 2019



This work was carried out under the supervision of:

**Prof. Shlomo Magdassi (HUJ Israel) and Prof. Pooi See Lee (NTU Singapore)**



## Abstract

In recent years, controlled deposition of functional materials has become a highly investigated field. Employing either two dimensional (2D) or three dimensional (3D) printing, many functional materials can be utilized for various applications once defined patterns or structures can be formed. From the sub-nano to the macroscale, scientists and engineers have been exploring processes and technologies that may enable the formation of such structures. In many cases, functionalities and enhanced properties are gained once a certain degree of order is achieved; for example, in single crystals, self-assembled layers and three dimensional molecular networks. This is due to various reasons, such as the intramolecular interactions, morphology, or the given functionality of a certain macro-design.

One group of functional materials exhibit porosity, which usually consists of sub-nanometric and nanometric voids within the material. This feature leads to high surface areas, which usually results in an adsorptive behavior. Porous materials are being utilized nowadays in many fields such as gas storage and purification, water remediation, filtration, ion-exchange and catalysis. Two examples for such materials are Metal Organic Frameworks (MOFs) and Zeolites.

MOFs are a subgroup of the coordination polymers (CPs) family. These are molecular nets with metal ions as nodes and organic molecules as linkers. Despite their extensive investigations in the past twenty years, the utilization of MOFs for industrial and commercial applications is scarce, due to physical and chemical limitations. On the other hand, zeolites, which are composed of aluminosilicate networks incorporated by cations, exhibit higher chemical and physical stability, and thus are being used for various commercial and industrial applications. Nevertheless, their powder form hinders their compatibility for certain purposes. In this work we demonstrate the enhancing effect of confining the MOFs and zeolites in 3D-printed structures, which assists to overcome the materials' limitations, towards a more extended utilization of these two extraordinary groups of materials. Moreover, once the MOFs were successfully printed, the printing process was further



exploited not just to form MOF-embedded structures, but also to synthesize all-CP standalone 3D objects.

Zeolites and MOFs are usually crystalline, and exhibit high periodic molecular order, which leads to the constant and defined pores sizes and contributes to their functionality. Many materials other than MOFs and zeolites also exhibit unique and enhanced properties when in the form of single crystals. An example for such group of functional materials is the small-molecules organic semiconductors. These materials demonstrate higher semiconducting performance once arranged as single crystals instead of micro- and nanoparticles.

The crystallization process usually requires time, as well as a stable and steady environment. Therefore, trying to develop a printing method for crystallization of materials in a controlled manner is a serious challenge, since printing is usually a rapid process that includes continuous movement. In this work we combined the two processes, and developed a method for inkjet-printing of single crystals at specific locations. The chosen representative compound was the organic semiconducting perylene.

One of the common denominators of the various chapters in this work is that by relying on chemical principles such as synthesis rules, phase separation considerations and crystallization processes, printing process control was successfully gained over the deposition and the arrangement of the materials in the confined structures. This in turn enhanced the performance of the materials and overcame their limitations, towards better and further utilization.

This research is expected to contribute in two main ways: (1) it demonstrates how taking advantage of basic chemical principles, such as hydrophilic-hydrophobic interactions and crystallization, can help overcome limitations of functional materials and increase their potential utilization. (2) This work also contributes to the overall effort of advanced manufacturing, as it sets clear examples as for how printing technologies can be utilized to enhance the applicability of functional materials and fabrication of functional devices.

The results of this work were published as three peer-reviewed articles, and an additional article has been submitted for publication.

## Letter of Contribution

To whom it may concern,

I hereby declare my following contributions in the PhD thesis, in which the results are presented in four chapters, three of them are published papers, and one has been submitted.

Chapter 1: ***Hydrolytically Stable MOF in 3D-Printed Structures, published.***

Halevi O., Tan J.M.R., Lee P.S., Magdassi S. Hydrolytically Stable MOF in 3D-Printed Structures. *Advanced Sustainable Systems* **2**, 1700150 (2018).

I developed the printing methodology, the ink formulation, and performed the MOF synthesis, adsorption measurements, analysis and characterization.

Dr. J.M.R. Tan contributed in performing the SEM measurements.

The work was performed under the supervision of Prof. S. Magdassi and Prof. P.S. Lee.

Chapter 2: ***Nuclear Wastewater Decontamination by 3D-Printed Hierarchical Zeolite Monoliths, published.***

Halevi O., Chen T.Y., Lee P.S., Magdassi S., Hriliac J.A. Nuclear wastewater decontamination by 3D-Printed hierarchical zeolite monoliths. *RSC Advances* **10**, 5766 (2020).

Equal contributors - O. Halevi and T.Y. Chen.

I developed the printing methodology, the ink formulation, and performed the characterization of the printed materials and structures by Powder-XRD, BET and SEM, under supervision of Prof. S. Magdassi and Prof. P.S. Lee.

The zeolites synthesis, ion-exchange measurements, and the Powder-XRD after ion-exchange, was performed by Dr. T.Y. Chen under the supervision of Prof. J.A. Hriliac.

Chapter 3: ***Synthesis through 3D Printing: Formation of 3D Coordination Polymers.***

By O. Halevi, J. Chen, G. Thangavel, S. A. Morris, T. Ben-Uliel, Y. Tichler, P.S. Lee and S. Magdassi; **Submitted.**

I developed the printing methodology, ink preparation, monomer synthesis, coordination polymer preparation and performed the characterization of the monomer and the printed coordination polymer.

Dr. J. Chen contributed in performing the EDX measurements and in discussions, under the supervision of Prof. P.S. Lee.

Dr. G. Thangavel contributed in performing the NMR measurements and in discussions, under the supervision of Prof. P.S. Lee.

Dr. S. A. Morris contributed in measuring the single crystal X-ray diffraction and solving the single crystal structure.

T. Ben-Uliel contributed in performing the Raman measurements, under the supervision of Prof. Y. Tichler. All the work was performed under the supervision of Prof. S. Magdassi and Prof. P.S. Lee.

Chapter 4: ***Additive Manufacturing of Micrometric Crystallization Vessels and Single Crystals***, published.

Halevi O., Jiang H., Kloc C., Magdassi S. Additive manufacturing of micrometric crystallization vessels and single crystals. *Scientific Reports* **6**, 36786 (2016).

I developed the printing and crystallization methodology, ink preparation, and performed the characterization of the printed crystals.

Dr. H. Jiang contributed in fabricating and characterizing the OFET. All the work was performed under the supervision of Prof. S. Magdassi and Prof. C. Kloc.

## Contents

<b>1. Introduction</b>	<b>3</b>
<b>1.1. Printing and Additive Manufacturing</b>	<b>3</b>
1.1.1. Digital Light Processing (DLP)	3
1.1.2. Inkjet Printing	4
<b>1.2. Functional Materials</b>	<b>5</b>
1.2.1. Porous Materials	5
1.2.1.1. Zeolites	5
1.2.1.2. MOFs and Other Coordination Polymers	6
1.2.2. Small-Molecules Organic Semiconductors	7
<b>1.3. Chemical Control Over the Formation of Function-Enhancing Confined Structures</b>	<b>8</b>
1.3.1. Organic-Inorganic Porous Composites	8
1.3.1.1. Controlled Polymer Porosity	9
1.3.1.1.1. Effect of the Intensity of the Initiating Energy Source	9
1.3.1.1.2. Effect of the Porogenic Solvent	9
1.3.1.1.3. Effect of the Cross-Linker	10
1.3.2. Single Crystals of Organic Semiconductors	11
<b>1.4. Printing of Functional Materials in 2D and 3D Structures</b>	<b>12</b>
<b>1.5. Research Objectives</b>	<b>12</b>
<b>2. Results</b>	<b>15</b>
2.1. Chapter 1: Hydrolytically Stable MOF in 3D-Printed Structures	17
2.2. Chapter 2: Nuclear Wastewater Decontamination by 3D-Printed Hierarchical Zeolite Monoliths	35
2.3. Chapter 3: Synthesis Through 3D Printing: Formation of 3D Coordination Polymers	53
2.4. Chapter 4: Additive Manufacturing of Micrometric Crystallization Vessels and Single Crystals	73
<b>3. Discussion and Conclusions</b>	<b>87</b>
3.1. Discussion and Summary	87
3.2. Insights and Perspectives	90
<b>4. References</b>	<b>95</b>
<b>5. Appendices</b>	<b>101</b>
5.1. Appendix I - 3D Printing of Thermo- and Solvatochromic Composite Material Based on a Cu(II)-Thymine Coordination Polymer with Moisture Sensing Capabilities	103



## **1. Introduction**

### **1.1. Printing and Additive Manufacturing**

Additive manufacturing, commonly known as three dimensional (3D) printing, was introduced for the first time in the 1980's.<sup>1</sup> Now it has become a significant tool for prototyping and custom manufacturing. It is considered as the third industrial revolution,<sup>2</sup> and now is also taking part in the Industry 4.0 revolution. Although there are several different 3D-printing methods currently available in the market, the basic principle behind them is the same. First, a 3D computer model is generated and uploaded into the printer. Then the printer's software slices the 3D model into many 2D layers. Following this, the desired material is deposited layer over layer, according to the sliced model, until the complete 3D object is formed (Figure 1).<sup>3</sup> The most widely used technique is Fused Deposition Modeling (FDM), in which a polymer filament is deposited through a heating element onto a stage.<sup>4</sup> The heating element temperature is set as the melting temperature of the polymer. As a result, the polymer is melted just before its deposition, and then solidifies again once it touches the substrates. By depositing the polymer layer over layer, a 3D structure is formed. Another printing method is Write-on-Demand (WOD),<sup>5</sup> which is basically an extruder that deposits layers of the selected material. Each layer is solidified before the following layer is added. It can be due to solvent evaporation, UV-polymerization, heating, or due to the non-Newtonian behavior of the printed material. The continuous extrusion of the solid layers one on top of the other generates the desired 3D model. Here are two printing methods that have been utilized in this work.

#### **1.1.1. Digital Light Processing (DLP)**

DLP printing was developed from the stereolithography (SLA) 3D-printers.<sup>6</sup> The basic principle of this technique is the formation of solid polymers from liquid monomers by UV-polymerization. A bath of monomers is placed on top of a UV-light source. Then polymerization of each layer takes place, according to the sliced computer 3D-model. (Figure 1b). The main difference between DLP and SLA is the light source. While SLA uses a laser to polymerize each voxel (a three dimensional pixel) one after the other, DLP's light source is a projector coupled to a set of reflecting mirrors that can polymerize a whole layer at the same

time. While SLA enables higher resolution, the main advantage of the DLP is the printing speed, which is significantly increased.

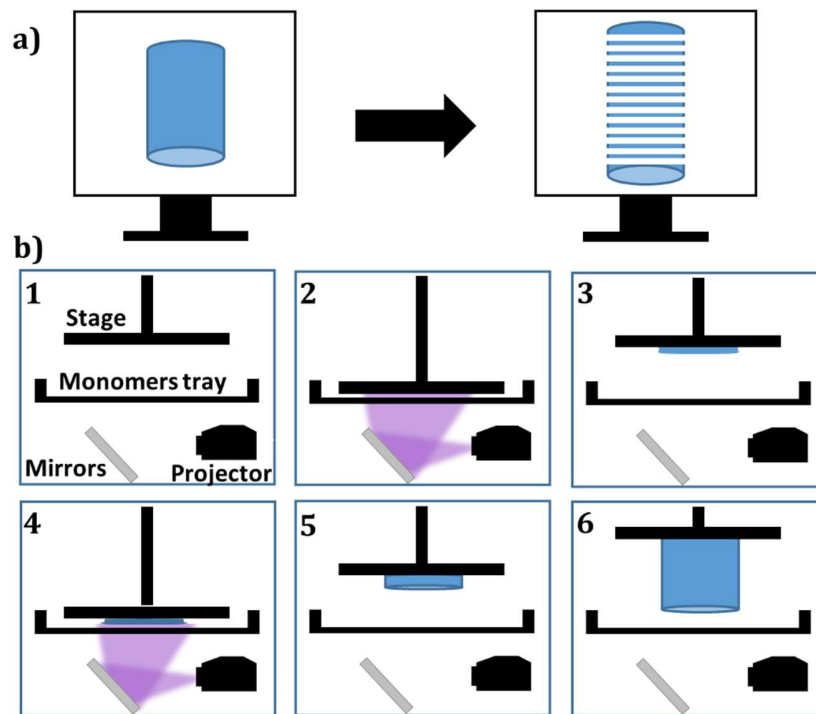


**Figure 1.** a) Slicing the computer 3D model into 2D layers. b) A scheme of the DLP printer components and process.

### 1.1.2. Inkjet Printing

Inkjet printing is a standard two dimensional (2D) approach, which is commonly used nowadays in households and offices. It is based on controlled injection of the ink to form predesigned patterns.<sup>7</sup> Although this method is used mainly for printing of pigmented inks for documents and images, it is also suitable for printing almost any material that can be dissolved or dispersed in a liquid medium. Nowadays, there are significant efforts in development of 2D-printable inks for printed electronic devices.<sup>8</sup>

## **1.2. Functional Materials**

### **1.2.1. Porous Materials**

Porous materials are categorized into three groups: a) microporous materials, with pores diameters smaller than 2 nm, b) mesoporous materials, with pores diameters ranging between 2 nm and 50 nm, and c) macroporous materials, which have pores diameters higher than 50 nm.<sup>9</sup> These materials are mostly known for their high surface area, and adsorption capabilities. For example, activated carbon is a well-known porous material with a surface area of 500 - 3000 m<sup>2</sup>/g.<sup>10</sup> It is commonly used for adsorption purposes, such as purification of drinking water from a variety of pollutants. The adsorption of molecules by porous materials can be attributed to physical and/or chemical adsorption processes.<sup>11, 12</sup> Therefore, by smart chemical and geometrical design of these materials, their properties can be tailored according to the desired application. For example, to have high adsorption selectivity towards certain molecules, catalytic activity, or change of color due to interaction with specific compounds.<sup>13, 14, 15</sup>

#### **1.2.1.1. Zeolites**

Zeolites are microporous aluminosilicate minerals,<sup>16</sup> some of them occur naturally, and some can be synthesized in the laboratory.<sup>17, 18</sup> Zeolites are known for their high surface area, and this is attributed to their microporosity.<sup>19, 20</sup> They are relatively stable and have high decomposition temperatures.<sup>21</sup> Zeolites are widely used, mostly in the industry, for various applications, such as ion exchange, catalysis and separation.<sup>22, 23, 24</sup> The structure of the zeolites comprises a permanent molecular skeleton of silicon, aluminum and oxygen atoms. The skeleton of the zeolite is negatively charged, and can host exchangeable cations, such as sodium, potassium and magnesium. Each zeolite has its unique pore size and channel dimensions; these two properties contribute to the selectivity towards various ions and molecules, and make them excellent candidates for separation and purification processes.



#### 1.2.1.2. MOFs and Other Coordination Polymers

Another type of porous materials is metal organic frameworks (MOFs).<sup>25</sup> These are micro- and mesoporous coordination polymers, which have been investigated extensively since the 1990's. They are composed of metal ions that act as joints, and organic ligands as linkers. During their synthesis, periodic 3D coordination polymeric networks are formed. This leads to the formation of crystalline materials with very high porosity and surface areas as high as 7000 m<sup>2</sup>/g.<sup>26</sup> The wide variety of metal ions and organic molecules that can serve as linkers, enables the tailoring of the MOFs chemical properties, pores sizes and the overall surface area. Their highly ordered and porous architecture results in many potential applications, such as gas storage, catalysis and sensors.<sup>27, 28, 29</sup> However, so far there have been only few examples of successful utilizations of these materials in industry or for commercial applications.<sup>30, 31</sup> The limited use so far was mostly due to several critical issues: many of the MOFs are relatively unstable at various conditions, for example, in aqueous environments.<sup>32, 33</sup> Also, they are mostly in the form of powders, which limits their mechanical properties and makes them difficult to handle.

Although MOFs are currently the most popular type of coordination polymers (CPs), there are many other polymeric compounds, which contain metal ions linked with organic ligands.<sup>34, 35</sup> These materials can be formed as one, two or three dimensional polymers. Their structure may be porous or non-porous, as well as crystalline or amorphous, and it is possible to design them according to the required utilization.<sup>36</sup> The synthesis of MOFs and other CPs follows a typical route, in which metal ions are introduced to organic molecules with at least two electron donating groups that can bind to the metal ions.<sup>37</sup> These organic molecules bridge between the metal ions and form molecular chains and nets (Figure 2). When a solvent is present, it occupies the pores that are formed in the process, and prevents them from collapsing. With MOFs and some additional CPs, upon evacuation of the solvent following the synthesis step, porous materials with high surface areas are formed.

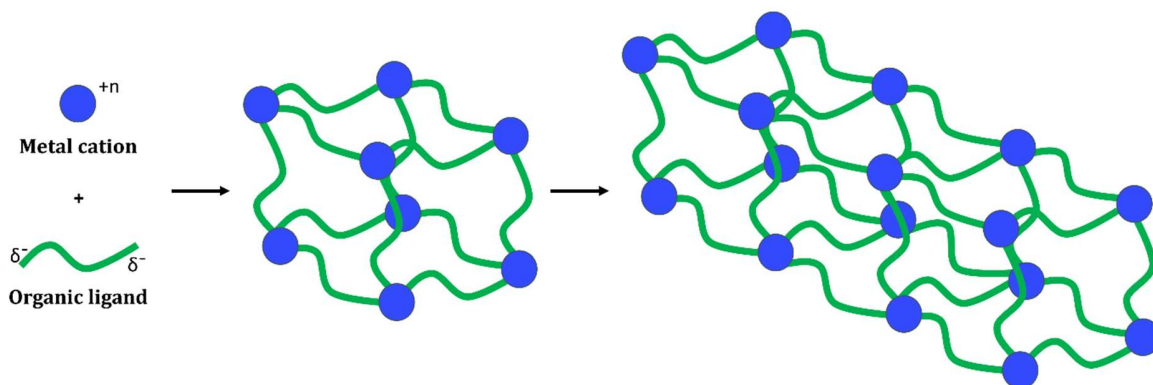


**Figure 2.** Formation of a coordination polymer.

### 1.2.2. Small-Molecules Organic Semiconductors

This group of functional materials include polyaromatic hydrocarbons (PAHs) such as pentacene, perylene, and others (Figure 3). Also included are metal ions complexes with conjugated ligands as Copper phthalocyanine (CuPc).<sup>38, 39</sup> These compounds have semiconducting properties, due to  $sp^2$  hybridization of the carbon and nitrogen atoms, which allows delocalization of  $\pi$ -electrons.<sup>40</sup>

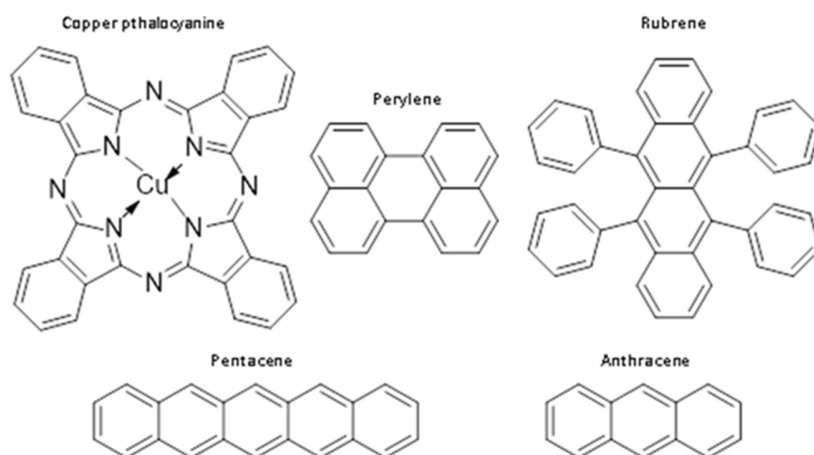


**Figure 3.** Polyaromatic compounds.

Compared to silicon and other inorganic semiconductors, these compounds have several advantages. Their major advantage is a possibility to utilize the high-throughput deposition methods such as inkjet-printing and screen-printing.<sup>41</sup> These methods have the potential to enable the fabrication of transistors, photovoltaic cells, OLEDs, memory components and

other electronic devices at lower costs. Moreover, they enable the coverage of large areas, and the fabrication of flexible devices, since the temperatures required are much lower than the glass temperature and decomposition temperature of the flexible polymeric substrates. Such advantages led to many new applications that could not be reached with the inorganic wafer-based materials.

### **1.3. Chemical Control Over the Formation of Function-Enhancing Confined Structures**

#### **1.3.1. Organic-Inorganic Porous Composites**

In the 1980's, the mixed-matrix-membranes (MMM) were introduced.<sup>42</sup> These membranes, which are still utilized nowadays mostly for separation and purification purposes,<sup>43, 44</sup> are composed of a thin organic matrix, which is incorporated with inorganic particles, such as MOFs and zeolites, as fillers.<sup>45, 46</sup> By doing so, it is possible to enjoy the benefits of the superior separation performances of the inorganic materials, while overcoming their processing difficulties, lowering the total cost of the materials, and benefitting from the properties associated with organic polymers, such as flexibility and lower fragility.<sup>47</sup> The inorganic particles in the membranes are accessible to the phase that flows through the membrane, mostly due to the minimal thickness of the membrane, or to the presence of an additional porous support layer.<sup>42</sup>

In recent years, MOF/Zeolite-polymer composites have been developed in the form of monoliths.<sup>48, 49</sup> These can be utilized for various applications, such as catalysis,<sup>50</sup> drug release,<sup>49</sup> extraction of materials from solutions and more.<sup>51</sup> Those monoliths are often prepared by polymerizing a mixture of monomers and the inorganic compound, in order to create MOF- or zeolite-embedded polymeric structures. In opposed to the MMMs, which have a thickness proportions that resembles 2D materials, the monoliths are three dimensional. Therefore, the composite should be designed in such a way that there would be sufficient accessibility of the liquid or gaseous medium towards the embedded inorganic particles. One possible route is to design 3D macrometric structures that are composed of many micrometric sections, such as three dimensional nets, and expose as much inorganic particles as possible on the surface of the structure. A more common method to increase the

availability of the inorganic particles is by forming a porous polymer, which would enable the medium to penetrate and reach the inorganic particles within it.

#### **1.3.1.1. Controlled Polymer Porosity**

A number of parameters of the polymerization reaction (Figure 4a) can affect the degree of porosity and the type of pores that are formed during the synthesis of the polymer. Since this work discusses 3D-printing of such monolithic structures, the relevant parameters are as follows:

##### **1.3.1.1.1. Effect of the Intensity of the Initiating Energy Source**

In case of thermal/UV-light initiation, the higher the temperature or the light intensity, the higher the decomposition rate of the initiator, which results in more radicals, more nuclei, and smaller polymeric particles. This in turn leads to smaller pores and an overall higher surface area.<sup>52</sup>

##### **1.3.1.1.2. Effect of the Porogenic Solvent**

In order to obtain a porous structure, phase separation must occur.<sup>52, 53</sup> At a certain stage, the forming polymer separates from the reaction solution, due to one or two of the following reasons: **(a)** the molecular weight exceeds the solubility limit of the polymer in the solvent; **(b)** cross linking of the polymer chains takes place and forms denser particles. Usually, option **(a)** will result in earlier phase separation and larger pores, while **(b)** will occur at a later stage of the polymerization process, and result in smaller pores and a higher surface area. A solvent that successfully dissolves the monomer and the polymeric chains in the early stage of the polymerization, and delays the phase separation, is considered as a **good porogenic solvent** (Figure 4b). A solvent that leads to the early phase separation of the polymeric chains, and as a result, their swelling with the monomers to form large particles with large pores between them, is considered as a **bad porogenic solvent** (Figure 4c). By

changing the ratios of the good and bad solvents in the mixture, it is possible to tailor the porosity of the polymer according to one's needs.

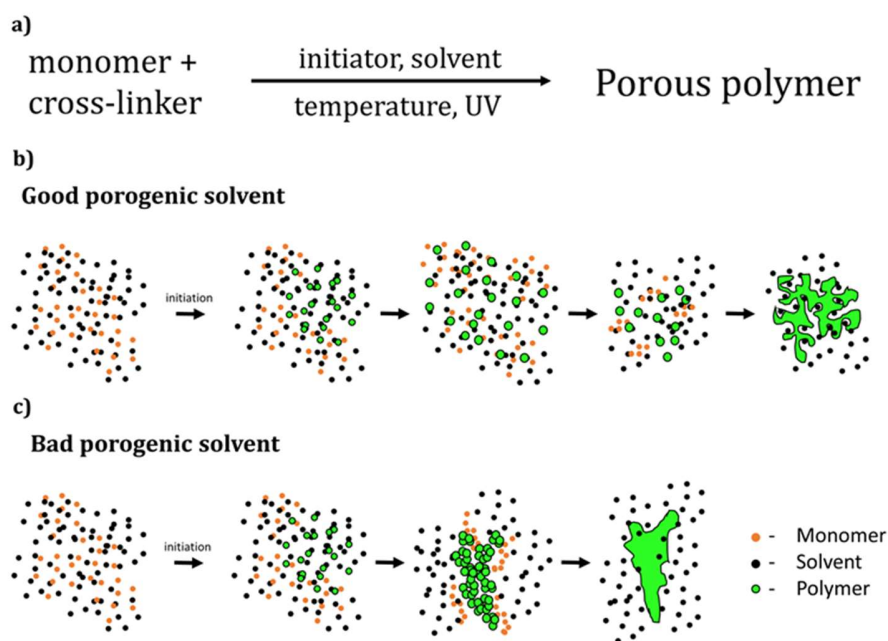


**Figure 4.** a) Parameters of the polymerization reaction. b) A scheme of the formation process of a porous polymer in a good porogenic solvent, due to late phase separation. c) A scheme of the formation of a non-porous polymer in a bad porogenic solvent, due to early phase separation.

#### 1.3.1.1.3. Effect of the Cross-Linker

The higher concentration of a cross-linking monomer leads to early cross-linking and to early phase separation.<sup>52, 54</sup> However, unlike a bad porogenic solvent, the high degree of cross linking does not cause the swelling of the polymerized particles with the monomers that are still in the solution, and forms denser particles. For this reason, the final polymeric particles in the presence of the cross-linker are small, which leads to small pores and high surface area.

### 1.3.2. Single Crystals of Organic Semiconductors

A single crystal is a highly ordered bulk that is composed of a defined and periodic repeating unit of its building blocks. Those building blocks may be whole molecules attached to one another via van der Waals or ionic interactions, or atoms connected through covalent or metallic bonding.

Among small-molecules organic semiconductors, single crystals demonstrate the highest performances,<sup>55, 56</sup> and high mobility values in the range of 5 to 20  $\text{cm}^2\text{V}^{-1}\text{s}^{-1}$  have been obtained.<sup>57</sup> By forming a single crystal, one eliminates most of the impurities and grain boundaries, which act as scattering and trapping sites.<sup>58</sup> Moreover, PAHs and other conjugated systems contain many  $\pi$  orbitals, resulting in the 2D sort of molecular packing in the crystal.<sup>40</sup> This allows 2D charge transport across the layers. Since charge transport between layers is one of the reasons for low efficiency, this type of molecular packing enhances the charge mobility. As opposed to the growth of the covalent inorganic single crystals of silicon, the organic crystals are formed by the alignment of molecules due to van der Waals and  $\pi$  interactions.<sup>57</sup> Therefore, it is much more difficult to control and predict the crystals formation regarding their size and even their exact location on the substrate. However, overcoming these difficulties and having a well-controlled crystallization method may be worthwhile, since carrier mobilities above 30  $\text{cm}^2\text{V}^{-1}\text{s}^{-1}$  have already been measured for organic single crystals.<sup>59</sup>

The most widespread crystallization methods of organic compounds rely on their solubility differences in various organic solvents due to temperature, pressure and molecular structure.<sup>57</sup> The common characteristic of all solvent-based crystallization methods is their goal to reach super-saturation of the solution. This would cause the creation of nuclei that can grow further to form micrometric and millimetric single crystals. In order to do so, without causing a fast and amorphous precipitation of the solute, one should perform the process in a very slow and controllable manner.

Super-saturation can be achieved by various ways: by slow evaporation of the solvent that increases the concentration of the solute, and by slow cooling of the solution that results in gradual decrease of solubility of the solute in the solvent. Other methods involve mixing the

solution with an anti-solvent either by slow liquid-liquid diffusion or vapor-liquid diffusion. As the percentage of the anti-solvent in the solution grows, the solubility of the solute decreases and crystals may form. Another, less common, but effective method is the physical vapor transport (PVT).<sup>57</sup> This method relies on sublimation temperatures and molecular weight of the organic compound. This process can be performed under inert atmosphere or vacuum and is suitable for organic compounds such as perylene and rubrene that sublime without decomposition.

#### **1.4. Printing of Functional Materials in 2D and 3D Structures**

In the past, most 2D- and 3D-printed patterns and objects were composed mainly of pigmented ink or structural materials, such as polymers. In recent years, controlled deposition of functional materials, such as conductive, porous and biocompatible patterns and structures attracted a growing interest.<sup>8, 60, 61</sup> From self-assembly to 2D- and 3D-printing, the structural order can be found in the macro/micro scale, e.g. printed millimetric or micrometric defined structures; or in the nano and molecular scale, such as the controlled arrangement of molecules to form a single crystal. The formation of such confined and defined structures of functional materials enables enhanced performances and wide utilization.<sup>62, 63, 64</sup> Since both, 2D- and 3D-printing are powerful tools for deposition of materials in confined structures, there is a need for developing methods and materials that are suitable for the formation of such functional structures by printing.

#### **1.5. Research Objectives**

##### **Main objective**

The primary goal, from which we derived the research objectives, was to develop materials and methods for printing and for the deposition of functional materials in defined and ordered structures at the macro- and micro-scales. By doing this, we overcame certain limitations of the materials, and enabled a more significant utilization of the functional materials for various purposes. Therefore, the research objectives included aspects related to both 2D- and 3D-printing.

- **To develop materials and methods for 3D-printing of porous functional materials, such as MOFs and zeolites, while maintaining their functional properties and overcoming their limitations.**

One method to obtain 3D structures of functional materials is to mix them with organic monomers or polymers that would form a polymeric matrix embedded with the desired material.<sup>65</sup> We utilized known organic monomers to form MOF- and zeolite-embedded 3D structures. Once obtained, the 3D structures were utilized for various purposes according to their functionality.

- **To utilize 3D-printing for the synthesis of porous coordination polymers in confined structures.**

So far, we could not find any papers regarding direct 3D-printing of monomers to form porous coordination polymers. There appeared to be three main challenges: first, the synthesis of the suitable monomers for this purpose and their structural characterization; second, the polymerization process of the monomers to form a porous coordination polymer; third, the verification of whether the metal-ligand bond sustained the polymerization reaction.

- **To develop materials and an inkjet-printing method for the controlled deposition and growth of organic single crystals.**

According to previous publications, in order to control the growth of a single crystal, a confining frame or area of some sort should exist. Thus, we used the inkjet printer as a lithography tool for the patterning of a confinement area and the deposition of the solutions in such a way that will induce crystallization. An important feature of this method should be the diversity of optional substrates, especially flexible ones. The functional material that was crystallized was a small-molecules OSC. This was due to the increased performance of single crystals of these materials, compared to their amorphous form. The resulting crystals were characterized structurally, optically and electrically to assess their quality.





## **2. Results**



## **2.1. Chapter 1: Hydrolytically Stable MOF in 3D-Printed Structures**

Published<sup>66</sup>: Halevi O., Tan J.M.R., Lee P.S., Magdassi S. Hydrolytically Stable MOF in 3D-Printed Structures. *Advanced Sustainable Systems* **2**, 1700150 (2018).



# Hydrolytically Stable MOF in 3D-Printed Structures

Oded Halevi, Joel M. R. Tan, Pooi See Lee,\* and Shlomo Magdassi\*

Metal–organic frameworks (MOFs) are a well-developed field of materials, having a high potential for various applications such as gas storage, water purification, and catalysis. Despite the continuous discoveries of new MOFs, so far there are only a limited number of industrial applications, partially due to their low chemical stability and limited mechanical properties, as well as difficulties in integration within functional devices. Herein, a new approach is presented toward the fabrication of MOF-based devices, utilizing direct 3D printing. By this method, 3D, flexible, and hydrolytically stable MOF-embedded polymeric structures are fabricated. It is found that the adsorption capacity of the 3D-printed MOF is retained, with significantly improved hydrolytic stability of the printed MOFs (copper benzene-1,3,5-tricarboxylate) compared to the MOF only. It is expected that applying 3D printing technologies, for the fabrication of functional MOF objects such as filters and matrices for columns and flow reactors, will open the way for utilization of this important class of materials.

## 1. Introduction

Metal–organic frameworks (MOFs) are a well-investigated family of functional materials, which are composed of metal ions that act as joints with organic ligands as linkers. The wide range of metal ions and organic ligands enables high structural tunability and a variety of physical and chemical properties, thus enabling their use in many fields such as catalysis, sensing, and chemical separation.<sup>[1,2]</sup> MOFs are extremely porous, with surface areas as high as several thousands of  $\text{m}^2 \text{g}^{-1}$ .<sup>[3]</sup> Therefore, MOFs are also commonly investigated as adsorbents for applications such as gas separation and storage, and water purification.<sup>[4,5]</sup>

Despite their extensive potential as active materials for various applications, up to now, the transition of MOFs from academic research to industrial applications has been very

limited, although several companies have been mass producing several MOFs.<sup>[6,7]</sup> Two main reasons for this are their low hydrolytic stability and the lack of proper mechanical properties. Certain progress has been made toward the formation of better water-stable MOF systems.<sup>[8,9]</sup> This has been achieved for copper benzene-1,3,5-tricarboxylate (Cu-BTC) either by depositing the hydrophobic perfluorohexane on the water-sensitive MOF or by incorporating the MOF particles within a 2D hydrophobic matrix. However, these approaches are scarce, and nowadays overcoming water sensitivity is mostly achieved by design and synthesis of new MOFs with better linkers and metal centers which are less sensitive to water.<sup>[10,11]</sup> Regarding the requirement for mechanical properties, such as flexibility, one approach is based on the formation of

mixed matrix membranes of MOFs and polymers.<sup>[12]</sup> Nevertheless, while achieving some of the desired mechanical properties, this approach is relevant only for thin films which contain polymeric materials, such as membranes.<sup>[13,14]</sup> There is yet an unmet need for 3D structures of MOFs, such as matrices for flow reactors and 3D filters. We address this by direct printing of complex 3D objects by combining MOF particles with photopolymerizable materials.

3D printing is a powerful tool for the fabrication of complex objects composed of various materials.<sup>[15,16]</sup> This technology enables manufacturing of devices and functional objects for various fields and applications, ranging from printed detectors, chemical reactions vessels, up to complex automotive bodies.<sup>[17–20]</sup> With this method, fabrication of functional objects can be achieved either by utilizing functional monomers that form a polymer with the desired properties<sup>[21,22]</sup> or by embedding functional materials within the printed structure.<sup>[23]</sup>

Several reports discuss the deposition of MOFs by microfluidic methods and 2D inkjet printing.<sup>[24–26]</sup> Moreover, functionalization of 3D objects by sequential coating of polymeric objects with MOFs has been demonstrated very recently.<sup>[27,28]</sup> Wang et al. printed 3D porous structures composed of acrylonitrile–butadiene–styrene, followed by coating the structure with Cu-BTC for the adsorption of methylene blue (MB).<sup>[29]</sup> However, so far, there are no publications on direct printing of MOFs into 3D complex structures.

Herein, we present the 3D printing of MOF-embedded polymeric structures, by the Digital Light Processing (DLP) printing method (Figure 1a).<sup>[30]</sup> The DLP process is based on localized photopolymerization of monomers and oligomers, in the presence of suitable photoinitiators. This process enables

O. Halevi, Prof. S. Magdassi  
Casali Center of Applied Chemistry  
Institute of Chemistry  
The Hebrew University of Jerusalem  
Jerusalem 91904, Israel  
E-mail: Magdassi@mail.huji.ac.il

O. Halevi, Dr. J. M. R. Tan, Prof. P. S. Lee  
School of Materials Science and Engineering  
Nanyang Technological University  
Singapore 639798, Singapore  
E-mail: PSLee@ntu.edu.sg

The ORCID identification number(s) for the author(s) of this article can be found under <https://doi.org/10.1002/adsu.201700150>.

DOI: 10.1002/adsu.201700150

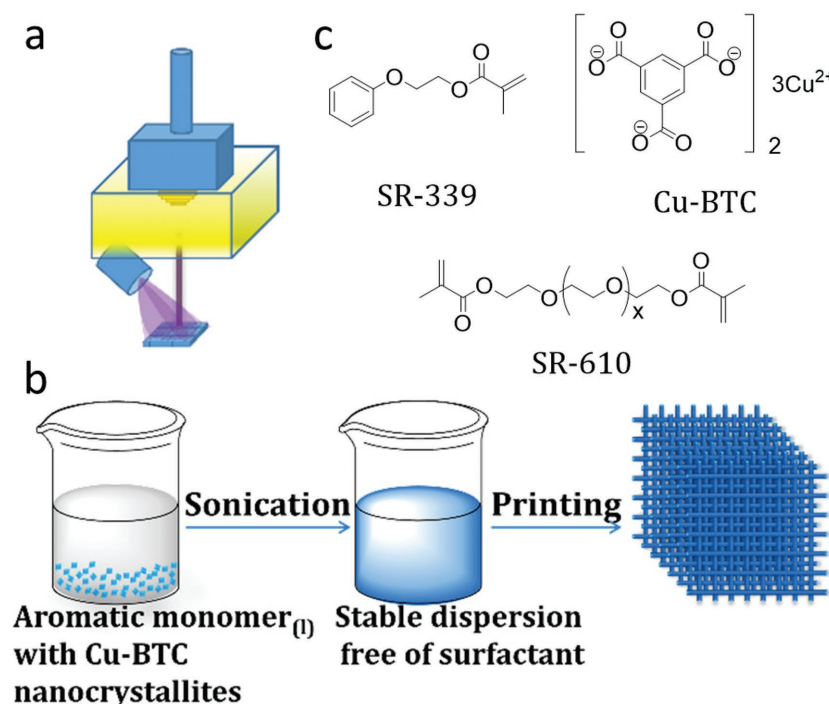


**Figure 1.** a) DLP printing: the stage descends into the resin bath; the UV light is projected onto the DLP mirror array and forms the desired image. Then the light initiates the polymerization reaction to form the polymer layer on the stage. The process is repeated over and over to form the 3D object. b) First, the Cu-BTC crystals are dispersed in the aromatic monomer. Then the photoinitiator is added and the formulation is printed with the DLP printer. c) The monomer, SR-339; the crosslinker, SR-610; and the MOF, Cu-BTC.

aromatic group, which can increase its affinity toward the MOF particles and yield a stable dispersion without any dispersants. Moreover, poly(2-phenoxyethyl acrylate) is hydrophobic and therefore can enhance the hydrolytic stability of the Cu-BTC that is embedded within.<sup>[8,36]</sup> The resulting dispersion of 10 wt% Cu-BTC (after sonication) was stable throughout for several hours, a time duration which is required for completing the printing process without significant sedimentation of Cu-BTC. Upon further increase of the MOF's concentration, it has become more difficult to form a stable dispersion without the addition of a surfactant. Therefore, the MOF's concentration of choice was 10 wt%. Since SR-339 is a monofunctional monomer, a crosslinker with two acrylate groups, polyethylene glycol (600) diacrylate (SR-610), was added to introduce a rigidity to the polymerized structure (Figure 1c). To enable the photopolymerization of the resulting opaque dispersion, a combination of two photoinitiators, Irgacure-819 and Irgacure-184, was required. Finally, the ink composition containing the monomers, MOF particles, and photoinitiators, was printed by the DLP printer. As shown in Figure 2, complex and flexible 3D structures could be formed with the typical blue color of the MOF (Cu-BTC@polymer).

the formation of MOF-containing 3D polymeric flexible objects, while preserving the adsorption capacity of the embedded MOF and significantly increases its hydrolytic stability. To demonstrate the advantages of the new approach, we selected the water-sensitive Cu-BTC as a model MOF compound,<sup>[31,32]</sup> while adsorption experiments were conducted in aqueous solutions to investigate the retention of the MOF's functionality in the 3D-printed object.<sup>[33,34]</sup>

## 2. Results and Discussion

### 2.1. 3D Printing of MOF-Embedded Structures

At the first stage, we synthesized Cu-BTC by modifying the method presented by Lee and co-workers for the synthesis of Ni-BTC, while mainly replacing the nickel nitrate with copper nitrate.<sup>[35]</sup> At the second step, the MOF particles were dispersed within a photopolymerizable composition, to enable printing a polymeric matrix that would support the MOF (Figure 1b).

At this step it was crucial to find a monomer mixture that would enable the formation of a stable dispersion, without adding a dispersion agent that might block the surface of the MOF particles and block their adsorption sites. Taking into consideration that Cu-BTC is composed of aromatic ligands bonded to the copper ion, the acrylate monomer, 2-phenoxyethyl acrylate (Sartomer SR-339), was chosen (Figure 1c). This monomer contains an

### 2.2. Evaluation of the 3D-Printed MOF

Following polymerization of the monomer, powder X-ray diffraction (PXRD) measurements of the resulting Cu-BTC@polymer were performed (Figure 3). In the diffractogram of Cu-BTC@polymer, some of the peaks that are attributed to the crystalline MOF can be observed along with the amorphous polymeric phase. This indicates that the MOF has kept its crystalline structure during the radical polymerization process. The functionality of Cu-BTC and Cu-BTC@polymer in the short and long periods of time was evaluated by adsorption experiments of MB. A bulk sample of Cu-BTC embedded within the polymer was shaped by photopolymerization of Cu-BTC and monomers in a solid mold. Figure 4a shows the adsorption versus time curves for the pure Cu-BTC in its powder form, the Cu-BTC@polymer in a mold, 3D-printed model and the polymer alone.

In these experiments, the net amount of Cu-BTC in each of the MOF-containing samples was 10 mg. In the case of the pure polymer, the measured sample was composed of 100 mg of polymer. For the bulk Cu-BTC@polymer that was made by polymerization in a mold, a significant decrease of MB adsorption was observed compared with the pure Cu-BTC. This indicated that most of the MOF in the Cu-BTC@polymer system was blocked by the polymer and the only active MOF was located at the external surface of the polymerized object. To expose a higher fraction of the Cu-BTC, removal of the

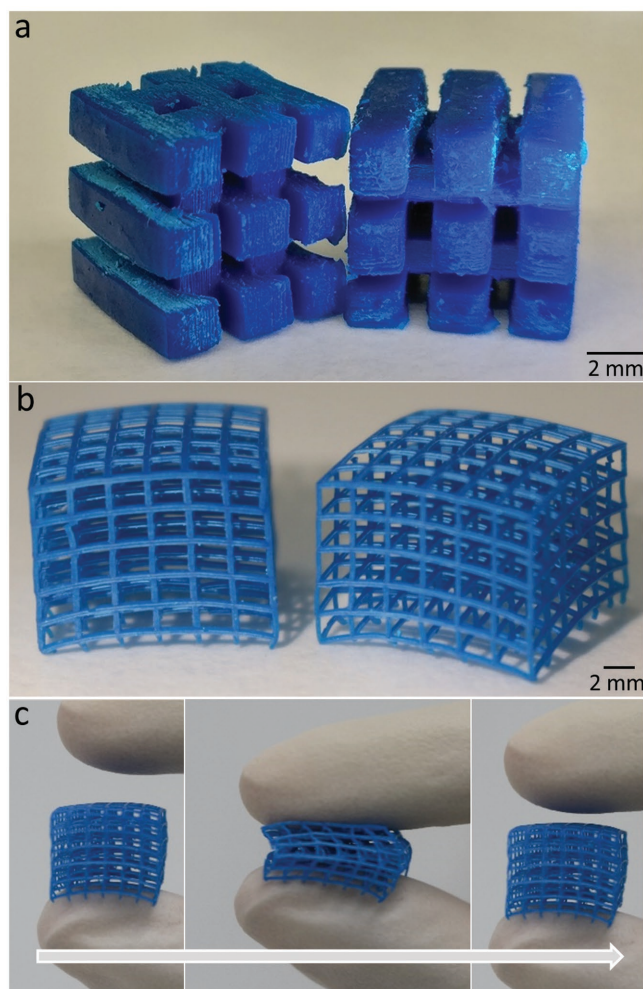


**Figure 2.** a) 3D-printed models of Cu-BTC@polymer. b) 3D-printed nets of Cu-BTC@polymer. c) Demonstration of the flexibility of the 3D-printed object before, during, and after pressing.

polymeric matrix by heat decomposition was investigated. thermal gravimetric analysis (TGA) measurements (Figure S1, Supporting Information) indicated that the MOF decomposed

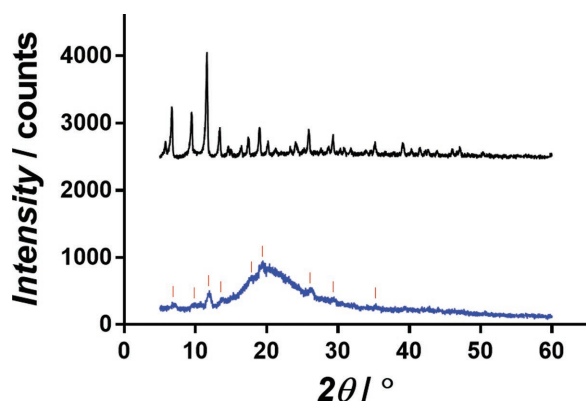


**Figure 3.** PXRD of the pure Cu-BTC and the Cu-BTC@polymer. The corresponding peaks are marked with red lines. Legend: —Cu-BTC, —Cu-BTC@polymer.

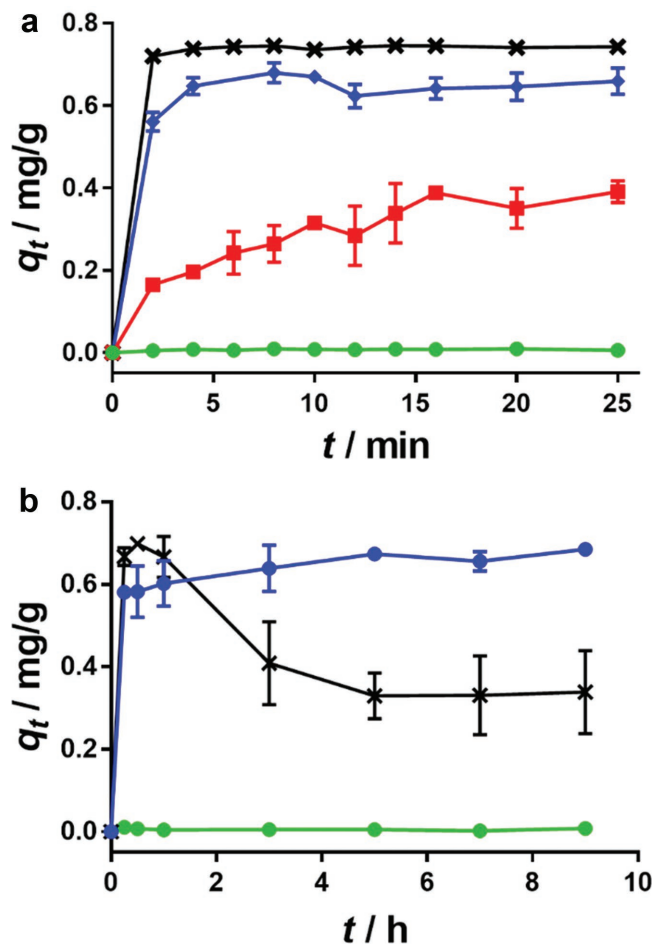


**Figure 4.** a) Adsorption curves of MB over short periods of time, by the various samples of Cu-BTC and the polymer. b) Adsorption curves of MB over long periods of time, by the pure powder Cu-BTC, printed Cu-BTC@polymer, and the polymer. Legend:  $\times$  Cu-BTC,  $\square$  Cu-BTC@polymer,  $\bullet$  Cu-BTC@polymer 3D printed,  $\circ$  Only polymer.

at a temperature slightly above 250 °C, while the decomposition of the polymer started at a lower temperature, under 200 °C, but proceeded up to 450 °C. Due to this, the heating temperature was limited to less than 250 °C, and although a significant weight loss of the polymer was achieved (30–40 wt%), its residues remained and therefore no increased adsorption of MB was observed (Figures S2–S4, Supporting Information). A more detailed description of the decomposition experiments appears in the Supporting Information.

To overcome this obstacle and expose more of the Cu-BTC, we utilized the powerful capabilities provided by additive manufacturing processes, by printing with a DLP printer to fabricate fine structures. Therefore, we printed a 3D net structure with a high macrosurface area, composed of 2 mm wide holes and 200  $\mu\text{m}$  wide grid lines (Figure 2b). Indeed, it was found by adsorption experiments of MB that the adsorption capacity significantly increased due to the presence of MOF within the 3D structure compared to simple embedding within the polymer. Furthermore, the adsorption capacity almost reached that of the MOF only, with a similar adsorption kinetics at the first period of the adsorption experiment (Figure 4a). Scanning electron



microscopy (SEM) evaluation of the cross section of the printed structure (Figure S5, Supporting Information) revealed that there was segregation of polymer-rich areas in the inner part of the printed structure and crystal-rich areas in its external part. This explains the relatively high adsorption capacity of the printed structure. To further demonstrate the effect of the objects' surface area on the adsorption capacity, a layered-cylinder structure was printed (Figure S6, Supporting Information). The change from the net structure to cylinders resulted in a lower surface area. Adsorption measurements of MB (Figure S3, Supporting Information) showed a slight decrease in the adsorption capacity, which is attributed to the decrease of the surface area of the structure.

The stability of the MOF@polymer system was investigated by adsorption measurements over a time duration of up to 9 h. Figure 4b demonstrates the adsorption of MB by the 3D-printed objects compared to the Cu-BTC in its powder form. As expected, the pure Cu-BTC adsorbed the MB during the first 30 min, and at longer time durations it released the MB back into the solution. The release of MB results from the well-known degradation of the Cu-BTC due to hydrolysis.<sup>[9]</sup> On the contrary, MB adsorbed by the Cu-BTC@polymer remained adsorbed during the entire period, due to the enhanced stability of 3D-MOF in water. These results correlate well with the report by Cohen and co-workers which demonstrated that Cu-BTC in a polymeric membrane is stable in an aqueous environment, due to prevention of the formation of water clusters near the copper ions, thus preventing the breakdown of the Cu-BTC to Cu(OH)<sub>2</sub>.<sup>[8]</sup>

### 3. Conclusion

In conclusion, for the first time, we fabricated complex 3D structures with embedded MOF, which significantly increase its hydrolytic stability while retaining the MOF's activity. Moreover, we successfully printed a flexible MOF-embedded 3D object, which suggests that by appropriate selections of the monomers, the overall mechanical properties can be tailored. We believe that this proof of concept for direct 3D printing of MOF-containing functional objects is a significant step toward the enabling of utilization of MOF in functional devices. Future research will focus on controlled decomposition of the polymeric matrix, in order to enable even higher exposure of the MOF within the printed objects, and on using the DLP printing for additional MOFs with various functionalities.

### 4. Experimental Section

**Synthesis of Cu-BTC:** Benzene-1,3,5-tricarboxylic acid (98%, Sigma) (2 g) was dissolved in absolute ethanol (VWR Chemicals) (80 mL) and triple distilled water (TDW) (80 mL). Then the solution was neutralized to pH = 7 with 1 M NaOH. Cu(NO<sub>3</sub>)<sub>2</sub>·2.5H<sub>2</sub>O (98%, Sigma) (4 g) was dissolved in TDW (40 mL) and added dropwise to the BTC solution with vigorous stirring at room temperature. During the addition of the copper solution, blue precipitate was formed. The reaction was stirred for 12 h and the blue product, Cu-BTC, was separated from the solution by centrifugation. The product was washed three times with TDW and

three times with absolute ethanol and was put in a vacuum oven at 60 °C overnight.

**Preparation of the Printing Formulation:** Cu-BTC (2 g) was mixed with SR-610 (Sartomer) (2 g) and SR-339 (Sartomer) (16 g). To form a homogeneous dispersion, the mixture was sonicated with a tip-sonicator (Sonics Vibra-cell, 500 W) for 30 min (2 s ON, 2 s OFF) and 50% amplitude. Following this, photoinitiators, Irgacure 819 (BASF) (0.133 g) and Irgacure 184 (BASF) (0.266 g), were dissolved in the dispersion.

**Polymerization in Molds:** To perform the characterization of the Cu-BTC@polymer, the formulation was polymerized in molds. In each mold, three drops of formulation were deposited and then exposed to UV light (Asiga Flush, 365 nm, 9 W × 4) for 90 s to achieve complete polymerization.

**3D Printing:** The models were printed with a DLP 3D printer (Asiga Pico 2). The printing parameters are provided in Table S1 in the Supporting Information. Following the printing, the objects were washed with isopropyl alcohol to remove the unpolymerized residues.

**Heat Treatment:** The polymerized Cu-BTC@polymer was heated with a heating rate of 0.5 °C min<sup>-1</sup> up to 200 °C and was left at that temperature for 48 and 72 h. The weight of the samples was measured before and after heating to calculate the weight loss percentage as a result of the process.

**Characterization:** The surface morphology evaluation of the samples was performed by scanning electron microscopy (Carl Zeiss SUPRA 55). Prior to the measurements, the samples were dried overnight in a vacuum oven at 60 °C. The structure of the samples was characterized by PXRD (Shimadzu XRD-6000).

**Absorbance Curves:** About 5 ppm aqueous solutions of MB (Merck) were used as the adsorbed materials. The amount of each adsorbent was determined so that the net amount of Cu-BTC in the sample would be 10 mg (Table S2, Supporting Information). In each measurement, MB solution (1500 µL) was added to the required amount of sample and stirred with a Vortex at 25 °C. Following this, the solid sample was separated from the solution and the absorbance of the resulting MB solution was measured with a UV-vis spectrophotometer at λ = 665 nm (PerkinElmer, Lambda 950).

**Crystal Size Measurements:** The crystals average sizes were measured from the SEM photos with ImageJ software.

### Supporting Information

Supporting Information is available from the Wiley Online Library or from the author.

### Acknowledgements

This research was supported by the Singapore National Research Foundation under the CREATE program: Nanomaterials for Energy and Water-Energy Nexus and by the Hebrew university fund for Ph.D. students.

### Conflict of Interest

The authors declare no conflict of interest.

### Keywords

3D printing, additive manufacturing, metal-organic framework (MOF), polymers

Received: October 10, 2017

Revised: November 18, 2017

Published online:

- [1] B. Li, M. Chrzanowski, Y. Zhang, S. Ma, *Coord. Chem. Rev.* **2016**, 307, 106.
- [2] Y. J. Cui, B. Li, H. J. He, W. Zhou, B. L. Chen, G. D. Qian, *Acc. Chem. Res.* **2016**, 49, 483.
- [3] H. Furukawa, K. E. Cordova, M. O'Keeffe, O. M. Yaghi, *Science* **2013**, 341, 974.
- [4] B. Li, H. M. Wen, W. Zhou, B. L. Chen, *J. Phys. Chem. Lett.* **2014**, 5, 3468.
- [5] S. Q. Li, Y. F. Chen, X. K. Pei, S. H. Zhang, X. Feng, J. W. Zhou, B. Wang, *Chin. J. Chem.* **2016**, 34, 175.
- [6] Editorial, *Nat. Chem.* **2016**, 8, 987.
- [7] T. Faust, O. Farha, B. Hernandez, *Nat. Chem.* **2016**, 8, 990.
- [8] J. B. DeCoste, M. S. Denny, G. W. Peterson, J. J. Mahle, S. M. Cohen, *Chem. Sci.* **2016**, 7, 2711.
- [9] J. B. Decoste, G. W. Peterson, M. W. Smith, C. A. Stone, C. R. Willis, *J. Am. Chem. Soc.* **2012**, 134, 1486.
- [10] A. J. Howarth, Y. Y. Liu, P. Li, Z. Y. Li, T. C. Wang, J. Hupp, O. K. Farha, *Nat. Rev. Mater.* **2016**, 1, 15.
- [11] J. Dechnik, A. Nuhnen, C. Janiak, *Cryst. Growth Des.* **2017**, 17, 4090.
- [12] M. W. Anjum, F. Vermoortele, A. L. Khan, B. Bueken, D. E. De Vos, I. F. J. Vankelecom, *ACS Appl. Mater. Interfaces* **2015**, 7, 25193.
- [13] B. Seoane, J. Coronas, I. Gascon, M. E. Benavides, O. Karvan, J. Caro, F. Kapteijn, J. Gascon, *Chem. Soc. Rev.* **2015**, 44, 2421.
- [14] G. Dong, H. Li, V. Chen, *J. Mater. Chem. A* **2013**, 1, 4610.
- [15] C. Minas, D. Carnelli, E. Tervoort, A. R. Studart, *Adv. Mater.* **2016**, 28, 9993.
- [16] Z. C. Eckel, C. Y. Zhou, J. H. Martin, A. J. Jacobsen, W. B. Carter, T. A. Schaedler, *Science* **2016**, 351, 58.
- [17] G. D. Goh, S. Agarwala, G. L. Goh, V. Dikshit, S. L. Sing, W. Y. Yeong, *Aerosp. Sci. Technol.* **2017**, 63, 140.
- [18] J. L. Erkal, A. Selimovic, B. C. Gross, S. Y. Lockwood, E. L. Walton, S. McNamara, R. S. Martin, D. M. Spence, *Lab Chip* **2014**, 14, 2023.
- [19] a) P. J. Kitson, R. J. Marshall, D. Long, R. S. Forgan, L. Cronin, *Angew. Chem., Int. Ed.* **2014**, 53, 12723; b) P. J. Kitson, R. J. Marshall, D. Long, R. S. Forgan, L. Cronin, *Angew. Chem.* **2014**, 126, 12937.
- [20] P. J. Kitson, S. Glatzel, W. Chen, C. G. Lin, Y. F. Song, L. Cronin, *Nat. Protoc.* **2016**, 11, 920.
- [21] M. Zarek, M. Layani, I. Cooperstein, E. Sachyani, D. Cohn, S. Magdassi, *Adv. Mater.* **2016**, 28, 4449.
- [22] H. N. Chia, B. M. Wu, *J. Biol. Eng.* **2015**, 9, 4.
- [23] A. E. Jakus, E. B. Secor, A. L. Rutz, S. W. Jordan, M. C. Hersam, R. N. Shah, *ACS Nano* **2015**, 9, 4636.
- [24] D. Witters, N. Vergauwe, R. Ameloot, S. Vermeir, D. De Vos, R. Piers, B. Sels, J. Lammertyn, *Adv. Mater.* **2012**, 24, 1316.
- [25] L. L. da Luz, R. Milani, J. F. Feix, I. R. B. Ribeiro, M. Talhavi, B. A. D. Neto, J. Chojnacki, M. O. Rodrigues, S. A. Junior, *ACS Appl. Mater. Interfaces* **2015**, 7, 27115.
- [26] J.-L. Zhuang, D. Ar, X.-J. Yu, J.-X. Liu, A. Terfort, *Adv. Mater.* **2013**, 25, 4631.
- [27] C. Z. Wang, S. Tadepalli, J. Y. Luan, K. K. Liu, J. J. Morrissey, E. D. Kharasch, R. R. Naik, S. Singamaneni, *Adv. Mater.* **2017**, 29, 1604433.
- [28] G. Huang, D. M. Yin, L. M. Wang, *J. Mater. Chem. A* **2016**, 4, 15106.
- [29] Z. Wang, J. Wang, M. Li, K. Sun, C.-j. Liu, *Sci. Rep.* **2014**, 4, 5939.
- [30] R. L. Truby, J. A. Lewis, *Nature* **2016**, 540, 371.
- [31] M. P. Singh, N. R. Dhumal, H. J. Kim, J. Kiefer, J. A. Anderson, *J. Phys. Chem. C* **2016**, 120, 17323.
- [32] P. Kusgens, M. Rose, I. Senkovska, H. Frode, A. Henschel, S. Siegle, S. Kaskel, *Microporous Mesoporous Mater.* **2009**, 120, 325.
- [33] M. Rafatullah, O. Sulaiman, R. Hashim, A. Ahmad, *J. Hazard. Mater.* **2010**, 177, 70.
- [34] E. Haque, J. W. Jun, S. H. Jhung, *J. Hazard. Mater.* **2011**, 185, 507.
- [35] R. Bendi, V. Kumar, V. Bhavanasi, K. Parida, P. S. Lee, *Adv. Energy Mater.* **2016**, 6, 1501833.
- [36] J. Chen, M. C. Chen, *Water Sci. Technol.* **2011**, 63, 1638.



# **ADVANCED SUSTAINABLE SYSTEMS**

## Supporting Information

for *Adv. Sustainable Syst.*, DOI: 10.1002/adsu.201700150

### Hydrolytically Stable MOF in 3D-Printed Structures

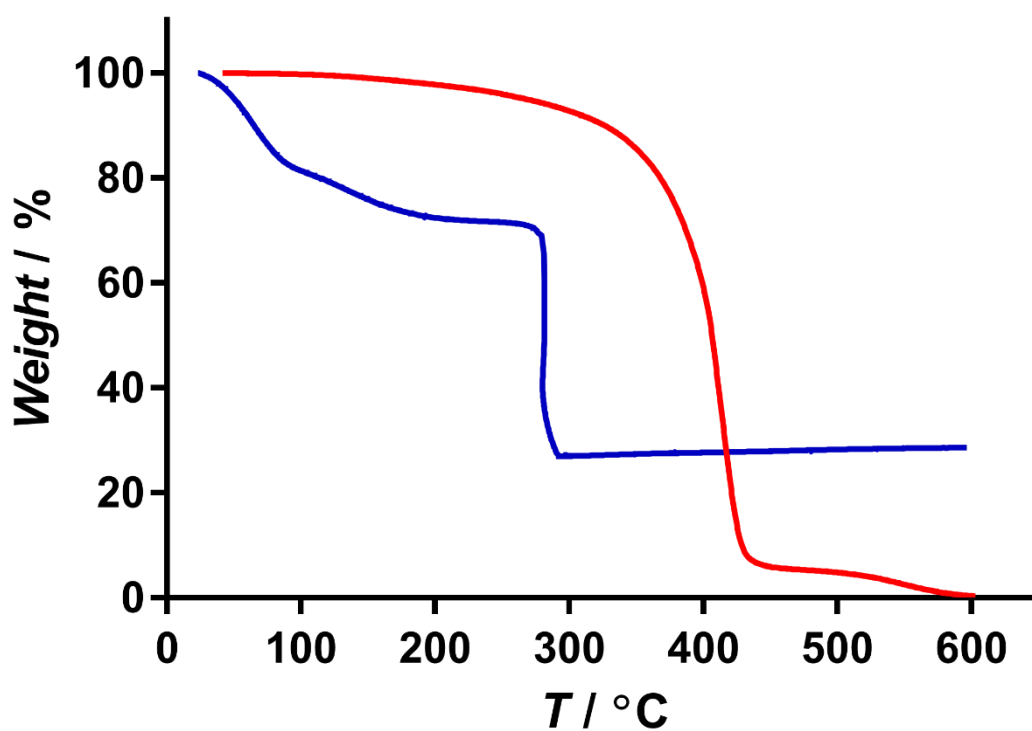
*Oded Halevi, Joel M. R. Tan, Pooi See Lee,\* and Shlomo Magdassi\**

## Supporting Information

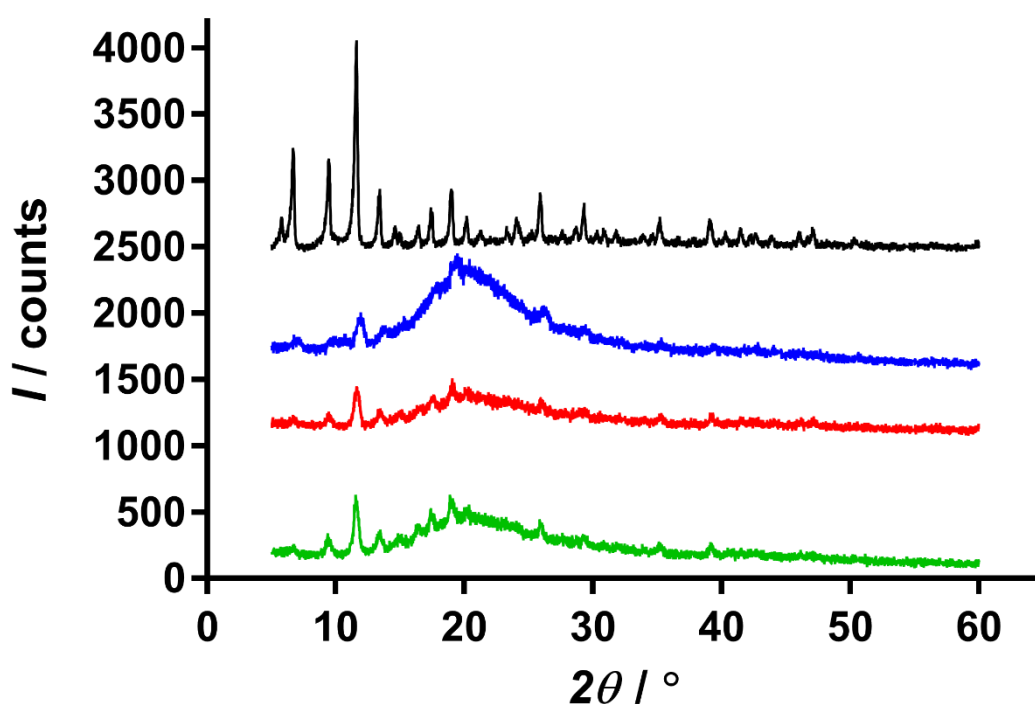
### **Hydrolytically Stable MOF in 3D Printed Structures**

*Oded Halevi, Joel M. R. Tan, Pooi See Lee\*, Shlomo Magdassi\**

1. Fig. S1
2. Fig. S2
3. Fig S3
4. Fig S4
5. Fig S5
6. Fig S6
7. Table S1
8. Table S2

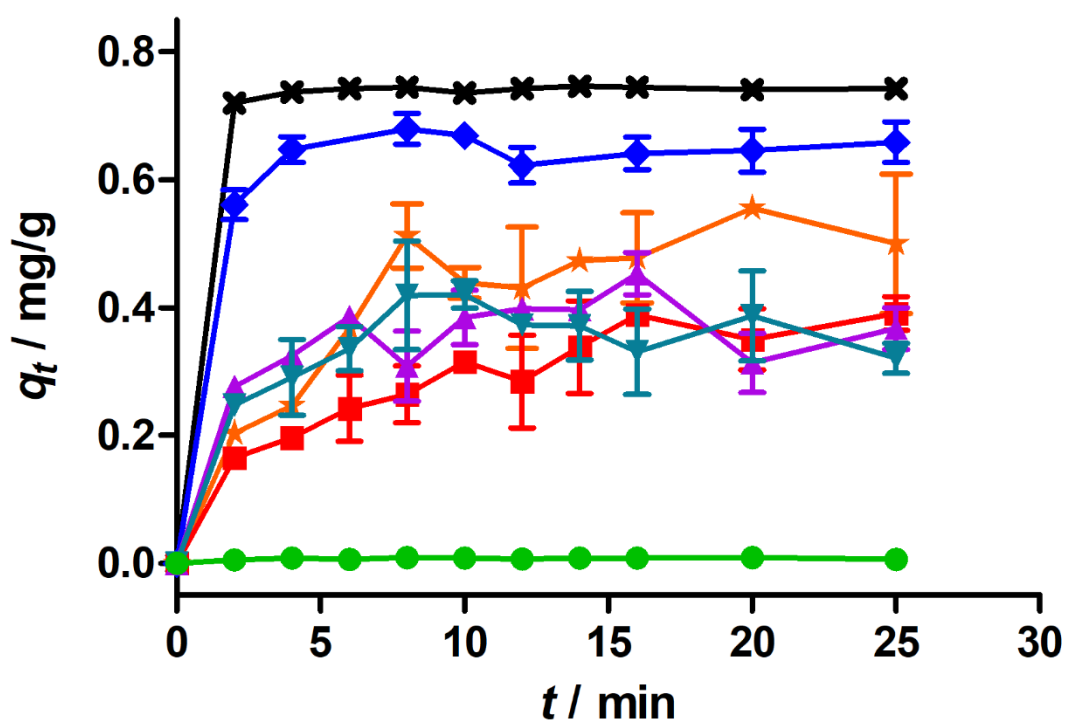


**Figure S1.** TGA of Cu-BTC and the polymer. Legend: — Cu-BTC, — polymer. For the Cu-BTC, the initial mass drop of about 30%, before reaching 200 °C is due to water loss from the surface and pores of Cu-BTC.<sup>[15]</sup>



**Figure S2.** PXRD of the pure Cu-BTC and the Cu-BTC@polymer after various times of heat treatment. – Cu-BTC, – Cu-BTC@polymer, – Cu-BTC@polymer 200 °C 48 h, – Cu-BTC@polymer 200 °C 72 h.

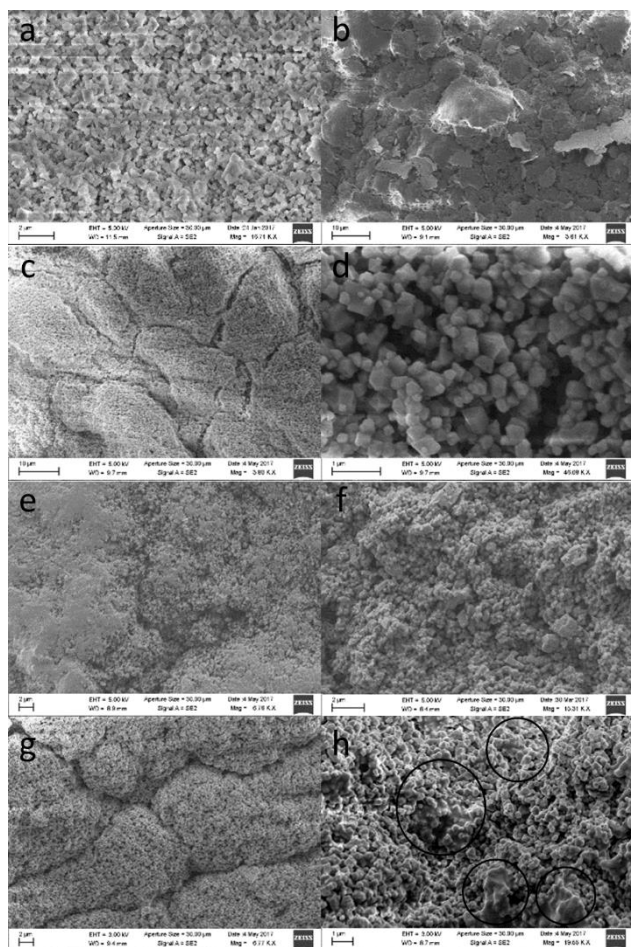
Figure S2 shows that the MOF maintained its crystalline structure during the heating process, while the organic polymer partially decomposed with time.



**Figure S3.** Adsorption curves of MB by the various samples of Cu-BTC and the polymer.

Legend:  $\times$  Cu-BTC,  $\blacksquare$  Cu-BTC@polymer,  $\blacklozenge$  Cu-BTC@polymer 3D printed net,  $\star$  Cu-BTC@polymer 3D printed layered-cylinders,  $\blacktriangle$  Cu-BTC@polymer 200 °C 48 h,  $\blacktriangleleft$  Cu-BTC@polymer 200 °C 72 h,  $\bullet$  Only polymer.

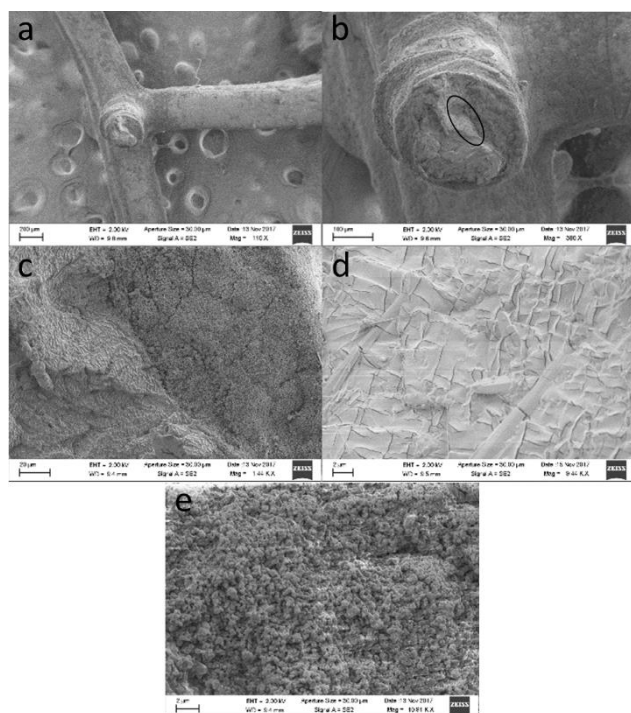




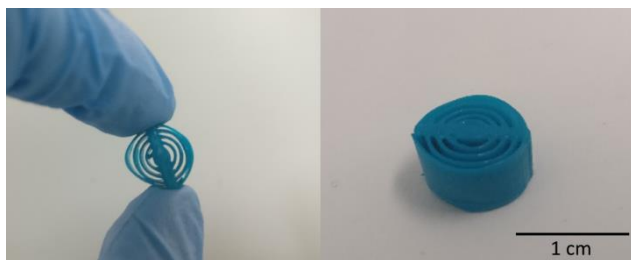
**Figure S4.** SEM images of the a) Cu-BTC crystals before addition to the formulation. b,c) SEM images of the surface area of Cu-BTC@polymer before heating. d) The Cu-BTC crystals on the surface of the polymerized model. e,f) Cu-BTC@polymer after 200 °C 48 h. g) Cu-BTC@polymer after 200 °C 72 h. h) The areas of MOF covered with polymeric residues are marked with circles. A statistical analysis of the MOFs particles sizes was performed for figures S4a and S4d and it was found that the average crystals size before addition to the formulation was  $361 \pm 160$  nm, while after formation of the polymer it was  $263 \pm 98$ . Although there is a certain overlap of the average sizes, the difference may result from the sonication of the formulation in its preparation process, which may break the crystals into smaller particles.

Figure S4 indicates that the polymerized model before heating was partially smooth (Figure S4b) and partially porous (Figure S4c). As expected, in those porous areas the Cu-BTC

nanometric crystals could be observed on the surface (Figure S4d). Following heating for 42 h, a larger portion of the surface became porous (Figures S4e and S4f), and after 72 h of heating at 200 °C most of the surface seemed to be porous (Figure S4g). However, in Figure S4h, large areas can be seen in which the nanocrystals are covered with a thin amorphous layer, which might be the polymeric residues that cover and block some of the Cu-BTC and its pores. This might be the reason for the un-changed MB adsorbance over increasing heating periods.



**Figure S5.** SEM images of a) A junction of the 3D printed net. b) A cross section of the printed net. The circled area is the interface between the polymer rich area and the crystals rich area. c) A close-up of the circled area in Figure 5b in which the interface of the two areas can be seen. d) The polymer rich area. e) The crystals rich area.



**Figure S6.** 3D printed layered-cylinders of Cu-BTC@polymer.

**Table S1.** Printing parameters for 3D printing of Cu-BTC@polymer.

Parameter	Value
Light Intensity	40.974 [mW/cm <sup>2</sup> ]
Slice thickness	0.100 [mm]
Burn-In Exposure Time	25.000 [s]
Exposure Time	2.000 [s]
Separation Velocity	1.000 [mm/s]
Separation Distance	5.000 [mm]
Approach Velocity	2.000 [mm/s]
Slides Per Layer	1.000
Slide Velocity	10.000 [mm/s]
Burn-In Wait Time (After Exposure)	5.000 [s]
Burn-In Wait Time (After Separation)	5.000 [s]
Burn-In Wait Time (After Approach)	0.000 [s]
Burn-In Wait Time (After Slide)	0.000 [s]
Normal Wait Time (After Exposure)	3.000 [s]
Normal Wait Time (After Separation)	3.000 [s]
Normal Wait Time (After Approach)	0.000 [s]
Normal Wait Time (After Slide)	0.000 [s]

**Table S2.** Cu-BTC quantity in measured samples.

Sample	Total mass of the sample [mg]	Cu-BTC percentage of the entire sample	Mass of Cu-BTC in the sample [mg]
Powder Cu-BTC	10	100%	10
Cu-BTC@polymer	100	10%	10
Cu-BTC@polymer after 48 h at 200 °C (34.6% weight loss)	66.4	~15.1%	10
Cu-BTC@polymer after 72 h at 200 °C (39.4% weight loss)	60.6	~16.5%	10
Only polymer	100	0%	0

## References

- [1S] Y. T. Wang, Y. Y. Lu, W. W. Zhan, Z. X. Xie, Q. Kuang and L. S. Zheng, *J. Mater. Chem. A*. **2015**, 3, 12796.



## **2.2. Chapter 2: Nuclear Wastewater Decontamination by 3D-Printed Hierarchical Zeolite Monoliths**

Published<sup>67</sup>: Halevi O., Chen T.Y., Lee P.S., Magdassi S., Hriljac J.A. Nuclear wastewater decontamination by 3D-Printed hierarchical zeolite monoliths. *RSC Advances* **10**, 5766 (2020).



## PAPER

Cite this: *RSC Adv.*, 2020, 10, 5766

# Nuclear wastewater decontamination by 3D-Printed hierarchical zeolite monoliths†

Oded Halevi,<sup>‡,def</sup> Tzu-Yu Chen,<sup>id</sup> <sup>‡,ac</sup> Pooi See Lee,<sup>id</sup> <sup>\*df</sup> Shlomo Magdassi<sup>id</sup> <sup>\*de</sup> and Joseph A. Hriljac<sup>id</sup> <sup>\*ab</sup>

The selective removal of radioactive cationic species, specifically  $^{137}\text{Cs}^+$  and  $^{90}\text{Sr}^{2+}$ , from contaminated water is critical for nuclear waste remediation processes and environmental cleanup after accidents, such as the Fukushima Daiichi Nuclear Power Plant disaster in 2011. Nanoporous silicates, such as zeolites, are most commonly used for this process but in addition to acting as selective ion exchange media must also be deployable in a correct physical form for flow columns. Herein, Digital Light Processing (DLP) three-dimensional (3D) printing was utilized to form monoliths from zeolite ion exchange powders that are known to be good for nuclear wastewater treatment. The monoliths comprise 3D porous structures that will selectively remove radionuclides in an engineered form that can be tailored to various sizes and shapes as required for any column system and can even be made with fine-grained powders unsuitable for normal gravity flow column use. 3D-printed monoliths of zeolites chabazite and 4A were made, characterized, and evaluated for their ion exchange capacities for cesium and strontium under static conditions. The 3D-printed monoliths with 50 wt% zeolite loadings exhibit Cs and Sr uptake with an equivalent ion-capacity as their pristine powders. These monoliths retain their porosity, shape and mechanical integrity in aqueous media, providing a great potential for use to not only remove radionuclides from nuclear wastewater, but more widely in other aqueous separation-based applications and processes.

Received 28th November 2019  
Accepted 27th January 2020

DOI: 10.1039/c9ra09967k

rsc.li/rsc-advances

## 1. Introduction

Nuclear power plants generate about 11% of world electricity today.<sup>1</sup> Although nuclear fission is environmentally benign in the sense of not producing any carbon emissions, it is of course necessary to deal with the nuclear waste that is produced and be able to rapidly respond to and mitigate the effects of accidental releases of radionuclides to the environment such as the disasters that occurred at Chernobyl in 1986 and the Fukushima Daiichi plant in 2011. The source for the majority of the medium-lived radiation in spent fuels are two radionuclides,  $^{137}\text{Cs}$  and  $^{90}\text{Sr}$ , which both have high fission yields and half-lives

of around 30 years. As the two radionuclides form many soluble salts, they are most likely to contaminate water bodies. In addition, given the relatively high volatility of cesium salts, it is the species that spreads most widely in the environment after accidental releases. For example, the Fukushima accident released approximately 10 PBq of  $^{137}\text{Cs}$  into environment,<sup>2</sup> the removal of this radionuclide continues to be a significant part of cleanup.

For more than 40 years, aluminosilicate zeolites have been playing an important role as ion exchange media for nuclear waste treatment by selective removal of cesium and strontium from wastewater. In 1985 British Nuclear Fuels Limited (BNFL) successfully commissioned the Site Ion Exchange Effluent Plant (SIXEP) at Sellafield, which uses a naturally occurring zeolite, clinoptilolite, to remove cesium and strontium from all water bodies before discharge into the sea.<sup>3</sup> This led to a dramatic decrease in the contamination of effluent. Two other zeolites which show good selectivity for  $\text{Cs}^+$  and  $\text{Sr}^{2+}$  are chabazite and zeolite 4A. Chabazite is found naturally as a sodium-rich form (herschelite) and shows good selectivity for  $\text{Cs}^+$  and moderate selectivity for  $\text{Sr}^{2+}$ .<sup>4,5</sup> Dyer and Zubair have shown that the selectivity is thermodynamically favorable for many cations ( $\text{Na}^+$ ,  $\text{K}^+$ ,  $\text{Rb}^+$ ,  $\text{Mg}^{2+}$ ,  $\text{Ca}^{2+}$ ,  $\text{Sr}^{2+}$  and  $\text{Ba}^{2+}$ ) and generally correlates with the size difference between  $\text{Cs}^+$  and the replaceable cation.<sup>6</sup> It has been widely used in clean-up efforts at Three Mile Island,

<sup>a</sup>School of Chemistry, University of Birmingham, Edgbaston, Birmingham, B15 2TT, UK

<sup>b</sup>Diamond Light Source Ltd, Harwell Science and Innovation Campus, Didcot, OX11 0DE, UK. E-mail: joseph.hriljac@diamond.ac.uk

<sup>c</sup>Materials and Engineering Research Institute, Faculty of Science, Technology and Arts, Sheffield Hallam University, City Campus, Howard Street, Sheffield, S1 1WB, UK

<sup>d</sup>CREATE NTU-HUJ Programme, Enterprise Wing, 138602, Singapore

<sup>e</sup>Casali Center for Applied Chemistry, Institute of Chemistry, The Hebrew University of Jerusalem, Jerusalem, 91904, Israel. E-mail: magdassi@mail.huji.ac.il

<sup>f</sup>School of Materials Science and Engineering, Nanyang Technological University, 639798, Singapore. E-mail: pslee@ntu.edu.sg

† Electronic supplementary information (ESI) available. See DOI: 10.1039/c9ra09967k

‡ O. H. and T.-Y. C. contributed equally to this work.



Chernobyl and Fukushima. Synthetic zeolite A in the sodium form (commercially known as zeolite 4A), has a polyhedral open-cage structure with pores roughly 4 Å in size and most of the cation sites are accessible. The sodium ions can be fully exchanged, showing better selectivity towards smaller metal cations, such as  $\text{Sr}^{2+}$ .<sup>7</sup> The selectivity of  $\text{Sr}^{2+}$  over  $\text{Na}^+$  or  $\text{K}^+$  has been attributed to the high framework charge and, hence, strong electrostatic attraction of the divalent cation to the framework.<sup>8</sup> Nuclear waste treatment can be demanding, in some cases the radionuclides must be removed from highly radioactive solutions that are also extremely acidic or caustic, where natural zeolites suffer due to their nature as aluminosilicates. Various synthetic materials such as titano-, zircono-silicates<sup>9–11</sup> or metal oxides<sup>12,13</sup> have been developed and proved more useful in these cases.

Synthetic ion exchangers can be produced with a wide variety of tailored chemical properties and ion exchange selectivity in the laboratory, but certain physical and mechanical characteristics may limit their applicability and efficiency for actual use. Therefore, most candidate materials do not make it from the bench into a plant. One of those limitations is when the material is only available as a fine-grained loose powder, such as many microporous solids that are produced with a particle size from sub-micron to a few tens of microns. Although they have a high surface area, which is beneficial for fast ion exchange, they might be packed very tightly in columns which can lead to reduced flow rates and ultimately leading to a flow blockage.<sup>14</sup> They are also more difficult to handle and can form radioactive dusts during dry handling and disposal after use. It is for this

reason that the naturally sourced aggregate SIXEP clinoptilolite is crushed and sieved so that only particles between 0.4 and 0.8 mm are put into the columns.<sup>15</sup> For fine-grained synthetic materials this is not an option, so binder materials must be used to produce beads embedded with the zeolite to retain good mechanical strength. For example IONSIV® R9120-B is a commercial crystalline silicotitanate (CST) powder produced in bead form using the inorganic binder  $\text{Zr}(\text{OH})_4$ ,<sup>16,17</sup> which is compatible with potential final waste forms and processes such as vitrification.

In this report, we present a new approach that provides a breakthrough solution to the above problems, based on the fabrication of ion exchanger monoliths by three-dimensional (3D) printing. 3D-printing is an emerging technology, offering various methods for fabrication of objects of varying size, shape and complexity. The common denominator of all 3D-printing methods is the layer by layer deposition of materials, to form a 3D solid object.<sup>18</sup> This printing technology is being utilized for manufacturing and prototyping in many fields such as construction,<sup>19</sup> microfluidics,<sup>20</sup> and soft robotics.<sup>21</sup> It is also used to form complex structures of polymers, embedded with functional materials, thus bringing additional functionalities to the printed structures. Such functional 3D-printing has been demonstrated for example with graphene and carbon nanotubes to form conductive objects,<sup>22</sup> ceramic nanoparticles for piezoelectric applications,<sup>23</sup> and metal-organic frameworks to form gas adsorbing structures.<sup>24</sup> Monolithic zeolite-containing structures have been produced and used in dry applications such as gas adsorption,<sup>25</sup> gas separation,<sup>26,27</sup> and catalytic

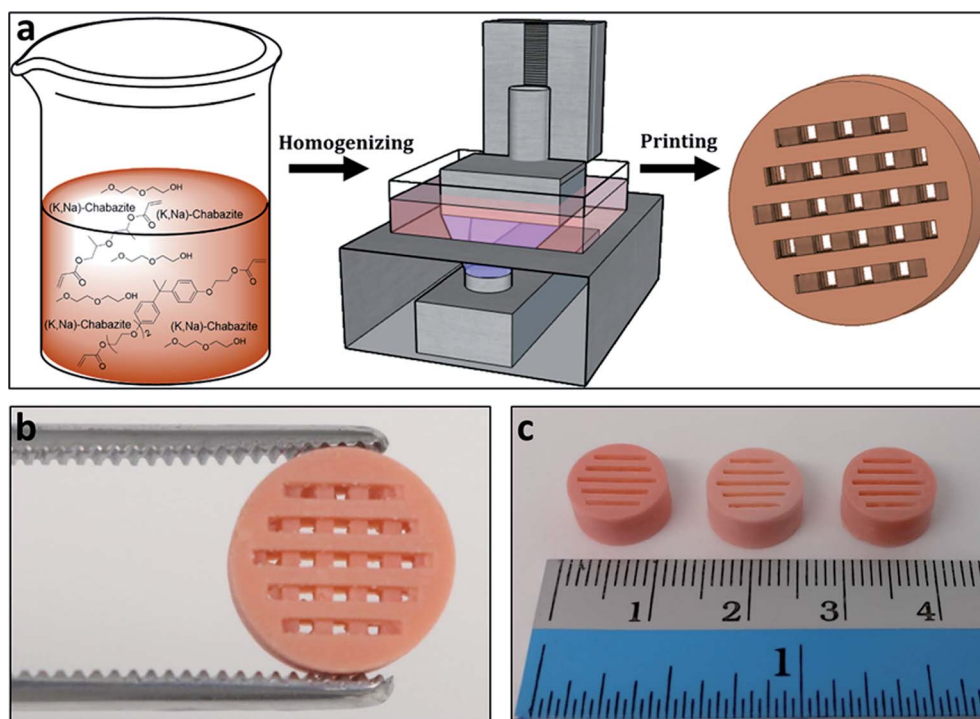


**Fig. 1** (a) Schematic overview of the printing process; first a dispersion of the zeolite was formed within the polymerizable monomers and porogenic solvent, then the formulation was 3D-printed by the DLP method. (b and c) The printed zeolite-embedded monolithic structures.

cracking.<sup>28,29</sup> Recently, a 3D printed metakaolin geopolymer was reported that withstood aqueous ion exchange, this was then used as a precursor to a ceramic monolith with a designed shape.<sup>30</sup>

To date, no 3D-printed zeolite monoliths have been produced specifically for ion exchange of aqueous media where they would need to be both insoluble and stable with regards shape retention over time when exposed to water.<sup>31</sup> Herein, the digital light processing (DLP) method was utilized,<sup>32</sup> which is based on UV-polymerization of each layer to form the 3D-printed structure. This enables excellent control over the porosity and the physical and chemical properties of the polymeric matrix, making it possible to tailor it according to the specific application requirements. Furthermore, the binder in

this report is an organic polymer, in contrary to the inorganic bentonite clay reported previously, which is not suitable for liquid column flow operation, due to the physical deformation under the flow of liquid.<sup>33</sup> In addition, the commonly used bentonite binder possesses cation-exchange capacity.<sup>34–36</sup> Therefore, when it is used as a binder for screening new ion exchangers in the laboratory scale, it interferes with the screening of the retention and selectivity properties of the selected materials of interests.

The photopolymerizable monomers were mixed with the zeolite powder and were locally polymerized by ultra-violet (UV) light during printing in the presence of a porogenic solvent. The variety of available photopolymerizable monomers enables tailoring of the binder's physical and chemical properties such

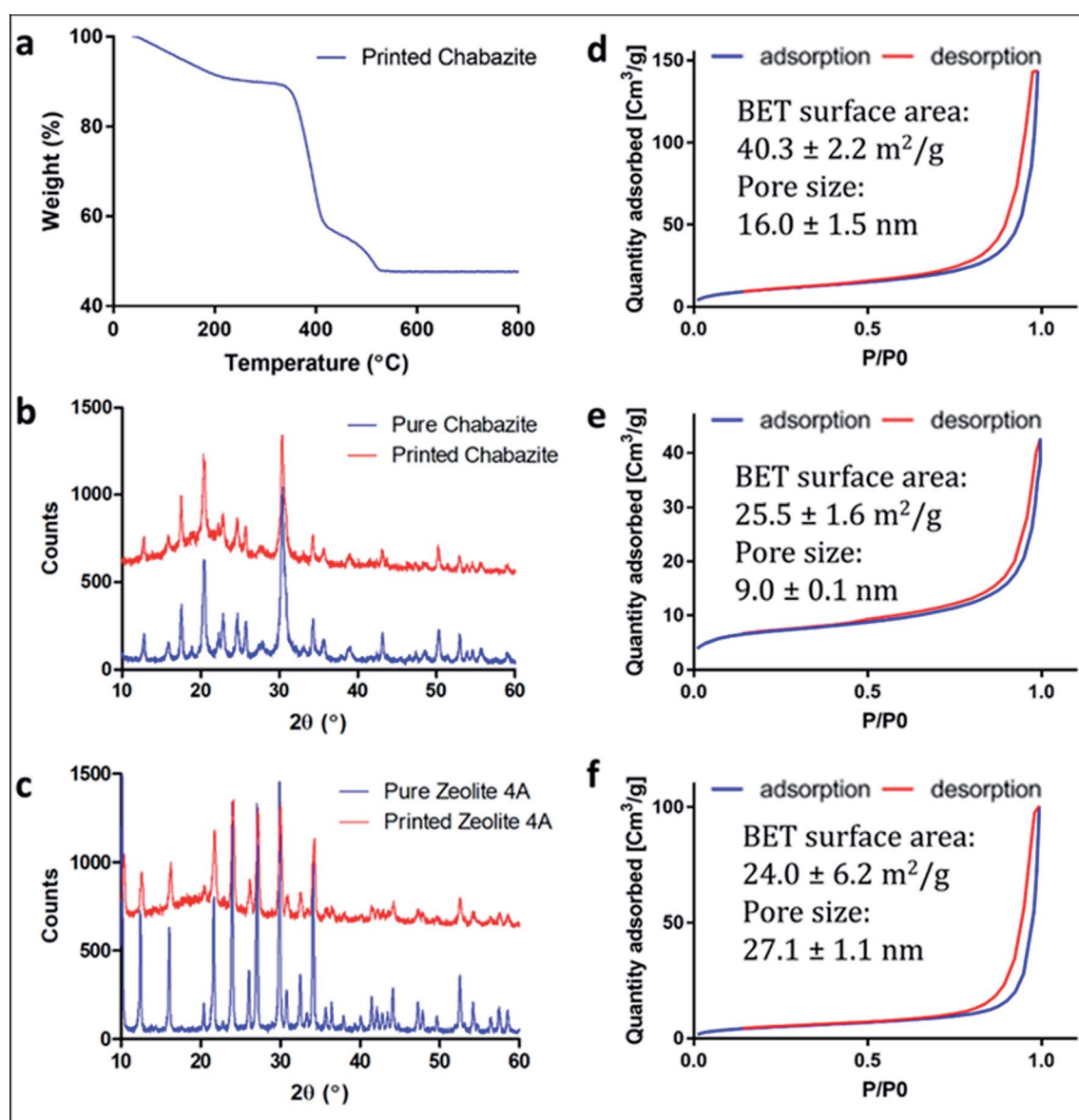


Fig. 2 (a) TGA curve of 3D-CHA. (b and c) Comparison between the PXRD of zeolite powders and the zeolite embedded printed structures (b) 3D-CHA and pure chabazite powder; (c) 3D-4A and pure zeolite 4A powder. The patterns of the printed systems have been offset for clarity. (d–f) N<sub>2</sub> adsorption isotherms of (d) 3D-CHA; (e) the pure chabazite powder; (f) the printed polymer.

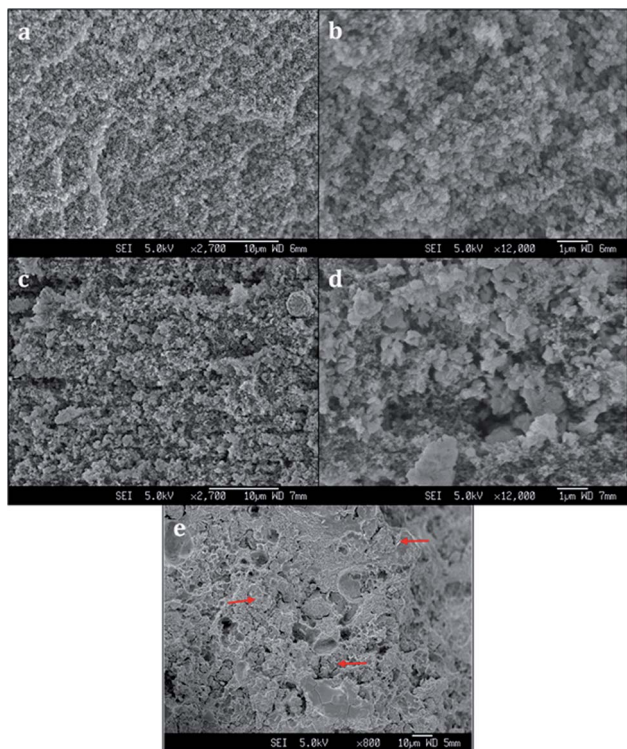


Fig. 3 SEM images of (a and b) 3D-printed polymer, (c and d) 3D-CHA monolith, (e) 3D-4A monolith.

as stretchability,<sup>37</sup> temperature responsiveness,<sup>38</sup> and hydrophobicity.<sup>39</sup> The use of the porogenic solvent enables formation of a porous 3D structures,<sup>40</sup> which is a crucial factor for maintaining the accessibility and functionality of the zeolite powder in the composite. The 3D monoliths have a hierarchical structure so that they are readily useable for liquid flow separation experiments, due to the design of cross-channels along the cylinder radius that connects the channels running along the cylinder length. Two zeolites, synthetic chabazite and commercial zeolite 4A, were printed and the hierarchical monoliths were evaluated to establish that the zeolites remain intact and retain the ability to remove Cs and Sr from aqueous solution. Depending upon the choice of ion exchanger, the target ions for removal do not have to be radionuclides, hence this technology could be readily adapted to removal of other

cations such as environmentally damaging heavy metals or ammonia.

## 2. Results and discussion

### 2.1 Formulation preparation and 3D-printing

Polymeric cylindrical monolithic nets, embedded with chabazite (3D-CHA) or zeolite 4A (3D-4A), have been printed using the DLP method (Fig. 1a). For optimal performance of the zeolite in an ion-exchange column configuration, the printed structure should enable the flow of the solution through the column, and the polymeric matrix should allow the access of the cations from the feed to the surface of the zeolite particles, so that they can exchange into the pores of the embedded zeolite. Therefore, each object was printed as a porous cylindrical net, as seen in Fig. 1b and c. The cylinders can be stacked to the required height providing adaptability in practice.

To enable maximal accessibility and prevent the polymer from blocking the zeolite active sites, a high surface area of the polymer was required. As reported earlier, the overall porosity of the polymer can be controlled mainly by tailoring the fraction of the porogenic solvent and the concentration of the cross-linker monomer.<sup>40,41</sup> The porogenic solvent causes low swelling of the formed polymer with the monomers during the polymerization process. This leads to a later-stage phase separation, which results in smaller pores and a higher surface area. Diethylene glycol monomethyl ether (DM), which is a good solvent for the selected monomers, was chosen as the porogenic solvent. The concentration of the cross-linker should affect the pores size as well. A higher cross-linker concentration would lead to a higher surface area.<sup>42</sup> Consequently, bifunctional acrylate monomers were chosen: ethoxylated (3) bisphenol A dicrylate (SR-349) as the main monomer, and dipropylene glycol diacrylate (SR-508) that was added to decrease the viscosity of the formulation, to enable printing at high quality. Since the printing is based on photopolymerization, the printing composition contained a photoinitiator, diphenyl(2,4,6-trimethylbenzoyl)phosphine oxide (TPO), as well as a pigment (Orasol orange 272), to obtain a high printing resolution. The weight concentration of the zeolite in the starting formulation was 25 wt% to yield solid printed structures with 45–50 wt% zeolite. Thermal gravimetric analysis (Fig. 2a) of a 3D-CHA sample showed several stages of weight loss upon heating, due to dehydration of the zeolite and

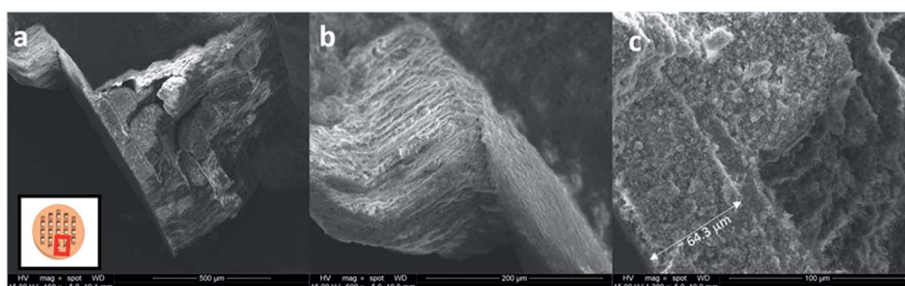


Fig. 4 SEM images of Cs-exchanged 3D-printed monolith (a) an overview (b) side view (c) top view of the rod taken from the grid.



decomposition of the polymer, giving a final 47.7% remaining weight after heating above 600 °C.

## 2.2 Structural characterization of the printed models

Powder X-ray diffraction (PXRD) measurements of the original zeolite powders and portions of crushed 3D monoliths verified that the zeolite crystal structures were not altered during the fabrication process (Fig. 2b and c). The higher backgrounds from *ca.* 10–30° for the printed systems are due to the presence of the amorphous polymeric phase. A minor decrease in crystallinity of the zeolites, indicated by peak broadening, was also observed.

Fig. 2d–f show the nitrogen adsorption isotherms of printed samples degassed at 70 °C (we did not apply higher temperature in order to avoid polymer deformation). The low BET surface area in the chabazite sample results from blockage of the channels for N<sub>2</sub> at 77 K by the solvent, and the incomplete clearance in the pores at such low degassing temperature. This claim will be confirmed later in this paper, by ion-exchange tests in solutions. All of the three samples show similarity in the shape of isotherms for the monoliths and the pristine powder, as well as H3-type hysteresis loops, which indicate the mesoporous nature of the 3D-printed monoliths. The microporous structure could not be identified due to the low degassing temperature.

## 2.3 Morphologies of the printed models

Scanning electron microscopy (SEM) images reveal a porous structure in the printed polymer (Fig. 3a and b). The voids are uniform and sized in the sub-micrometer scale. The SEM image of the chabazite-embedded monolith (Fig. 3c and d) shows that the chabazite grains are distributed evenly within the porous polymeric matrix. The zeolite 3D-4A (Fig. 3e) was printed with the same composition of polymer. The microcrystals of zeolite 4A, indicated with arrows, were well embedded in the polymer matrix. However, it shows a much denser morphology compared to 3D-CHA. The texture is less fluffy, and more agglomerates were observed.

## 2.4 Ion exchange tests

In order to verify the removal of Cs or Sr and investigate the mechanical integrity, the printed objects were tested for ion exchange and characterized using SEM-EDX, Infinite Focus Microscopy (IFM), XRD and X-ray Fluorescence (XRF) spectroscopy.

Fig. 4 shows the morphologies of Cs-exchanged 3D-CHA printed monolith after shaking in aqueous solution for 24 hours. A rod was taken from the grid for SEM observation as shown in the inset of Fig. 4a. This demonstrates that the printed structures are retained intact after ion exchange and the porous texture of each layer is consistent. Chabazite is uniformly

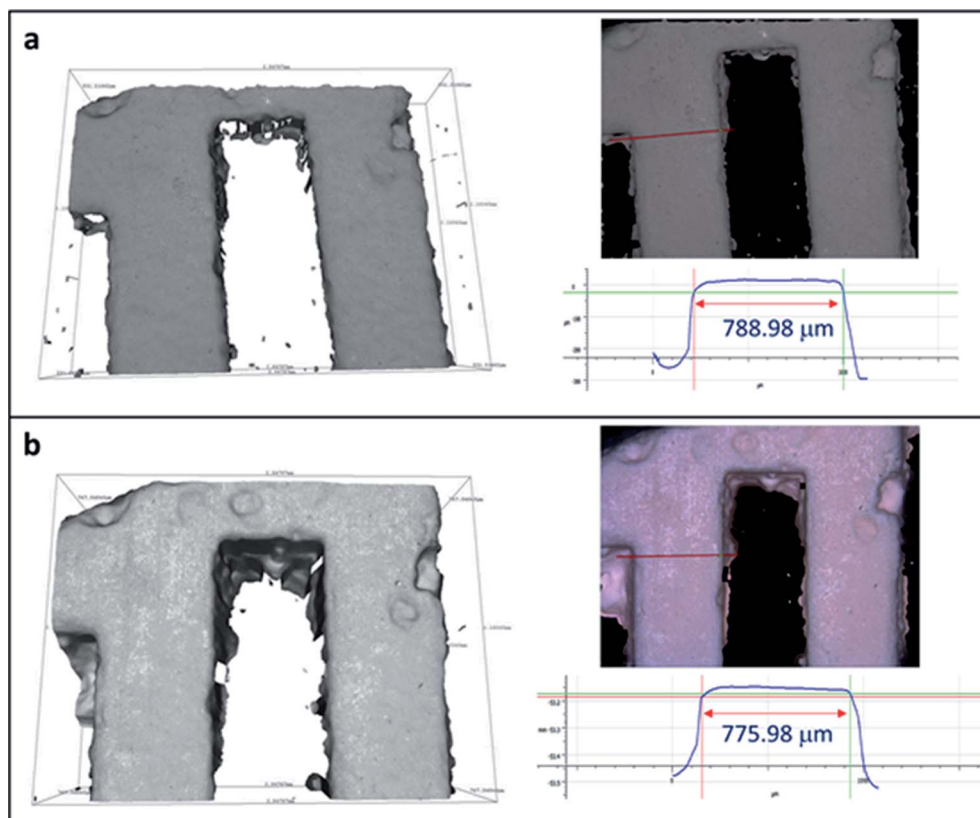


Fig. 5 IFM images of 3D-printed monolith (a) before and (b) after Cs ion exchange and their profile measurements.

blended into the polymer matrix and the rough surfaces of all sides of the rod and each porous layer allow the aqueous media to access through the pellet, as shown in Fig. 4b and c. It also demonstrates the excellent resolution of the DLP technique (Fig. 4c) enabling 3D printing to fabricate an object detailed to  $\sim 60 \mu\text{m}$ .

3D printed monoliths were subjected to IFM for investigating the robustness of the monoliths after being shaking in water media. Since the ion exchangers used in the nuclear industry will be immobilized rather than regenerated and reused to avoid risk of spreading the hazards, the integrity investigation was done after one cycle. A region with non-smooth sites was chosen for the ease of observation using IFM. Because the microscope adopts focus-variation principle, there needs to be sufficient contrast on the surface to obtain a meaningful measurement. As seen in Fig. 5, the surface textures remain identical before and after ion exchange. Their profile measurements based on surface metrology using IFM show that the shape and width of the selected area were retained after ion exchange. The error in the length of the bar is due to the difficulty of manually selecting the same profile at every observation for calculations.

Cs and Sr adsorption by the 3D-printed polymer matrix on its own was also tested as a control (Table S1†). From the XRF

results, the polymer matrix itself does not exhibit any significant adsorption of either Cs or Sr. XRF data were collected for the pristine zeolite powders and two separate batches of 3D monoliths before and after exposure to Cs and Sr solutions (Tables 1 and 2). As absolute weight percentages vary depending upon many factors, the relative atomic ratios of elements, normalized to Al, have been calculated and are used for comparison. For all chabazite samples (Table 1), as expected, the Si/Al ratio remains the same at around  $2.48 \pm 0.15$ . For the chabazite samples before ion exchange, both Na and K are present as charge-balancing cations and the sum of their ratios to Al should equal to 1. The ratios are 1.06, 1.24 and 1.10 for the pristine powder, 3D-CHA monolith 1 and 3D-CHA monolith 2, respectively (Table 1). Given the fact that the data were collected on loose powders and many of the fluorescence lines are low energy, this is within acceptable error. After the Cs-exchange process, there is clear evidence of cesium uptake and loss of Na and K. The cation sums are 1.58, 2.39 and 2.83, respectively. These may be high due to an over-determination of the amount of cesium or indicate that in addition to the ion exchange uptake of the zeolite, a small amount of an insoluble cesium salt has formed. The determination of elements that fluoresce at higher energies, such as cesium vs. sodium, are often over-estimated for thin samples as used here, as the thickness is

**Table 1** Elemental composition of 3D-printed and powdered chabazite before and after ion exchange, analyzed using XRF

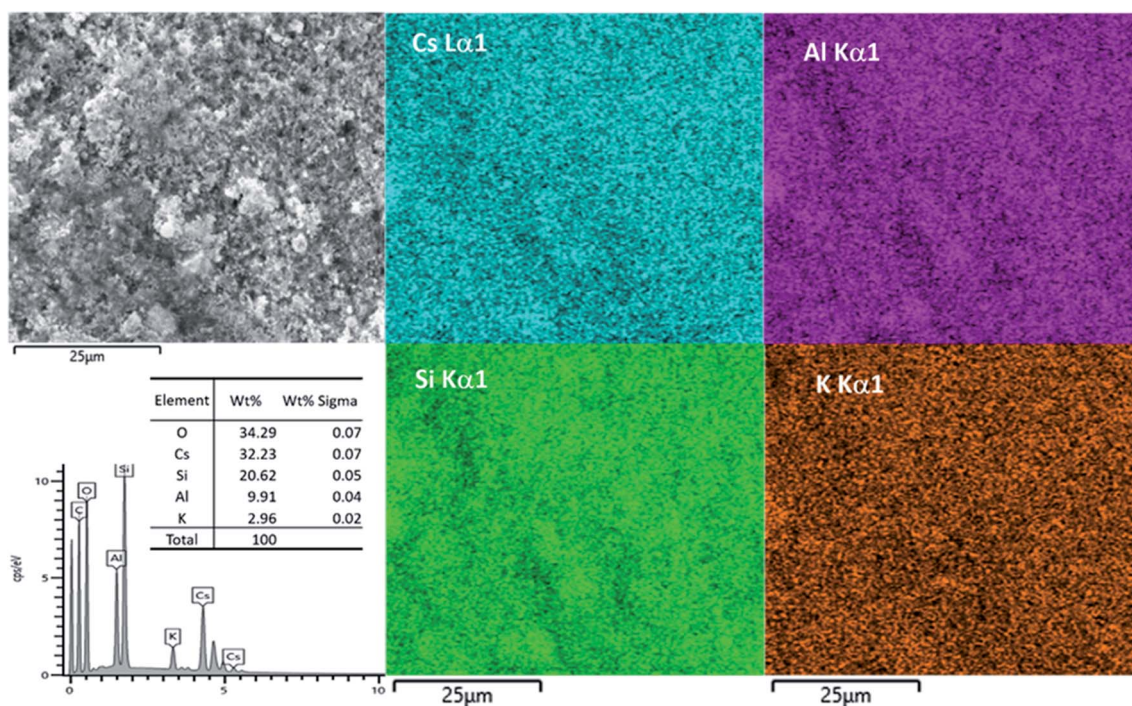
	Before ion exchange		Cs exchanged		Sr exchanged	
Element	wt%	Atomic ratio (normalised to Al)	wt%	Atomic ratio (normalised to Al)	wt%	Atomic ratio (normalised to Al)
Powder (K, Na)-chabazite						
Cs			17.84%	1.33		
Sr					8.92%	0.65
Si	18.33%	2.47	6.80%	2.39	8.22%	2.21
Al	7.12%	1	2.73%	1	3.87%	1
K	5.71%	0.55	1.01%	0.26	0.74%	0.13
Na	3.07%	0.51				
	Si/Al = 2.47		Si/Al = 2.39		Si/Al = 2.21	
	(K + Na)/Al = 1.06		(K + Cs)/Al = 1.58		(K + 2Sr)/Al = 1.44	
3D-CHA monolith 1						
Cs			24.67%	2.07		
Sr					6.79%	0.77
Si	6.62%	2.69	6.04%	2.40	6.21%	2.62
Al	2.36%	1	2.42%	1	2.49%	1
K	2.85%	0.83	1.14%	0.33	0.66%	0.18
Na	0.82%	0.41				
	Si/Al = 2.69		Si/Al = 2.40		Si/Al = 2.62	
	(K + Na)/Al = 1.24		(K + Cs)/Al = 2.39		(K + 2Sr)/Al = 1.54	
3D-CHA monolith 2						
Cs			24.07%	2.44		
Sr					6.53%	0.83
Si	7.86%	2.54	4.98%	2.39	6.03%	2.45
Al	2.97%	1	2.00%	1	2.22%	1
K	3.20%	0.74	1.12%	0.39	0.63%	0.18
Na	0.91%	0.36				
	Si/Al = 2.54		Si/Al = 2.39		Si/Al = 2.61	
	(K + Na)/Al = 1.10		(K + Cs)/Al = 2.83		(K + 2Sr)/Al = 2.01	

**Table 2** Elemental composition of 3D-printed and powdered zeolite 4A before and after ion exchange, analyzed using XRF

Element	Before ion exchange		Cs exchanged		Sr exchanged	
	wt%	Atomic ratio (normalised to Al)	wt%	Atomic ratio (normalised to Al)	wt%	Atomic ratio (normalised to Al)
<b>Powder zeolite 4A</b>						
Cs			21.30%	1.05		
Sr					7.81%	0.61
Si	14.80%	1.08	4.49%	1.05	4.25%	1.0
Al	13.20%	1	4.12%	1	3.95%	1
Na	9.08%	0.81	2.31%	0.66	0.44%	0.13
	Si/Al = 1.08		Si/Al = 1.04		Si/Al = 1.03	
	Na/Al = 0.81		(Na + Cs)/Al = 1.71		(Na + 2Sr)/Al = 1.35	
<b>3D-4A monolith 1</b>						
Cs			22.41%	1.31		
Sr					5.87%	0.51
Si	9.67%	1.14	3.64%	1.01	4.15%	1.12
Al	8.14%	1	3.47%	1	3.55%	1
Na	5.68%	0.82	1.60%	0.54	0.81%	0.27
	Si/Al = 1.14		Si/Al = 1.01		Si/Al = 1.12	
	Na/Al = 0.82		(Na + Cs)/Al = 1.85		(Na + 2Sr)/Al = 1.29	
<b>3D-4A monolith 2</b>						
Cs			14.64%	0.76		
Sr					4.59%	0.38
Si	9.51%	1.17	4.46%	1.09	4.54%	1.18
Al	7.80%	1	3.92%	1	3.71%	1
Na	5.30%	0.80	2.13%	0.65	1.14%	0.36
	Si/Al = 1.17		Si/Al = 1.09		Si/Al = 1.18	
	Na/Al = 0.80		(Na + Cs)/Al = 1.40		(Na + 2Sr)/Al = 1.12	

insufficient for the assumption that all elements are present to an infinite thickness. The situation for Sr-exchange is identical, and as it is a divalent cation, the key sum is twice the Sr/Al ratio

added to the other cation/Al ratios and these are 1.44, 1.54 and 2.01 for the pristine powder, 3D-CHA monolith 1 and 3D-CHA monolith 2, respectively. Critically, the 3D monoliths

**Fig. 6** SEM image, EDX results and elemental mapping of Cs-exchanged 3D-CHA.

**Table 3** Unit cell parameters of the pre- and post-ion exchanged 3D-CHA and 3D-4A

	Crystal system	Space group	<i>a</i> [Å]	<i>b</i> [Å]	<i>c</i> [Å]	<i>V</i> [Å <sup>3</sup> ]
3D-CHA	Rhombohedral	<i>R</i> $\bar{3}m$	13.8321 (11)	13.8321 (11)	15.1547 (22)	2510.0 (6)
Cs-exchanged 3D-CHA	Rhombohedral	<i>R</i> $\bar{3}m$	13.8680 (8)	13.8680 (8)	15.1188 (18)	2518.1 (4)
Sr-exchanged 3D-CHA	Rhombohedral	<i>R</i> $\bar{3}m$	13.7826 (5)	13.7826 (5)	15.2636 (16)	2511.0 (3)
3D-4A	Cubic	<i>Pm</i> $\bar{3}m$	12.2839 (7)	12.2839 (7)	12.2839 (7)	1853.6 (3)
Cs-exchanged 3D-4A	Cubic	<i>Pm</i> $\bar{3}m$	12.3016 (4)	12.3016 (4)	12.3016 (4)	1861.6 (2)
Sr-exchanged 3D-4A	Cubic	<i>Pm</i> $\bar{3}m$	12.3013 (3)	12.3013 (3)	12.3013 (3)	1861.4 (2)

maintained their own shape after one day of shaking in solution, and no colloidal particles were observed after ion exchange. From Table 1, 3D-CHA behaves the same as the original form, and their Cs and Sr uptakes are proportional to the zeolite content. This also supports our claim that the low measured BET surface area was due to the low degassing temperature, and not due to blockage of the pores by the polymer. Based on these results, it can be concluded that the 3D-printing does not affect the ion exchange features in chabazite, and that its ion-capacity and performance are comparable to that of the zeolite only, but without the hazards associated with the powder form.

An attempt was made to use SEM-EDX-mapping to provide a better insight than XRF into the elemental distribution within the matrix. EDX maps of Cs-exchanged 3D-CHA are shown in Fig. 6. Unfortunately, chabazite is uniformly blended into the polymeric matrix and due to the very fine particle size, EDX-mapping could not distinguish regions of zeolite from polymeric matrix. The elemental composition of the Cs-exchanged CHA was measured and the Si/Al ratio from the average of five selected areas is  $2.05 \pm 0.05$  and the (Na + K + Cs)/Al ratio is  $0.99 \pm 0.11$ , these are closer to the expected values than observed with XRF.

For all 4A samples, before and after ion exchange, the Si/Al ratio remains around  $1.09 \pm 0.06$  (Table 2). For the zeolite 4A samples before ion exchange, Na is present as the charge-balancing cation and the sum of its ratio to Al should equal 1. It was noticed that cation/Al ratios were under-determined for samples before ion exchange and over-determined after Cs or Sr

change. After the Cs and Sr-exchange process, there is clear evidence of Cs/Sr uptake and loss of Na. However, after one day of static ion exchange, none of the zeolite 4A samples was fully exchanged. Zeolite 4A exhibits better uptake towards smaller metal cations ( $\text{Sr}^{2+}$ ) than larger alkali metal cations ( $\text{Cs}^+$ ), and this phenomenon is consistent to all the powdered zeolite 4A or 3D-4A monoliths.

An additional way to assess cation exchange in zeolites is to examine changes in the X-ray powder diffraction patterns. For 3D-CHA, the Cs- and Sr-exchanged samples remain with the same crystal structure and slightly bigger unit cells (Table 3 and Fig. S1†). Ion exchange typically results in a noticeable change in intensities due to heavy metal cations exchanging with light alkali cations inside the pores. As observed in Fig. 7a, the crystal structure of chabazite remained intact and noticeable changes in the relative intensities and unit cell dimensions were observed for both exchanged 3D materials. This further supports that ion exchange has occurred. Similarly, the crystal structure of zeolite 4A remained unchanged before and after ion exchange (Fig. 7b), and slight bigger unit cell dimensions for Cs and Sr-exchanged 4A were observed. The significant changes in peak intensities also further support the success of cation exchange.

The most common uses of ion exchange media are as packed beds in vessels or columns. A stack of these 3D-printed monoliths can be packed in a customized small-volume column with an engineered inlet, outlet and flow distribution system to allow liquid to percolate through the bed of the medium at a specified flow rate. Fig. 8a represents a schematic diagram for a column

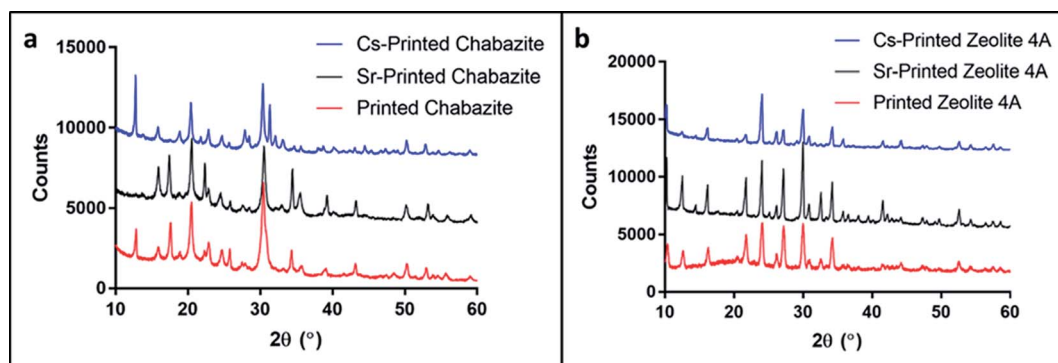


**Fig. 7** PXRD patterns of (a) 3D-CHA and (b) 3D-4A before and after ion exchange with Cs and Sr. The patterns of the printed systems have been offset for clarity.



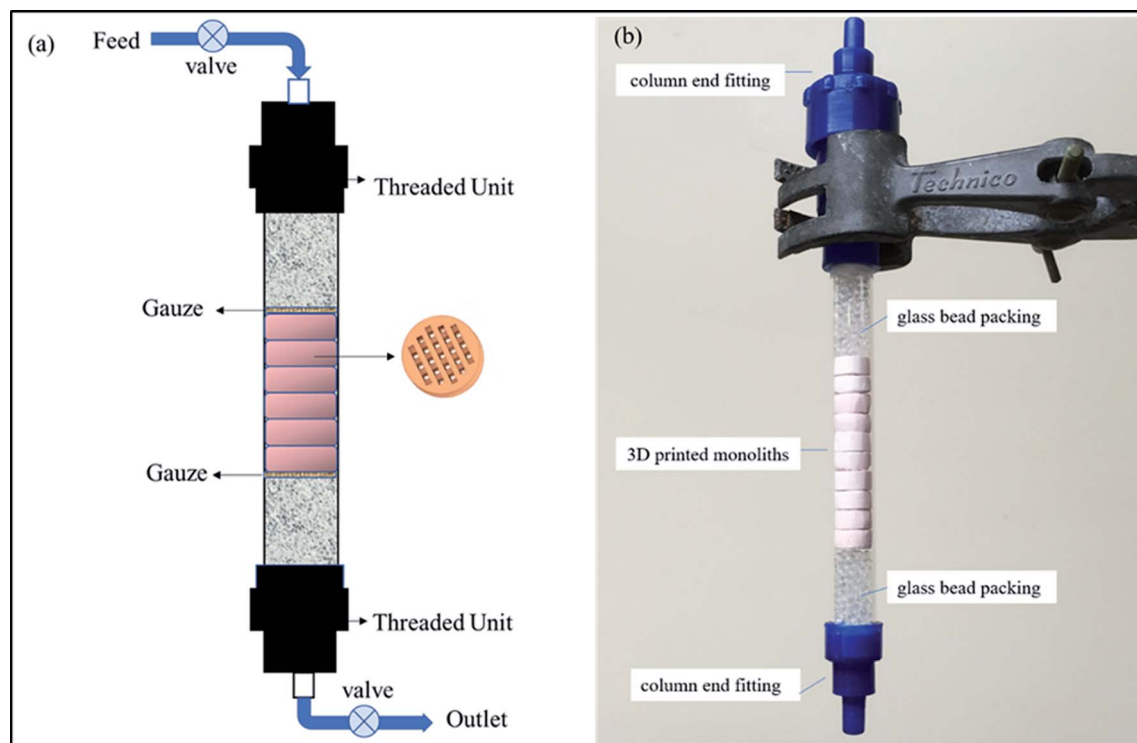


Fig. 8 (a) Schematic diagram of an ion exchange column, (b) photograph of a packed column.

set up, and a photograph of a mock column is presented in Fig. 8b. Retention screens on the inlet and outlet would prevent the medium from escaping into the process loop. After use, the robust monoliths could be readily removed and replaced in a simple operation. An additional advantage of the 3D-printing process is that the pore size and pore system within the monoliths can be tailored to suit the engineering flow requirements.

### 3. Conclusions

In summary, we have successfully demonstrated that 3D-printing enables the fabrication of porous hierarchical zeolite complex structures for utilization in nuclear wastewater decontamination. The monoliths retain the ion exchange properties of the zeolites and possess good mechanical stability. There is no reason to believe that the selectivities towards  $\text{Cs}^+$  and  $\text{Sr}^{2+}$  over other cations in solution will be different for the monoliths over zeolite powders. The DLP 3D-printing process demonstrated in this work enables control over the dimensions and shapes of the zeolite-embedded polymer, and over the degree of porosity and internal structure of the matrix. These features of the process enable its use for other separation processes, which are based on specific adsorption. In the case of nuclear waste treatment, in addition to the above-mentioned advantages, the printed columns enable simple and safe handling of the contaminated ion exchanger and may significantly reduce the risks and difficulties that rise when dealing with radioactive contaminated powders. We have not tested the radiological stability of the polymer matrix, but as the

radioactive cations are trapped within the inorganic zeolite particles we would not expect any release of these into the environment even with polymer degradation. The polymer should also not significantly interfere with the thermal conversion of the spent exchangers into ceramic or vitreous wasteforms as it would be readily oxidized during the process without release of any radionuclides.

## 4. Experimental section

### 4.1 Synthesis of (K, Na)-chabazite

Chabazite was synthesised based on the method reported by the IZA commission.<sup>43,44</sup> A 25 g portion of the ammonium form of zeolite Y (Alfa Aesar) (Powder, S.A.  $750 \text{ m}^2 \text{ g}^{-1}$ , 5.2 : 1 mole ratio) was added into a solution made of water (198.2 mL) and KOH (26.8 mL, 45% solution). The mixture was sealed in a 500 mL polypropylene bottle and shaken for 30 s and then crystallised at  $95^\circ \text{C}$  for 96 h. The product was filtered and thoroughly washed with DI-water. The (K, Na)-chabazite was prepared by repeated ion exchange of the as-synthesized K-chabazite with 1 M NaCl solutions.

### 4.2 Preparation of the printing formulation

The monomers, SR-508 (Sartomer) (1.8 g) and SR-349 (Sartomer) (4.2 g), were mixed with a dispersant, Anti-terra 203 (BYK) (0.8 g), and DB (Sigma) (12 g). The selected zeolite (6 g) was added and the mixture was stirred with a homogenizer (IKA T25) for 10 min. Then, the mixture was sonicated with a tip-sonicator (Sonics-Vibra cell, 500 W) for 10 min (1 s ON, 2 s OFF) at 40%



amplitude. Following this, the pigment, Orasol orange 272 (BASF) (0.008 g), and the photoinitiator, Irgacure TPO (BASF) (0.0125 g) were added.

#### 4.3 3D-printing and solvent exchange

The models were printed with a DLP 3D-printer (Asiga Pico 2). The printing parameters are presented in Table S2.† Once printed, the objects were washed with ethanol to remove any unpolymerized residues. Following this, the printed models were suspended in ethanol absolute (VWR) (20 mL) for 3 days to replace the DB. The ethanol was replaced with a new one every day to allow better removal of the DB.

#### 4.4 Characterization of the printed models

The structural and morphological characterization of the printed models was performed with Powder X-Ray Diffraction (PXRD) (Shimadzu XRD-6000, Cu radiation), Scanning Electron Microscopy (Carl Zeiss SUPRA 55), Accelerated Surface Area and Porosimetry System (ASAP 2020, Micromeritics, degas at 70 °C) and Differential Scanning Calorimetry (Mettler-Toledo TGA/DSC 1 star system, sample is heated from 30–800 °C in air at the rate of 20 °C min<sup>−1</sup>). Pawley fits were performed using Total Pattern Solution (TOPAS 5) to calculate unit cell parameters before and after ion exchange.

#### 4.5 Ion exchange test

The Cs and Sr uptake was tested individually by shaking the 3D-printed monoliths in 0.1 M Sr(NO<sub>3</sub>)<sub>2</sub> or CsNO<sub>3</sub> solution under batch conditions at v : m = 100 : 1 (mL : g) for 24 h at room temperature. The monoliths were rinsed with ~50 mL of water and dried at 50 °C. The Cs and Sr-exchanged monoliths were grounded and analyzed in XRD (Bruker D8, Cu radiation) and XRF (Bruker S8 Tiger WDXRF, QUANT-EXPRESS software analysis). The Cs-exchanged monoliths were examined using SEM (FEI NOVA 200 Nano SEM) equipped with EDX and Alicona Infinite Focus Microscope.

## Conflicts of interest

There are no conflicts to declare.

## Acknowledgements

This research was supported by the Singapore National Research Foundation under the CREATE program: Nano-materials for Energy and Water-Energy Nexus, by the EPSRC (EP/L014041/1, DISTINCTIVE), and by the Hebrew University Fund for PhD students. The authors would like to thank Zhou Xinran for her assistance with the SEM measurements, Dr Jackie Deans for technical assistance, Dr Colin Slater for XRF advice, Marie Chauvois and Dr Francis Clegg for TGA measurements. The XRF (Bruker S8) used in this research was obtained through Birmingham Science City: Creating and Characterising Next Generation Advanced Materials (West Midlands Centre for Advanced Materials Project 1), with support from Advantage West Midlands (AWM) and part-

funded by the European Regional Development Fund (EDRF). The Advanced Materials Facility is part of the Centre for Chemical and Materials Analysis in the School of Chemistry at the University of Birmingham.

## References

- 1 R. Pravalie and G. Bandoc, *J. Environ. Manage.*, 2018, **209**, 81–92.
- 2 T. Kobayashi, H. Nagai, M. Chino and H. Kawamura, *J. Nucl. Sci. Technol.*, 2013, **50**, 255–264.
- 3 A. Dyer, J. Hriljac, N. Evans, I. Stokes, P. Rand, S. Kellet, R. Harjula, T. Moller, Z. Maher, R. Heatlie-Branson, J. Austin, S. Williamson-Owens, M. Higgins-Bos, K. Smith, L. O'Brien, N. Smith and N. Bryan, *J. Radioanal. Nucl. Chem.*, 2018, **318**, 2473–2491.
- 4 H. Mimura and T. Kanno, *J. Nucl. Sci. Technol.*, 1985, **22**, 284–291.
- 5 W. Baek, S. Ha, S. Hong, S. Kim and Y. Kim, *Microporous Mesoporous Mater.*, 2018, **264**, 159–166.
- 6 A. Dyer and M. Zubair, *Microporous Mesoporous Mater.*, 1998, **22**, 135–150.
- 7 W. Schmidt, in *Handbook of Porous Solids*, ed. F. Schuth, K. S. W. Sing and J. Weitkamp, Wiley-VCH, 2008, DOI: 10.1002/9783527618286.ch18g.
- 8 M. W. Munthali, E. Johan, H. Aono and N. Matsue, *J. Asian Ceram. Soc.*, 2015, **3**, 245–250.
- 9 R. G. Anthony, R. G. Dosch, D. Gu and C. V. Philip, *Ind. Eng. Chem. Res.*, 1994, **33**, 2702–2705.
- 10 M. E. Huckman, I. M. Latheef and R. G. Anthony, *Sep. Sci. Technol.*, 1999, **34**, 1145–1166.
- 11 A. Clearfield, A. I. Bortun, L. N. Bortun, D. M. Poojary and S. A. Khainakov, *J. Mol. Struct.*, 1998, **470**, 207–213.
- 12 T. Möller, A. Clearfield and R. Harjula, *Microporous Mesoporous Mater.*, 2002, **54**, 187–199.
- 13 B. J. Liu, W. J. Mu, X. Xie, X. L. Li, H. Y. Wei, Z. Y. Tan, Y. Jian and S. Z. Luo, *RSC Adv.*, 2015, **5**, 15603–15611.
- 14 C. S. Fewox, A. Clearfield and A. J. Celestian, *Inorg. Chem.*, 2011, **50**, 3596–3604.
- 15 P. Sylvester, in *Encyclopedia of Separation Science*, ed. I. D. Wilson, Academic Press, Oxford, 2000, pp. 4261–4267.
- 16 M. Nyman, T. M. Nenoff and T. J. Headley, *Characterization of UOP IONSIV IE911*, 2001.
- 17 J. E. Miller, N. E. Brown, J. L. Krumhansl, D. E. Trudell, R. G. Anthony and C. V. Philip, in *Science and Technology for Disposal of Radioactive Tank Wastes*, ed. W. W. Schulz and N. J. Lombardo, Springer US, Boston, MA, 1998, pp. 269–286.
- 18 T. D. Ngo, A. Kashani, G. Imbalzano, K. T. Q. Nguyen and D. Hui, *Composites, Part B*, 2018, **143**, 172–196.
- 19 B. Panda, Y. W. D. Tay, S. C. Paul and M. J. Tan, *Materialwiss. Werkstofftech.*, 2018, **49**, 666–673.
- 20 J. L. Erkal, A. Selimovic, B. C. Gross, S. Y. Lockwood, E. L. Walton, S. McNamara, R. S. Martin and D. M. Spence, *Lab Chip*, 2014, **14**, 2023–2032.
- 21 G. Haghighashtiani, E. Habtour, S. H. Park, F. Gardea and M. C. McAlpine, *Extreme Mech. Lett.*, 2018, **21**, 1–8.

- 22 K. Gnanasekaran, T. Heijmans, S. van Bennekom, H. Woldhuis, S. Wijnia, G. de With and H. Friedrich, *Appl. Mater. Today*, 2017, **9**, 21–28.
- 23 K. Kim, W. Zhu, X. Qu, C. Aaronson, W. R. McCall, S. C. Chen and D. J. Sirbuly, *ACS Nano*, 2014, **8**, 9799–9806.
- 24 O. Halevi, J. M. R. Tan, P. S. Lee and S. Magdassi, *Adv. Sustainable Syst.*, 2018, **2**, 5.
- 25 M. J. Regufe, A. F. P. Ferreira, J. M. Loureiro, A. Rodrigues and A. M. Ribeiro, *Microporous Mesoporous Mater.*, 2019, **278**, 403–413.
- 26 S. Couck, J. Cousin-Saint-Remi, S. Van der Perre, G. V. Baron, C. Minas, P. Ruch and J. F. M. Denayer, *Microporous Mesoporous Mater.*, 2018, **255**, 185–191.
- 27 Y. H. Li, S. J. Chen, X. H. Cai, J. Q. Hong, X. Wu, Y. Z. Xu, J. J. Zou and B. H. Chen, *J. Mater. Chem. A*, 2018, **6**, 5695–5702.
- 28 H. Thakkar, S. Eastman, A. Hajari, A. A. Rownaghi, J. C. Knox and F. Rezaei, *ACS Appl. Mater. Interfaces*, 2016, **8**, 27753–27761.
- 29 X. Li, W. B. Li, F. Rezaei and A. Rownaghi, *Chem. Eng. J.*, 2018, **333**, 545–553.
- 30 S. Fu, P. He, M. Wang, M. Wang, R. Wang, J. Yuan, D. Jia and J. Cui, *J. Eur. Ceram. Soc.*, 2019, **39**, 563–573.
- 31 J. Lefevre, L. Protasova, S. Mullens and V. Meynena, *Mater. Des.*, 2017, **134**, 331–341.
- 32 R. L. Truby and J. A. Lewis, *Nature*, 2016, **540**, 371–378.
- 33 I. A. E. Agency, *Application of Ion Exchange Processes for Treatment of Radioactive Waste and Management of Spent Ion Exchangers*, International Atomic Energy Agency, Vienna, 2002.
- 34 Z. Klika, L. Kraus and D. Vopalka, *Langmuir*, 2007, **23**, 1227–1233.
- 35 H. J. Liu, S. B. Xie, L. S. Xia, Q. Tang, X. Kang and F. Huang, *Environ. Earth Sci.*, 2016, **75**, 1–7.
- 36 I. Plecas, S. Dimovic and I. Smiciklas, *Prog. Nucl. Energy*, 2006, **48**, 495–503.
- 37 X. Kuang, K. J. Chen, C. K. Dunn, J. T. Wu, V. C. F. Li and H. J. Qi, *ACS Appl. Mater. Interfaces*, 2018, **10**, 7381–7388.
- 38 D. Han, Z. C. Lu, S. A. Chester and H. Lee, *Sci. Rep.*, 2018, **8**, 10.
- 39 Y. Y. Li, H. D. Tolley and M. L. Lee, *J. Chromatogr. A*, 2010, **1217**, 4934–4945.
- 40 Y. Y. Li, H. D. Tolley and M. L. Lee, *J. Chromatogr. A*, 2011, **1218**, 1399–1408.
- 41 C. Viklund, F. Svec, J. M. J. Frechet and K. Irgum, *Chem. Mater.*, 1996, **8**, 744–750.
- 42 B. P. Santora, M. R. Gagne, K. G. Moloy and N. S. Radu, *Macromolecules*, 2001, **34**, 658–661.
- 43 M. Bourgonne, J.-L. Guth and R. Wey, *US Pat.*, 4 503 024, 1985.
- 44 *Verified Syntheses of Zeolitic Materials*, ed. H. Robson and K. P. Lillerud, Elsevier Science, Amsterdam, 2001, pp. 123–125, DOI: 10.1016/B978-044450703-7/50132-0.



## Supporting Information

### Nuclear Wastewater Decontamination by 3D-Printed Hierarchical Zeolite Monoliths

*Oded Halevi, Tzu-Yu Chen, Pooi See Lee\*, Shlomo Magdassi\*, Joseph A. Hriljac\**

O. H. and T.-Y. C. contributed equally to this work.

Dr. J. A. Hriljac, Dr. T.-Y. Chen

School of Chemistry, University of Birmingham, Edgbaston, Birmingham, B15 2TT, UK.

Dr. J. A. Hriljac

Diamond Light Source Ltd, Harwell Science and Innovation Campus, Didcot, OX11 0DE, UK.

Dr. T.-Y. Chen

Materials and Engineering Research Institute, Faculty of Science, Technology and Arts, Sheffield Hallam University, City Campus, Howard Street, Sheffield, S1 1WB, UK

Prof. S. Magdassi, Prof. P. S. Lee, O. Halevi

CREATE NTU-HUJ Programme, Enterprise Wing, 138602, Singapore.

Prof. S. Magdassi, O. Halevi

Casali Center for Applied Chemistry, Institute of Chemistry, The Hebrew University of Jerusalem, Jerusalem, 91904, Israel.

Prof. P. S. Lee, O. Halevi

School of Materials Science and Engineering, Nanyang Technological University, 639798, Singapore.

E-mail: joseph.hriljac@diamond.ac.uk; magdassi@mail.huji.ac.il; pslee@ntu.edu.sg

1. Table S1. XRF results of Cs and Sr adsorption on 3D printed polymer metrics
2. Table S2. Printing parameters
3. Figure S1. Pawley fits of 3D-CHA and 3D-zeolite 4A before and after Cs and Sr exchanges

**Table S1.** XRF results of Cs and Sr adsorption on 3D printed polymer metrics

	<b>control sample 1</b>		<b>control sample 2</b>		<b>control sample 3</b>	
	Formula	wt%	Formula	wt%	Formula	wt%
<b>Cs adsorption</b>	Ce	0.11%	P	0.09%	Ce	0.11%
	P	0.10%	Cr	0.03%	P	0.06%
	Ca	0.06%	Fe	0.02%	Fe	0.02%
	Cl	0.06%			Si	0.02%
	Zr	0.04%			S	0.01%
	Fe	0.04%			Mg	0.01%
	S	0.03%				
	Mg	0.02%				
	V	0.02%				
<b>Sr adsorption</b>	Formula	wt%	Formula	wt%	Formula	wt%
	P	0.11%	P	0.03%	P	0.11%
	Al	0.09%	Fe	0.03%	Na	0.06%
	Ca	0.05%	Mo	0.02%	Fe	0.04%
	Sr	0.05%	Sr	0.02%	Cl	0.03%
	Cr	0.04%	Mg	0.01%	Ca	0.03%
	Cu	0.02%			Si	0.03%
	Ti	0.02%				

**Table S2.** Printing parameters

<b>Parameter</b>	<b>Value</b>
Light Intensity	39.158 [mW/cm <sup>2</sup> ]
Slice thickness	0.050 [mm]
Burn-In Exposure Time	45.000 [s]
Exposure Time	12.000 [s]
Separation Velocity	1.000 [mm/s]
Separation Distance	5.000 [mm]
Approach Velocity	2.000 [mm/s]
Slides Per Layer	1.000
Slide Velocity	10.000 [mm/s]
Burn-In Wait Time (After Exposure)	5.000 [s]
Burn-In Wait Time (After Separation)	5.000 [s]
Burn-In Wait Time (After Approach)	0.000 [s]
Burn-In Wait Time (After Slide)	0.000 [s]
Normal Wait Time (After Exposure)	5.000 [s]
Normal Wait Time (After Separation)	3.000 [s]
Normal Wait Time (After Approach)	0.000 [s]
Normal Wait Time (After Slide)	0.000 [s]

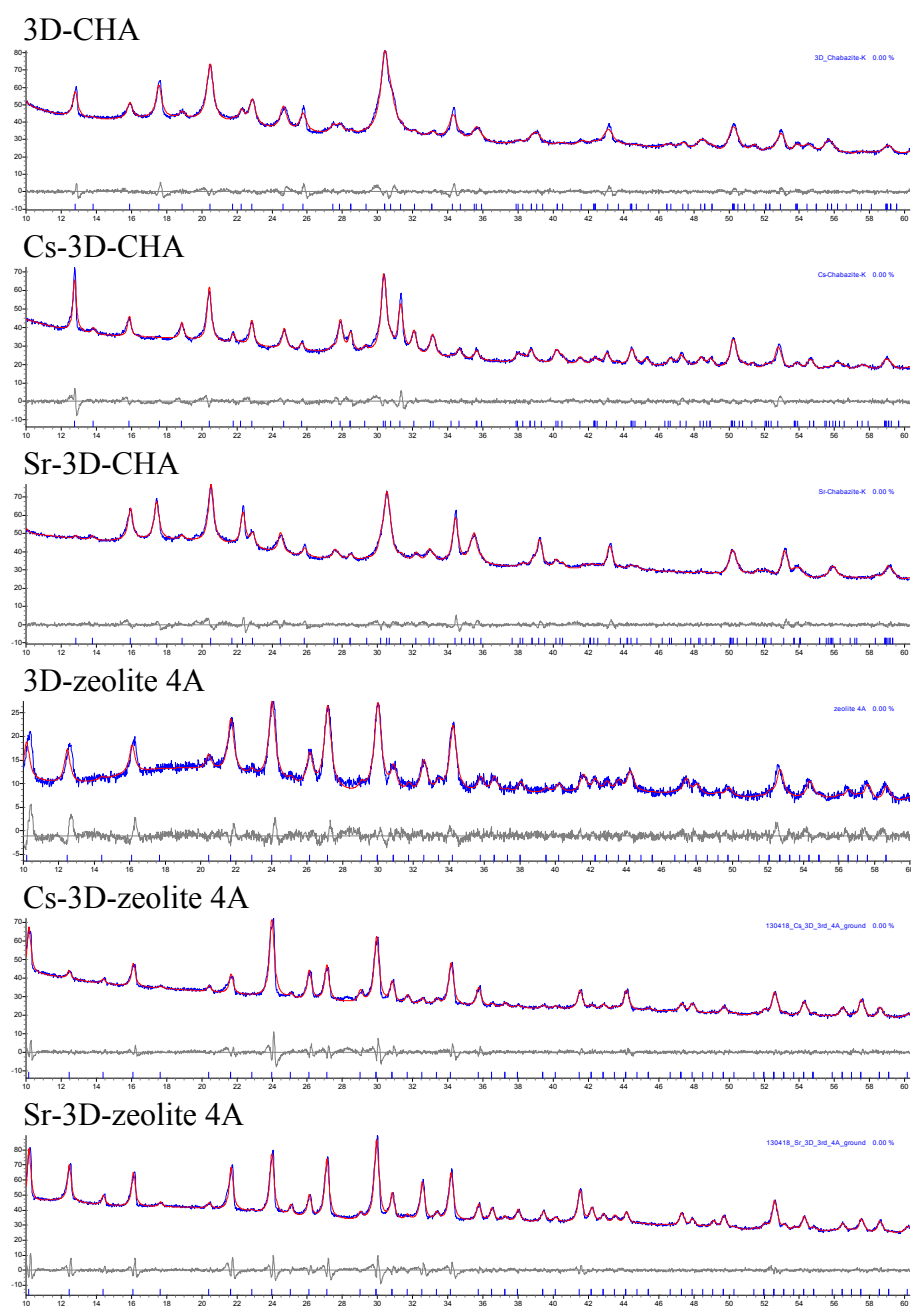


**Figure S1.** Pawley fits of 3D-CHA and 3D-zeolite 4A before and after Cs and Sr exchanges.

### **2.3. Chapter 3: Synthesis Through 3D Printing: Formation of 3D Coordination Polymers**

Halevi O., Chen J., Thangavel G., Morris A.S., Ben-Uliel T., Tichler Y., Lee P.S. and Magdassi S.  
Submitted.





# Synthesis through 3D printing: Formation of 3D Coordination Polymers

Oded Halevi<sup>1,2,3</sup>, Jingwei Chen<sup>2,3</sup>, Gurunathan Thangavel,<sup>2</sup> Samuel Alexander Morris,<sup>2</sup> Tal Ben Uliel<sup>4</sup>, Yaakov Tischler<sup>4</sup>, Pooi See Lee<sup>2,3\*</sup>, Shlomo Magdassi<sup>1,3\*</sup>

<sup>1</sup>Casali Center for Applied Chemistry, Institute of Chemistry, The Hebrew University of Jerusalem, Jerusalem, 91904, Israel. <sup>2</sup>School of Materials Science and Engineering, Nanyang Technological University, 639798, Singapore. <sup>3</sup>Singapore-HUJ Alliance for Research and Enterprise (SHARE), Nanomaterials for Energy and Energy-Water Nexus (NEW), Campus for Research Excellence and Technological Enterprise (CREATE), Singapore 138602. <sup>4</sup>Department of Chemistry, Bar-Ilan University, Ramat-Gan, 5290002, Israel.

## Abstract

Metal organic frameworks (MOFs) and coordination polymers (CPs), gain a lot of interest during recent years due to their unique properties and huge potential for applications. Combining these materials within 3D structures would provide many advantages towards utilization in various fields, such as energy, catalysis and sensing. So far, 3D structures were printed only by dispersing pre-synthesized particles of MOFs and CPs within a polymerizable carrier, while the printing was used only to convert the liquid carrier into a solid. This resulted in the active material dispersed within an inert 3D polymeric body. Here we present a new concept for obtaining 3D objects solely composed of the CP material, by starting from soluble coordination metal complexes as the monomeric building blocks, and utilizing the 3D printer both as a tool to synthesize a coordination polymer, and to fabricate 3D object. To demonstrate the new approach, nickel tetra-acrylamide monomeric complex, was simultaneously converted into a coordination polymer and printed to a pre-designed 3D-shape, composed solely of the coordination polymer, without any additional materials. We expect that this work will open new directions in additive manufacturing and utilization of coordination polymers.

## Introduction

Coordination polymers (CPs) belong to a highly interesting family of materials, which are 1D, 2D and 3D macro molecules, comprised of metal ions that are linked by ligands, usually organic molecules (Figure 1a). CPs have become popular in the past twenty years, since the rising of the sub-group of porous CPs, known as metal-organic frameworks (MOFs),<sup>1</sup> among other groups of promising porous functional materials.<sup>2, 3</sup> The interest in CPs started in the early 1950's,<sup>4</sup> and this group of extended inorganic-organic assemblies includes many additional porous and non-porous compounds, which have interesting chemical properties and applications in a wide variety of fields. Most of the reports focus on the molecular design, synthetic chemistry and their applications in heterogeneous catalysis, gas storage and molecular separation. For example, Soo Seo et al. reported the synthesis of a porous coordination polymer for the catalysis of an enantioselective transesterification reaction;<sup>5</sup> Du et al. synthesized a silver coordination polymer for highly selective sensing of Cd<sup>2+</sup>;<sup>6</sup> and Wang et al. explored coordination polymer particles with antibacterial and anticancer activity.<sup>7</sup>

With the advent of additive manufacturing that effectuates the emergence and quick adoption of three-dimensional (3D) printing, bottom-up fabrication of functional 3D-objects have been realized rapidly. For example, functional reaction-ware, shape-customized adsorbing structures, 3D catalysts and batteries are a few examples that can be achieved through 3D printing with the layer-by-layer deposition of materials, according to a predesigned computer 3D model.<sup>8</sup> 3D printing enables

formation of customized and complex structures with minimum material waste and high precision.<sup>9</sup> Initially, the most commonly printed materials were organic polymers, more recently, the potential of 3D-printing has pored over to the discovery of unique materials properties and the development of new fabrication processes inclusive of metals,<sup>10</sup> ceramics and hydrogels.<sup>11, 12</sup> The properties of the resulting 3D objects are dependent on the printing technology; for example, light initiated printing, such as digital light processing printers (DLP) (Figure S1), is based on localized UV-polymerization of liquid formulations, layer over layer, to form solid 3D-structures. Typical inks for this technology are composed of photoinitiators and monomers, and in some cases dispersed or dissolved materials. An interesting approach was recently reported by Greer et al. using two-photon lithography printing of monomers with nickel-containing photoresist, resulting in a structure containing more than 90 wt% Ni-containing architecture after pyrolysis of the organic materials.<sup>13</sup>

In the past two years, there were several reports on functional 3D-printed structures that contain coordination polymers. We previously reported on the 3D-printing of Cu-BTC MOF for the adsorption of organic dyes from solutions,<sup>14</sup> and in collaboration with Amo-Ochoa and Zamora, on the 3D-printing of a Cu<sup>2+</sup> coordination polymer for the colorimetric sensing of humidity and water.<sup>15</sup> Other research groups also printed MOFs for various applications, for example, 3D-printed a cobalt-based MOF embedded within an organic binder by Lyu et al. for energy storage applications.<sup>16</sup> 3D-printed ZIF-7 embedded within organic monoliths for ethane/ethylene separation process by Thakkar et al.,<sup>17</sup> and 3D-printing MOF embedded in organic-inorganic binder for removal of CO<sub>2</sub> from air.<sup>18</sup> More examples on 3D-printed MOFs were explored by Lawson et al. and Sultan et al.<sup>19, 20</sup>

In these prior works, the coordination polymers were synthesized prior to the printing, mostly in the form of particles, which were later dispersed within matrix forming material, since the CP particles could not form a stand-alone 3D object. Therefore, so far, the resulting printed objects are composed of CPs embedded within organic or inorganic binders. A direct print-and-form route to prepare free standing coordination polymer object with 3D architecture has not been realized.

Herein, we present a new approach, in which we form 3D objects composed of a coordination polymer, while the printing process causes the synthesis of the coordination polymer, resulting in a free standing 3D object composed only of a coordination polymer.

Our approach differs from the traditional pathway to the synthesis of CPs in which metal ions were reacted with bridging ligands, which have more than one metal-binding site (Figure 1a).<sup>21</sup> Another possibility, although challenging and not common, is to bind non-bridging ligands to the metal ions to form inorganic complexes, and then connect these ligands to one another (Figure 1b). Such **metal-containing-monomers** (MCMs)<sup>22, 23 24, 25, 26</sup> have both polymerizable functional groups and electron donating groups, such as acrylamide and acrylic acid (Figure 1c). In these attempts, the polymerization was initiated mostly by heating.

By proper selection of ligands that can polymerize upon exposure to ultra-violet (UV) light, we hypothesize that rationally designed and formulated MCMs can be utilized as 3D inks that can form free-standing objects without any additional binders or monomers, by light initiated printing processes. Therefore, the printing can be utilized both as a tool to synthesize the coordination polymer, and to directly obtain 3D structures composed predominantly of the coordination polymer, that can be tailored according to the required application. To the best of our knowledge, this new approach has yet to be reported till date. To demonstrate the new approach, we have synthesized MCM with a Ni<sup>2+</sup> metal center and acrylamide ligands, and formulated it as a photo-polymerizable ink, without any additional monomers. The ink composition was 3D-printed by a DLP printer, resulting in a stand-alone complex structure of an amorphous coordination polymer.

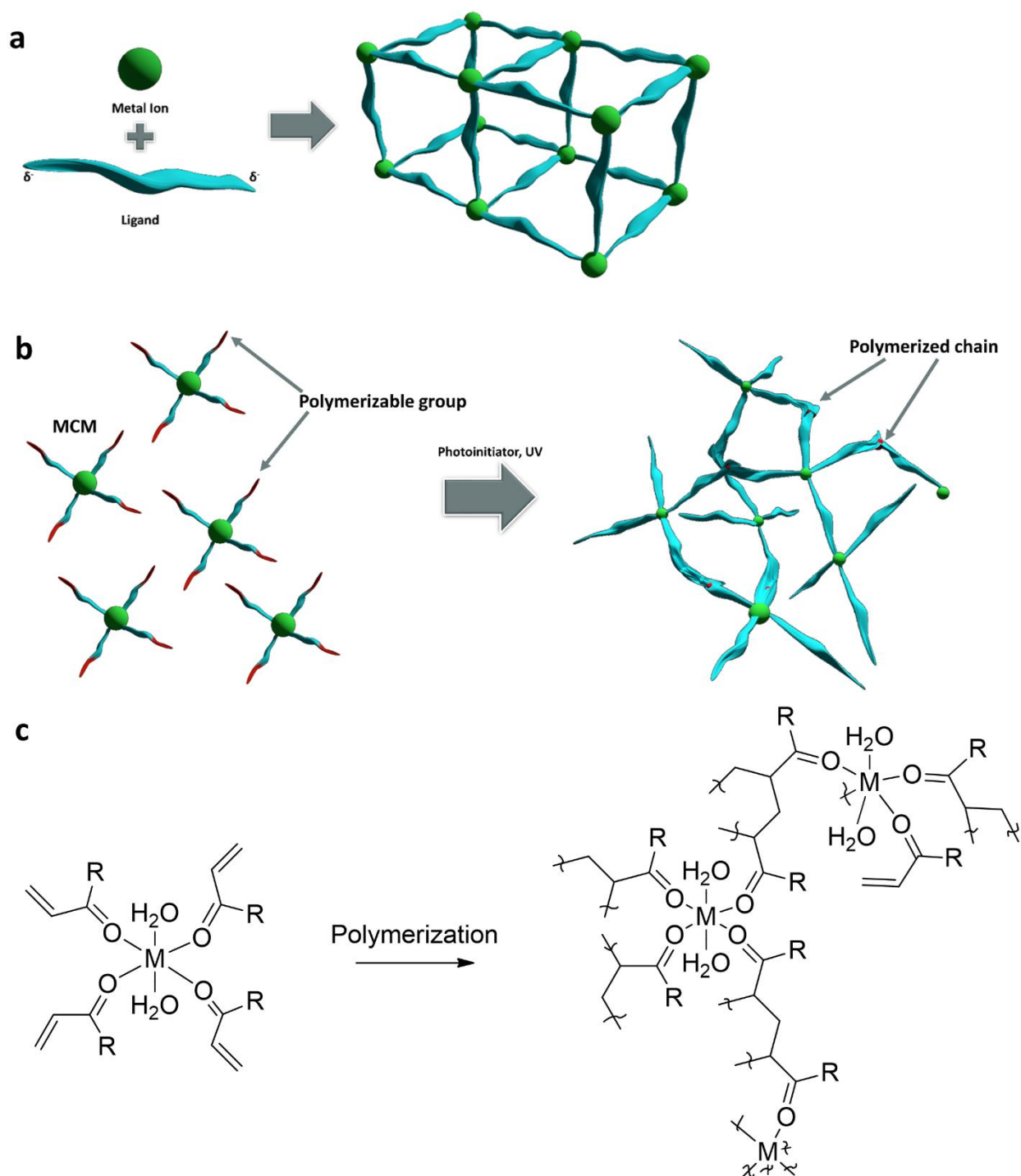


**Figure 1.** a) CP formation by reacting metal ions with bridging ligands. b) CP formation by polymerization of MCMs. c) The hypothesized polymerization reaction of the MCM with polymerizable acryl ligands.

## Results and Discussion

In this work, nickel(II) was selected as the metal for the MCM, since it demonstrates rich chemistry and is being utilized for various applications, mostly for catalysis. For example: Cui et al. synthesized a  $\text{Ni}^{2+}$  CP and demonstrated its photocatalytic activity in degradation of water pollutants;<sup>27</sup> Ghorbani-Choghamarani et al. immobilized  $\text{Ni}^{2+}$  complexes on boehmite nanoparticles for the heterogeneous catalysis of sulfides oxidation to sulfoxides, and oxidative coupling of thiols into disulfides;<sup>28</sup> and Malgas et al. synthesized dendritic  $\text{Ni}^{2+}$  catalysts for ethylene oligomerization.<sup>29</sup> Therefore, we have first synthesized the photo-polymerizable Ni containing monomer, followed by its conversion into a coordination polymer by 3D-printing process.

**MCM synthesis and characterization.** For a proof of concept for the new approach, we synthesized a MCM based on nickel and acrylamide ligands,  $[\text{Ni}(\text{AAm})_4(\text{H}_2\text{O})_2](\text{NO}_3)_2$  (**Ni Complex**).<sup>30</sup> The MCM was obtained as a wet powder, which was then recrystallized into a single crystal from ethanol, and its structure was determined for the first time (Figure 2a, 2b and Table S1). As shown, the complex has interesting features: The octahedral complex comprises four acrylamide ligands bonded to the  $\text{Ni}^{2+}$  center via the carbonyl oxygen, and two water molecules in axial positions. The presence of the coordinative water molecules has high significance for future utilizations of the MCM polymerization product, as it may provide two available positions on the polymeric  $\text{Ni}^{2+}$  ion, and its potential binding to other electron-donating molecules. Powder X-ray diffraction measurement (PXRD) (Figure 2b) confirmed that the crystal structure of the wet powder was identical to the single crystal. Further investigation of the structure by Fourier Transform Infra-Red (FTIR) spectroscopy (Figure 2c) shows a spectrum similar to one of the free acrylamide. Following complexation, an expected redshift and splitting of the bands at  $1670\text{ cm}^{-1}$  and  $1613\text{ cm}^{-1}$  is observed; this corresponds well with the previously reported FTIR spectra of other acrylamide metal complexes.<sup>22</sup> The characteristic peak of the non-coordinative nitrate ion, around  $1400\text{ cm}^{-1}$ , can be identified as a shoulder at  $1443\text{ cm}^{-1}$  in the Ni complex spectrum.

**3D-Printing of the MCM.** 3D objects of the coordination polymer (**polyNiComplex**) were printed successfully by the DLP printer (Figure 3a), while using the MCM as the single monomer in the solution, without any additional monomers. Since the synthesized MCM has four acrylamide ligands, it could function as a built-in cross-linker. The MCM was dissolved in absolute ethanol at a weight ratio of 1:2 respectively, and a photo-initiator, diphenyl(2,4,6-trimethylbenzoyl)phosphine oxide (TPO) was added at a low concentration (2 %wt). It should be noted that the printed object remained covered by the ethanol solution throughout the whole printing process, thus avoiding problems arising from the hygroscopic nature of the CP. Once the printing was complete, the 3D-CP object was exposed to UV light for additional five minutes, in order to react any unpolymerized monomers on the surface, followed by a thorough washing with ethanol and drying under vacuum. An interesting feature of the printed CP, which was revealed by scanning electron microscopy (SEM), is its macroporous structure (Figure 3b). As shown, the whole 3D object is composed of connected spherical particles, which as will be proven in the following section, are composed of the coordination polymer. This is of high importance in view of future applications in which surface area is essential, such as in diagnostics, catalysis and separation processes. The measured surface area revealed that the printed material has a surface area of  $53.32 \pm 23.00\text{ m}^2/\text{g}$ . The measured isotherm (Figure S2), combined with the calculated pores size of  $35.90 \pm 24.80\text{ \AA}$ , suggests a mesoporous structure. Currently, further investigation of the porosity and its tuning, as well as the influence of the macro structure of the 3D-printed objects on the total accessible surface area of the CP is underway, and will be the focus of a future report.

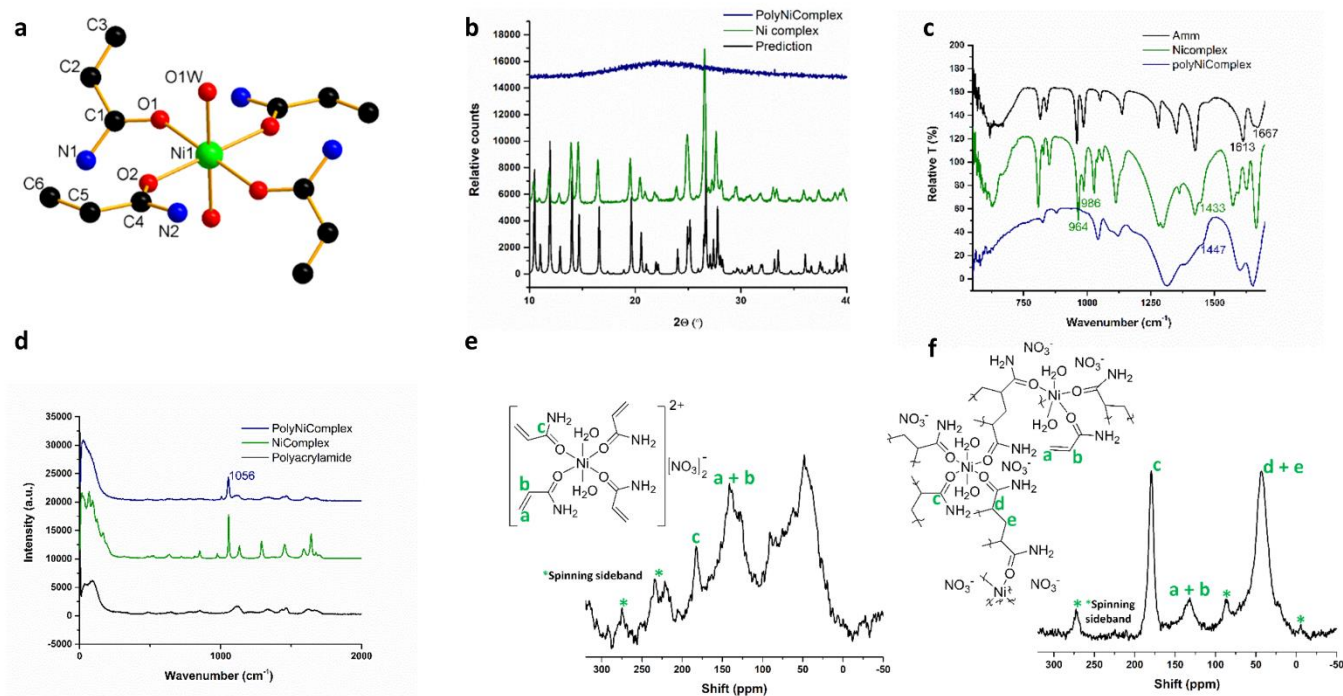


**Figure 2.** a) Crystal structure of the  $[\text{Ni}(\text{AAm})_4(\text{H}_2\text{O})_2]^{2+}$  complex, hydrogen atoms and the nitrate anions were removed for clarity. b) PXRD prediction, based on the single crystal structure, and the measured diffractograms for Ni Complex and the polyNiComplex. c) FTIR spectra of the free acrylamide, Ni complex, and polyNiComplex. d) Raman spectra of the polyNiComplex, Ni Complex, and polyacrylamide. e) Solid-State  $^{13}\text{C}$  NMR of Ni Complex. f) Solid-State  $^{13}\text{C}$  NMR of polyNiComplex.

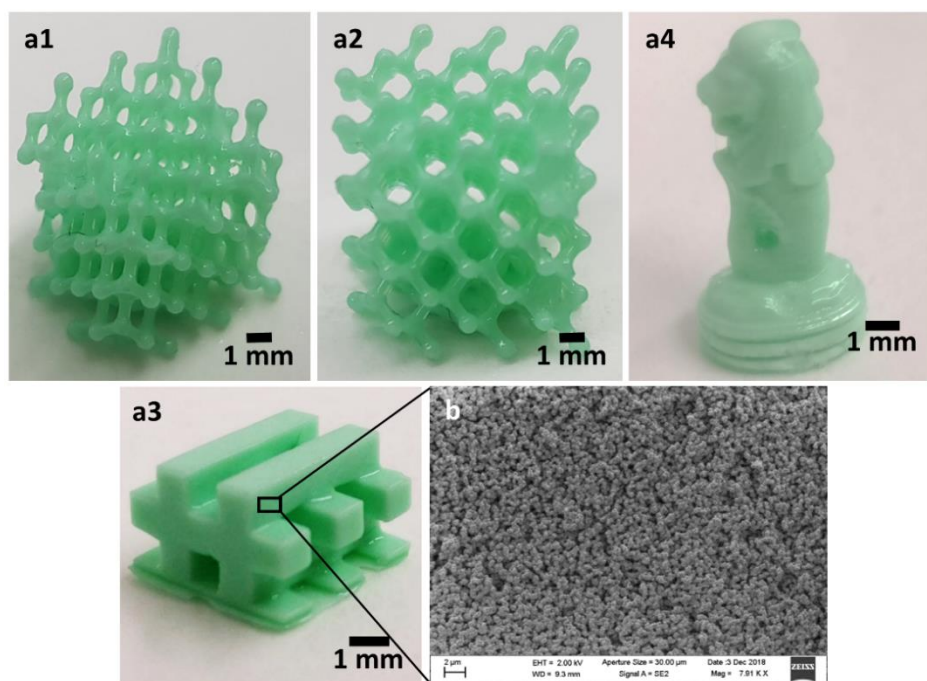


**Figure 3.** a) Various 3D-printed structures of polyNiComplex. b) SEM of the printed polyNiComplex cross-section.

**Characterization of the 3D-printed CP.** A major challenge following the 3D-printing process, was to identify whether the Ni–O bond of the nickel-acrylamide remained intact during the radical polymerization reaction; and whether the printed object was indeed a coordination polymer. PXRD of the printed polymer was performed and it was found that it is non-crystalline. FTIR measurements (Figure 2c) indicated that the polymerization reaction indeed occurred, as the peaks for C=CH and C=CH<sub>2</sub> at 986 cm<sup>-1</sup> and 964 cm<sup>-1</sup> disappeared in the polymer spectrum.<sup>22</sup> However, the Ni–O bond could not be identified, as it was predicted to be around 400-500 cm<sup>-1</sup>.<sup>31, 32, 33</sup> As in the Ni complex salt, the nitrate ion was also present in the polymerized product, as indicated by the shoulder at 1447 cm<sup>-1</sup>. Furthermore, Raman spectroscopy (Figure 2d) revealed the presence of the nitrate ions in the printed polymer, as its typical Raman shift appeared at 1056 cm<sup>-1</sup>. Nuclear magnetic resonance (NMR) was considered in order to extract more information on the nickel environment. <sup>61</sup>Ni NMR was not practical due to the paramagnetism of Ni<sup>2+</sup>, however solid <sup>13</sup>C NMR revealed more information (Figure 2e,f). For the monomer NMR, the peak at 56.28-34.93 ppm, indicates saturated CH<sub>2</sub> and CH carbons, revealing that during the drying process, following the synthesis and washing steps, partial polymerization took place. For this reason, the monomer was used without drying, immediately after the synthesis and washings. For the polymer, the NMR revealed that the C=C bond decayed and a C–C bond was formed instead. So far, the organic part of the hypothesized CP was well characterized, however there was no direct indication regarding the Ni<sup>2+</sup> species and its immediate chemical environment in the polymer.

Focusing on the nickel, there were three questions to be addressed: First, was the distribution of the nickel in the polymer uniform, or was there a phase-separation between the Ni<sup>2+</sup> and the polyacrylamide? Second, has there been any loss of nickel ions during the printing or the washings? Third, was the nickel still bonded to the carbonyl oxygen of the acrylamide? The first question was addressed by Energy-dispersive X-ray spectroscopy measurements (EDX), which showed a uniform distribution of the Nickel throughout the whole printed structure (Figure S3); thus it was concluded that no phase-separation occurred. For the second question, inductively coupled plasma optical emission spectrometry (ICP-OES) measurements were conducted. The results in Table 1 show that the amount of nickel in the object after the washing step remained the same as that at the beginning of the process, within the error range. To verify the existence of Ni–O bonds, we compared the binding energies of the Ni<sup>2+</sup> before and after polymerization, by X-ray photoelectron spectroscopy (XPS) (Figure S3). The binding energies of MCM Ni 2p<sub>1/2</sub> and Ni 2p<sub>3/2</sub> are located at 873.8 eV and 856.3 eV respectively, indicative of the presence of Ni<sup>2+</sup> (typical Ni–O=C binding energy)<sup>34</sup> in the MCM (Table 1). After the printing/polymerization process, there were no shifts of the binding energies of Ni 2p<sub>1/2</sub> and Ni 2p<sub>3/2</sub> in polyNiComplex, indicating no change in chemical environment of Ni<sup>2+</sup> before and after polymerization. These results, combined with <sup>13</sup>C NMR and Raman spectroscopy, indicated that the Ni<sup>2+</sup> ions remained bonded to the carbonyl oxygen, forming a positively charged coordination polymer stabilized with nitrate ions. Thus, it could be concluded that a coordination polymer was indeed successfully synthesized by 3D-printing.

**Table 1. Nickel weight percentage and binding energies in the Ni Complex and polyNiComplex, as measured by ICP-OES and XPS, respectively.**

Sample	Ni wt% by ICP-OES	2P 3/2 [eV]	2P 1/2 [eV]
Ni Complex	6.4 ± 1.6	856.3	873.8
polyNiComplex	7.4 ± 0.3	856.3	873.8

In summary, this paper presents an unprecedented synthetic print-and-form strategy through the utilization of light-based 3D-printing as a synthesis tool for coordination polymers. This work has two interesting aspects; first, synthesis-wise, for the first time a transition-metal complex was used as a monomer for 3D-printing without additional co-monomers, enabling the synthesis of pure porous CP by printing. The second important aspect of this work is the ability to form complex structures of stand-alone CPs, thus opening the pathways for their utilization for various applications that require complex architectures, such as reactive flow reactors, separation columns, and reaction-ware with built-in catalysts. Although the current work focused on Ni-acrylamide complexes, we expect that the variety of metal ions and polymerizable ligands will enable the synthesis through printing of many other amorphous or crystalline CPs, with tailored functionality that takes advantage of free standing complex 3D objects.

## Methods

**Synthesis of [Ni(AAm)<sub>4</sub>(H<sub>2</sub>O)<sub>2</sub>](NO<sub>3</sub>)<sub>2</sub> (Ni Complex).** Ni(NO<sub>3</sub>)<sub>2</sub>·6H<sub>2</sub>O (Sigma)(2.5 g) and Acrylamide (AAm) (Sigma)(3.0 g) were mixed and grinded together with a mortar and pestle for several minutes. As the reaction progressed, water was released and the reaction mixture turned from dark to light green. Following this, the product was washed three times with chloroform (VWR) and three times with diethyl ether (Sigma). Single crystals were obtained by recrystallization from ethanol. Solid-State <sup>13</sup>C NMR [Ni(AAm)<sub>4</sub>(H<sub>2</sub>O)<sub>2</sub>](NO<sub>3</sub>)<sub>2</sub>: (600 MHz, δ) 56.28-34.93 (-CH<sub>2</sub>, -CH), 145.93-126.61 (-CH=CH<sub>2</sub>), 186.60-178.51 (-C=O), \*: spinning sideband.

**3D-printing of polyNiComplex.** Ni complex was dissolved in ethanol absolute (VWR), in a 1:2 weight ratio, respectively. The photoinitiator, Irgacure TPO (BASF)(2 wt%), was added to the solution. The 3D-structures were printed with the DLP 3D-printer (Asiga Pico 2). The printing parameters are shown in Table S2. Following the printing, the structures were exposed to UV-light for 5 mins, washed with ethanol absolute three times and placed under vacuum at room temperature overnight. Solid-State <sup>13</sup>C NMR Poly[Ni(acrylamide)<sub>4</sub>(H<sub>2</sub>O)<sub>2</sub>](NO<sub>3</sub>)<sub>2</sub>: (600 MHz, δ) 56.88-32.67 (-CH<sub>2</sub>, -CH), 140.75-126.09 (-CH=CH<sub>2</sub>, -CH<sub>2</sub>-CH<sub>2</sub>-), 188.32-173.94 (-C=O), \*: spinning sideband.

**Characterization methods.** The characterization of Ni Complex and the polyNiComplex was done with Powder X-Ray Diffraction (Shimadzu, XRD-6000), Single-crystal X-Ray Diffraction (Bruker, SMART APEX II) Fourier Transform Infra-Red (PerkinElmer, Frontier), Raman X-Ray Photoelectronic Spectroscopy (Ondax, THz-Raman), Surface area measurements (Micromeritics, ASAP-2020) - the surface area was calculated according to the Brunauer-Emmett-Teller (BET) model, prior to the surface area measurement the 3D-printed structures were gently grinded with a mortar and pestle, and degassed for 12 h at 50 °C. Inductively Coupled Plasma Optical Emission Spectrometry (Perkin Elmer, Optima 8300), Scanning Electron Microscopy (Carl Zeiss, SUPRA 55), Energy-Dispersive X-Ray Spectroscopy (JEOL, FESEM 7600F), X-Ray Photoelectron Spectroscopy (Kratos Analytical, Axis



Ultra), and Solid-State  $^{13}\text{C}$  NMR (Bruker, Avance III HD 600 MHz (14.1 T) wide-bore MAS Solid-state NMR spectrometer).

### **Acknowledgements**

This research was supported by the grants from the National Research Foundation, Prime Minister's Office, Singapore under its Campus of Research Excellence and Technological Enterprise (CREATE) Programme, Nanomaterials for Energy and Water-Energy Nexus, and the EPSRC (EP/L014041/1, DISTINCTIVE), and by the Hebrew university fund for PhD students. The authors would like to thank the Facility for Analysis Characterization and Simulation (FACTS) in MSE NTU, for assisting with the XRD measurements and analysis. We thank Prof. Felix Zamora and Prof. Pilar Amo Ochoa for the fruitful discussions.

## References

1. Furukawa H, Cordova K.E., O'Keeffe M., Yaghi O.M. The Chemistry and applications of metal-organic frameworks. *Science* **341**, 974 (2013).
2. Yuan S., Li X., Zhu J., Zhang G., Van Puyvelde P., Van der Bruggen B. Covalent organic frameworks for membrane separation. *Chem. Soc. Rev.* **48**, 2665-2681 (2019).
3. Li Y., Li L., Yu J.H. Applications of zeolites in sustainable chemistry. *Chem.* **3**, 928-949 (2017).
4. Biradha K., Ramana A., Vittal J.J. Coordination polymers versus metal-organic frameworks. *Cryst. Growth Des.* **9**, 2969-2970 (2009).
5. Seo J.S., *et al.* A homochiral metal-organic porous material for enantioselective separation and catalysis. *Nature* **404**, 982-986 (2000).
6. Du P.Y., Gu W., Gao S., Liu X. A bimodal 2D silver coordination polymer: Turn-on sensing of Cd-II and sensitization of lanthanide ions. *Inorg. Chem. Commun.* **60**, 47-50 (2015).
7. Wang K.B., Ma X.Y., Shao D.L., Geng Z.R., Zhang Z.Y., Wang Z.L. Coordination-induced assembly of coordination polymer submicrospheres: Promising antibacterial and in vitro anticancer activities. *Crys. Growth Des.* **12**, 3786-3791 (2012).
8. Horvath J. *Mastering 3D Printing*. Apress (2014).
9. Ngo T.D., Kashani A., Imbalzano G., Nguyen K.T.Q., Hui D. Additive manufacturing (3D printing): A review of materials, methods, applications and challenges. *Compos. Pt. B-Eng.* **143**, 172-196 (2018).
10. Martin J.H., Yahata B.D., Hundley J.M., Mayer J.A., Schaedler T.A., Pollock T.M. 3D printing of high-strength aluminium alloys. *Nature* **549**, 365 (2017).
11. Minas C., Carnelli D., Tervoort E., Studart A.R. 3D printing of emulsions and foams into hierarchical porous ceramics. *Adv. Mater.* **28**, 9993-9999 (2016).
12. Li H.J., Tan C., Li L. Review of 3D printable hydrogels and constructs. *Mater. Des.* **159**, 20-38 (2018).
13. Vyatskikh A., Delalande S., Kudo A., Zhang X., Portela C.M., Greer J.R. Additive manufacturing of 3D nano-architected metals. *Nat. Commun.* **9**, 593 (2018).

14. Halevi O., Tan J.M.R., Lee P.S., Magdassi S. Hydrolytically stable MOF in 3D-printed structures. *Adv. Sustain. Syst.* **2**, 1700150 (2018).
15. Maldonado N., *et al.* 3D printing of a thermo- and solvatochromic composite material based on a Cu(II)–thymine coordination polymer with moisture sensing capabilities. *Adv. Funct. Mater.* **29**, 1808424 (2019).
16. Lyu Z.Y., *et al.* 3D-printed MOF-derived hierarchically porous frameworks for practical high-energy density Li-O-2 batteries. *Adv. Funct. Mater.* **29**, 1806658 (2019).
17. Thakkar H., *et al.* Adsorption of ethane and ethylene over 3D-printed ethane-selective monoliths. *ACS Sustain. Chem. Eng.* **6**, 15228-15237 (2018).
18. Thakkar H., Eastman S., Al-Naddaf Q., Rownaghi A.A., Rezaei F. 3D-printed metal-organic framework monoliths for gas adsorption processes. *Acs Appl. Mater. Interfaces* **9**, 35908-35916 (2017).
19. Lawson S., *et al.* UTSA-16 growth within 3D-printed Co-kaolin monoliths with high selectivity for CO<sub>2</sub>/CH<sub>4</sub>, CO<sub>2</sub>/N<sub>2</sub>, and CO<sub>2</sub>/H<sub>2</sub> Separation. *Acs Appl. Mater. Interfaces* **10**, 19076-19086 (2018).
20. Sultan S., Abdelhamid H.N., Zou X.D., Mathew A.P. CelloMOF: Nanocellulose enabled 3D printing of metal-organic frameworks. *Adv. Funct. Mater.* **29**, 1805372 (2019).
21. Benmansour S., Gomez-Garcia C.J. A heterobimetallic anionic 3,6-connected 2D coordination polymer based on nitrilate as ligand. *Polymers* **8**, 89 (2016).
22. Girma K.B., Lorenz V., Blaurock S., Edelmann F.T. Coordination chemistry of acrylamide 2. Classical complexes of acrylamide with manganese(II), iron(II) and nickel(II) chlorides: Syntheses and crystal structures. *Z. Anorg. Allg. Chem.* **631**, 2763-2769 (2005).
23. Girma K.B., Lorenz V., Blaurock S., Edelmann F.T. Coordination chemistry of acrylamide 4. Crystal structures and IR spectroscopic properties of acrylamide complexes with Co-II, Ni-II, and Zn-II nitrates. *Z. Anorg. Allg. Chem.* **631**, 1843-1848 (2005).
24. Uflyand I.E., Ilchenko I.A., Starikov A.G., Sheinker V.N., Pomogailo A.D. Preparation and reactivity of metal-containing monomers .13. Complexes of transition-metals with methacroyacetophenone *Bull. Acad. Sci. USSR. Div. Chem. Sci.* **39**, 388-391 (1990).

25. Savostyanov V.S., *et al.* Preparation and reactivity of metal-containing monomers .14. Composition and structure of acrylamide complexes of transition-metals. *Bull. Acad. Sci. USSR. Div. Chem. Sci.* **39**, 674-679 (1990).
26. Savostyanov V.S., Pomogailo A.D., Selenova B.S., Kritskaya D.A., Ponomarev A.N. Preparation and reactivity of metal-containing monomers .15. Frontal polymerization of acrylamide complexes of transition-metals. *Bull. Acad. Sci. USSR. Div. Chem. Sci.* **39**, 680-684 (1990).
27. Cui J.W., Hou S.X., Li Y.H., Cui G.H. A multifunctional Ni(II) coordination polymer: synthesis, crystal structure and applications as a luminescent sensor, electrochemical probe, and photocatalyst. *Dalton Trans.* **46**, 16911-16924 (2017).
28. Ghorbani-Choghamarani A., Tahmasbi B., Arghand F., Faryadi S. Nickel Schiff-base complexes immobilized on boehmite nanoparticles and their application in the oxidation of sulfides and oxidative coupling of thiols as novel and reusable nano organometal catalysts. *Rsc Adv.* **5**, 92174-92183 (2015).
29. Malgas R., Mapolie S.F., Ojwach S.O., Smith G.S., Darkwa J. The application of novel dendritic nickel catalysts in the oligomerization of ethylene. *Catal. Commun.* **9**, 1612-1617 (2008).
30. Savostyanov V.S., Kritskaya D.A., Ponomarev A.N., Pomogailo A.D. Thermally initiated frontal polymerization of transition-metal nitrate acrylamide complexes. *J. Polym. Sci. Pol. Chem.* **32**, 1201-1212 (1994).
31. Fujita J., Nakamoto K., Martell A.E. Infrared spectra of metal chelate compounds .6. Normal coordinate treatment of oxalato metal complexes. *J. Chem. Phys.* **36**, 324 (1962).
32. Djordjevic C. Metal-oxygen stretching frequencies in some metal gamma-nitroacetylacetonates in solid and solution infrared spectra. *Spectrochim. Acta* **21**, 1018-1020 (1965).
33. Savostyanov V.S., *et al.* Preparation and reactivity of metal-containing monomers .21. Spontaneous polymerization of acrylamide coordinated to metal nitrates. *Bull. Russ. Acad. Sci. Div. Chem. Sci.* **41**, 1615-1620 (1992).
34. de Souza M.O., Mendes F.M.T., de Souza R.F., dos Santos J.H.Z. XPS characterization of nickel-acetylacetonate impregnated in NaX and NaY zeolites. *Microporous Mesoporous Mater.* **69**, 217-221 (2004).



## Synthesis through 3D printing: Formation of 3D Coordination Polymers - Supplementary Information

Oded Halevi<sup>1,2,3</sup>, Jingwei Chen<sup>2,3</sup>, Gurunathan Thangavel,<sup>2</sup> Samuel Alexander Morris,<sup>2</sup> Tal Ben Uliel<sup>4</sup>,  
Yaakov Tischler<sup>4</sup>, Pooi See Lee<sup>2,3\*</sup>, Shlomo Magdassi<sup>1,3\*</sup>

<sup>1</sup>Casali Center for Applied Chemistry, Institute of Chemistry, The Hebrew University of Jerusalem, Jerusalem, 91904, Israel. <sup>2</sup>School of Materials Science and Engineering, Nanyang Technological University, 639798, Singapore. <sup>3</sup>Singapore-HUJ Alliance for Research and Enterprise (SHARE), Nanomaterials for Energy and Energy-Water Nexus (NEW), Campus for Research Excellence and Technological Enterprise (CREATE), Singapore 138602. <sup>4</sup>Department of Chemistry, Bar-Ilan University, Ramat-Gan, 5290002, Israel.

Table S1 - Crystallographic data

Figure S1- Printing process scheme

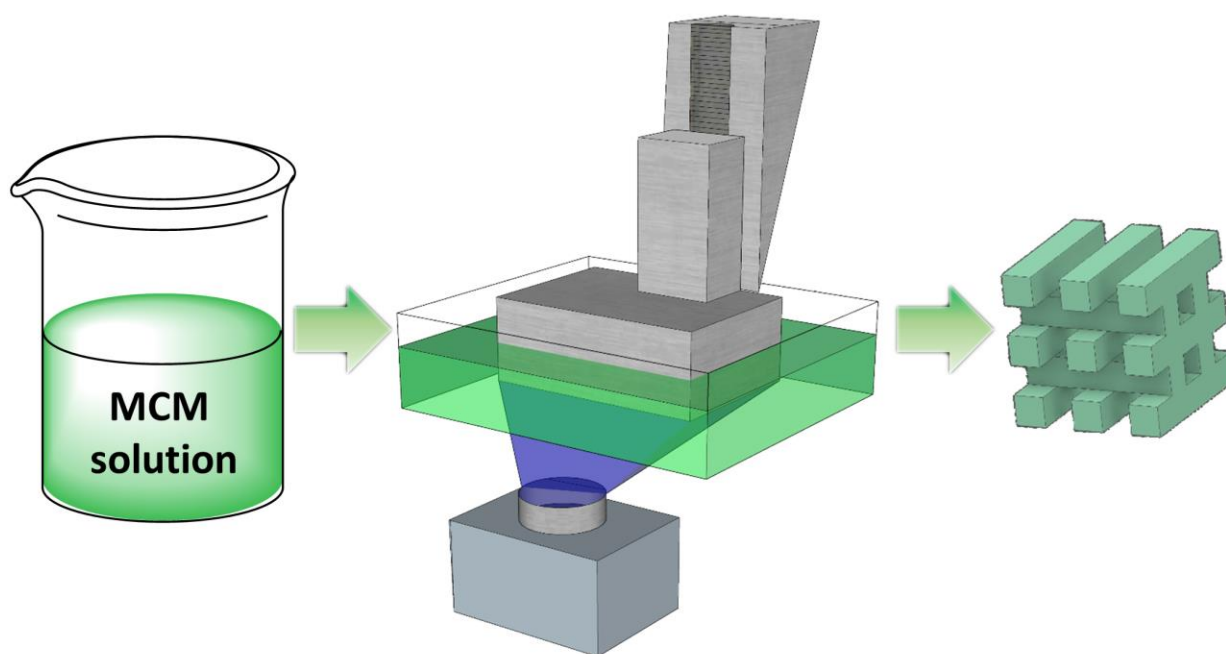
Figure S2- EDX

Figure S3- XPS

Table S2 - Printing Parameters

**Table S1. Crystallographic data and data collection parameters for [Ni(AAm)<sub>4</sub>(H<sub>2</sub>O)<sub>2</sub>](NO<sub>3</sub>)<sub>2</sub>**

Formula	C <sub>12</sub> H <sub>24</sub> N <sub>6</sub> Ni O <sub>12</sub>
M	503.04
<i>T</i> (K)	296(2)
$\lambda$ (Å)	0.71073
Crystal system	Triclinic
Space group	P $\bar{1}$ (2)
<i>a</i> (Å)	7.3043(5)
<i>b</i> (Å)	8.8329(6)
<i>c</i> (Å)	9.7206(7)
$\alpha$ (°)	65.294(3)
$\beta$ (°)	70.106(3)
$\gamma$ (°)	79.466(3)
<i>V</i> (Å <sup>3</sup> )	535.14(7)
<i>Z</i>	1
$\rho_{\text{calcd.}}$ (Mg/m <sup>3</sup> )	1.561
$\mu$ (mm <sup>-1</sup> )	0.977
Range of $2\theta$ (°)	2.41-34.368
Total reflection	43507
Independent reflection ( <i>R</i> <sub>int</sub> )	4466 [R(int) = 0.0246]
Data / restraints/ parameters	4466 / 30 / 191
Final <i>R</i> Indices (all data)	R1 = 0.0353, wR2 = 0.0881
Final <i>R</i> Indices ( <i>I</i> > 2sigma( <i>I</i> ))	R1 = 0.0300, wR2 = 0.0819



**Figure S1.** A scheme of the 3D-Printing of PolyNiComplex by DLP.



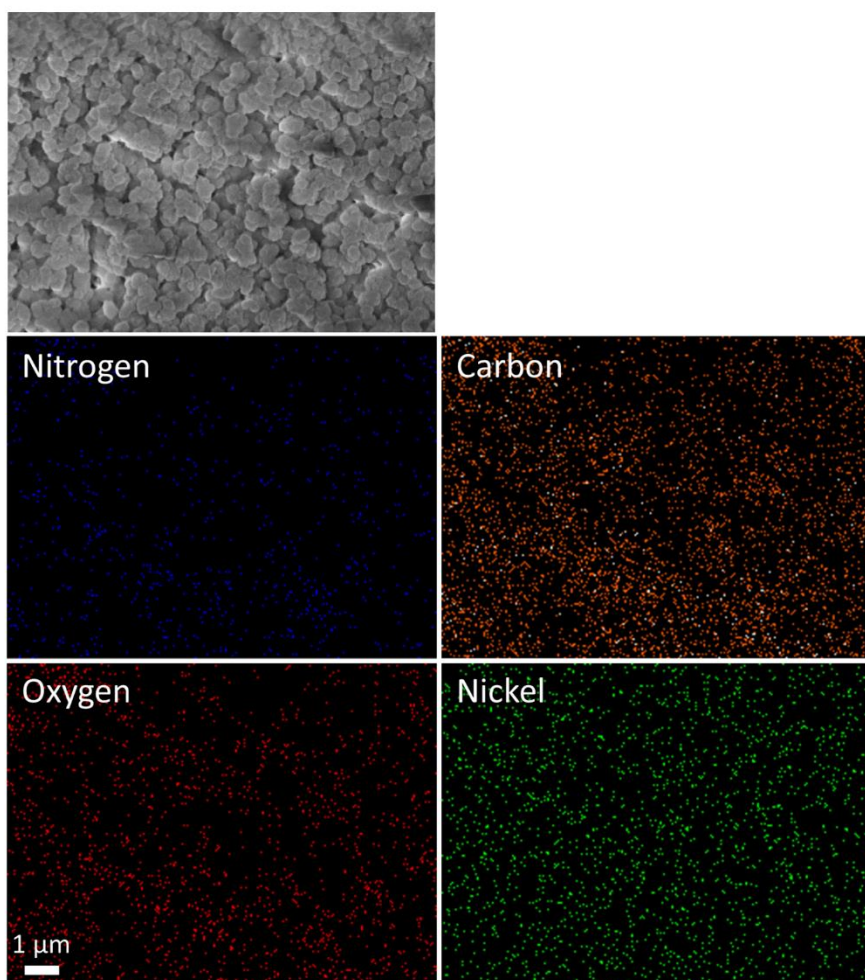


**Figure S2.** EDX measurement of the printed PolyNiComplex.

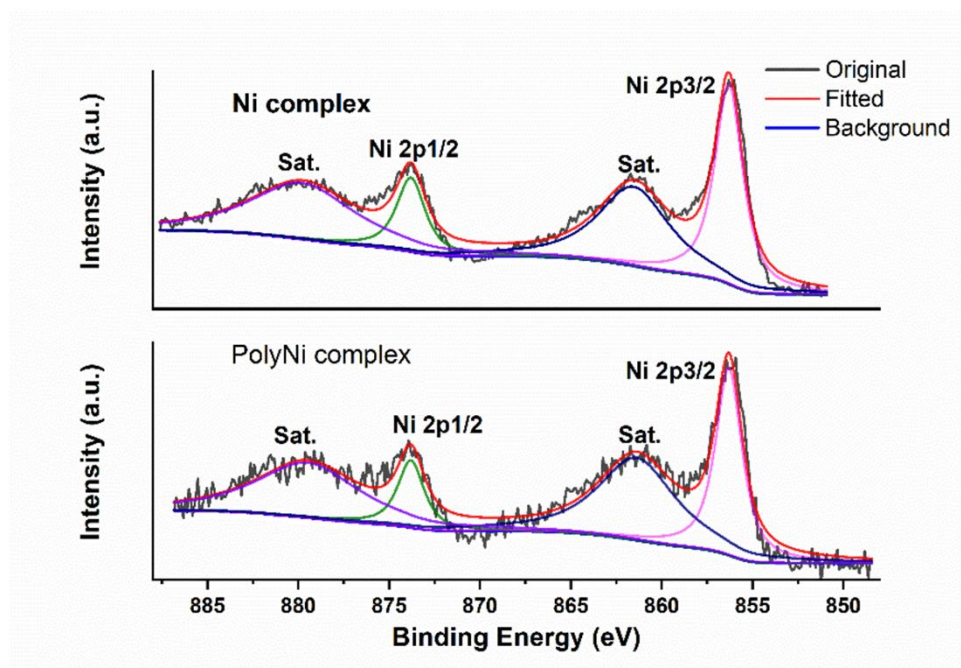


**Figure S3. XPS of Ni complex and polyNiComplex.**

**Table S2. Printing parameters for 3D printing of polyNiComplex.**

Parameter	Value
Light Intensity	39.880 [mW/cm <sup>2</sup> ]
Slice thickness	0.025 [mm]
Burn-In Exposure Time	5.000 [s]
Exposure Time	1.200 [s]
Separation Velocity	0.200 [mm/s]
Separation Distance	1.000 [mm]
Approach Velocity	0.500 [mm/s]
Slides Per Layer	1.000
Slide Velocity	10.000 [mm/s]
Burn-In Wait Time (After Exposure)	1.000 [s]
Burn-In Wait Time (After Separation)	1.000 [s]
Burn-In Wait Time (After Approach)	0.000 [s]
Burn-In Wait Time (After Slide)	0.000 [s]
Normal Wait Time (After Exposure)	1.000 [s]
Normal Wait Time (After Separation)	1.000 [s]
Normal Wait Time (After Approach)	0.000 [s]
Normal Wait Time (After Slide)	0.000 [s]

## **2.4. Chapter 4: Additive Manufacturing of Micrometric Crystallization Vessels and Single Crystals**

Published<sup>68</sup>: Halevi O., Jiang H., Kloc C., Magdassi S. Additive manufacturing of micrometric crystallization vessels and single crystals. *Scientific Reports* **6**, 36786 (2016).



# SCIENTIFIC REPORTS

OPEN

## Additive manufacturing of micrometric crystallization vessels and single crystals

Oded Halevi<sup>1,2</sup>, Hui Jiang<sup>2</sup>, Christian Kloc<sup>2</sup> & Shlomo Magdassi<sup>1</sup>

Received: 15 August 2016

Accepted: 17 October 2016

Published: 10 November 2016

We present an all-additive manufacturing method that is performed at mild conditions, for the formation of organic single crystals at specific locations, without any photolithography prefabrication process. The method is composed of two steps; inkjet printing of a confinement frame, composed of a water soluble electrolyte. Then, an organic semiconductor solution is printed within the confinement to form a nucleus at a specific location, followed by additional printing, which led to the growth of a single crystal. The specific geometry of the confinement enables control of the specific locations of the single crystals, while separating the nucleation and crystal growth processes. By this method, we printed single crystals of perylene, which are suitable for the formation of OFETs. Moreover, since this method is based on a simple and controllable wet deposition process, it enables formation of arrays of single crystals at specific locations, which is a prerequisite for mass production of active organic elements on flexible substrates.

Additive manufacturing processes such as inkjet and 3D printing are rapidly entering into new fields, bringing new approaches to what many relate to as the third industrial revolution. Among the benefits and advantages of these technologies is the production of tailor-made tools and even reaction vessels<sup>1,2</sup>. These items and devices can be designed for specific functions and purposes such as pressure durable reactors, incorporation of catalysts within reactor walls<sup>3</sup>, and formation of electronically active devices<sup>4,5</sup>.

Additive manufacturing can be highly efficient when combined with the technology of organic semiconductors. These materials have become a major area of research due to the maturity of devices based on them; such as organic light-emitting diodes (OLEDs), which are used for active-matrix OLED TV, or polymer LEDs for lighting. Therefore, intense efforts have led to the optimization of organic semiconductors technologies and discoveries of new materials<sup>6,7</sup>. These compounds demonstrate significant differences compared with inorganic-based electronic materials and devices; low manufacturing costs, solubility, flexibility, and simple processing methods are some of the qualities that make these materials so promising for utilization in various technologies<sup>8</sup>. Due to these differences, organic semiconductors seem to be preferred for low-energy manufacturing technologies like printing, and for instruments in which the space or element dimensions are crucial, such as printed electronics on the back of an active-matrix OLED TV screen. However, printing elements in the micrometers scale requires different materials properties than those designated for photolithographic based technologies and for the fabrication of electronic circuits in the nanometers scale. The most important issues are the physical properties of materials that would enable current conduction in long paths and efficient switching of such large devices. Therefore, due to the requirement of a well-controlled structure and quality of the electronic active parts of circuits, organic semiconductors would be preferred if made from small, high quality organic single crystals.

Polycyclic aromatic hydrocarbons (PAHs) such as perylene, rubrene, anthracene and their derivatives demonstrate semiconducting behavior due to their conjugated  $\pi$ -electrons system, and are used in many electronic devices such as organic field-effect transistors (OFETs)<sup>9</sup>. The highest electronic performances, are mostly obtained in devices that are based on single crystals, which demonstrate high purity, short and long-term structural order, and lack of grain boundaries<sup>10,11</sup>. However, until recently, the fabrication of such devices required the growth of crystals from solution or by physical vapor deposition (PVD)<sup>12</sup>. These two methods limit the applicability of single crystal based devices due to time consuming and crystal transferring difficulties; thus, the controlled and fast

<sup>1</sup>Casali Center of Applied Chemistry, Institute of Chemistry, The Hebrew University of Jerusalem, Jerusalem 91904, Israel. <sup>2</sup>School of Materials Science and Engineering, Nanyang Technological University, 639798, Singapore. Correspondence and requests for materials should be addressed to S.M. (email: magdassi@mail.huji.ac.il) or C.K. (email: CKLOC@ntu.edu.sg)

deposition of single crystals of these materials has become a challenging research area. In order to gain significant control over the growth of a large number of identical single crystals, forming active elements of electronic circuits, it is required to create a single nucleus at a specific location. Once a nucleus is formed, additional building blocks should be supplied to the nucleus for its growth. Some efforts have been made to gain control over the deposition of both organic and inorganic single crystals<sup>13–16</sup>. A highly effective approach to control the assembly and organization of functional materials in general, and specifically their formation of single crystals, is by spatial confinement. The importance of spatial confinement is due to the ability to control various features such as crystal orientation, location, the mean size of crystalline domains, and the ease of fabrication<sup>17</sup>. This was demonstrated for example by Moto *et al.*, where individual single crystals were grown by the deposition of solution into a defined confinement frame that enabled geometrical separation between nucleation control region (NCR) and growth control region (GCR)<sup>18</sup>. Another case in which spatial confinement enabled the formation of defined structures as presented by Valle *et al.*, who deposited laminin on highly hydrophobic, anti-adhesive substrates such as Teflon-AF by lithographically controlled wetting, in order to control cell adhesion and growth<sup>19</sup>. This deposition method has been also utilized by Gentili *et al.* to grow micrometric single crystals at specific locations by confining the solution of an organic semiconductor<sup>20</sup>.

However, in the field of crystallization, there are no reports in which only additive manufacturing technologies, such as inkjet printing, are utilized for the process of crystal growth. Inkjet printing is a powerful additive tool, which enables the deposition of many forms of liquid inks on a variety of substrates. It is a fast, cost-effective, highly precise and controllable method with a micrometric resolution<sup>21,22</sup>. Hasegawa *et al.* used a substrate with a pre-fabricated hydrophilic pattern, which was prepared by photolithography<sup>23</sup>, and utilized inkjet printing for the formation of single crystals at specific location. In their work, they inkjet printed an anti-solvent, followed by printing a semiconductor solution, thus resulting in crystal formation. Later, Park *et al.* used source and drain electrodes, which were made by PVD as nucleation sites, while depositing an organic solution into a confined hydrophilic area by inkjet printing<sup>24</sup>. The hydrophilic areas were also made by a photolithographic process, which was performed prior to printing. These methods enabled the formation of pure, micrometric single crystals, which were suitable for fabrication of high-performance devices such as OFETs. However, these and other methods require the combination of various fabrication and deposition processes, which mostly include photolithography, lift-off techniques, and solution deposition methods<sup>14,16,25</sup>. So far, no one has presented an all-additive manufacturing approach for the fabrication of the crystallization areas, followed by formation of single crystals also by deposition of the organic solution. This approach for the controlled growth of single crystals has many implications concerning the time and cost of the process and also its applicability to a variety of materials, substrates including plastics, at large production scale. Lately, inkjet printing has been used to etch microwells and to deposit a solution of an organic semiconductor<sup>26</sup>. However, this method enabled forming polycrystalline film in each microwell and not a single crystal.

Herein, we propose an additive manufacturing process, which is based on inkjet-printing for the controlled growth of **single crystals** at specific locations on the substrate. The proposed method utilizes the printer both as a high-resolution lithographic tool for the pre-fabrication of a complex confinement frame, in which the crystallization process takes place; and for the deposition of the semiconductor solution in a controlled and gradual manner, which enables separation of nucleation from growth. By this method, we printed single crystals of perylene, which are suitable for the formation of OFETs. Moreover, since this method is in essence a one-step wet deposition process it enables formation of arrays of single crystals at specific locations, which is a prerequisite for mass production processes of active organic elements on flexible substrates.

## Results

**Inkjet-printing of confinement frames.** The printing of confined frames was the first step towards obtaining a large number of individual micrometric crystals at specific location on surfaces that are as large as A4 sheet. In this method (Fig. 1), each frame would act as a micrometric crystallization vessel for the growth of a single crystal of perylene. Confinement of solutions can be achieved by inducing mechanical barrier due to a presence of solid walls, or by causing hydrophilic/lipophilic interactions.

In our approach we use both; printing of a hydrophilic frame that also acts as a mechanical barrier, while having a unique design, with pre-determined wall height and thickness. The building block of the wall is  $\text{AlCl}_3$ , which easily dissolves in water at relatively high concentrations, thus enables a sufficient load of the wall forming material. In addition, it does not precipitate too rapidly and adsorbs water from the air, thus minimizing typical print-head clogging problems during printing. Moreover, upon drying, the precipitated building block is a hydrated salt, therefore presenting hydrophilic characteristics that will enable confinement of organic solutions without the dissolution of the wall material. An  $\text{AlCl}_3$  solution in a 1:1 mixture of diethylene glycol butyl ether (DB) and deionized water was inkjet-printed onto a silicon wafer, to fabricate defined micrometric geometrical frames, as shown in Fig. 2a. The figure demonstrates a typical printed single micrometric crystallization frame with a specific design that will be explained later, and arrays of many such frames, which can be utilized for making arrays of single crystals as will be presented in the following sections. Each frame was fabricated by printing five layers of the electrolyte. The height of each wall of the frame is about 300 nanometers, and its width is about 60 micrometers. Obviously, these dimensions can be modified by changing the printing parameters and the physicochemical properties of the printing solution.

**Controlled crystallization of single crystals.** Following the printing of the confinement frames, the organic solution of the semiconductor was printed within the frames, to form a single crystal upon evaporation of the solvent. The chosen “printing ink” in this work was a concentrated solution of perylene in a 1:1 mixture of isophorone and propylene glycol phenylether (PPH). Although not considered a relatively high-performance organic semiconductor on its own, perylene was chosen due to its being a parent compound for many semiconducting



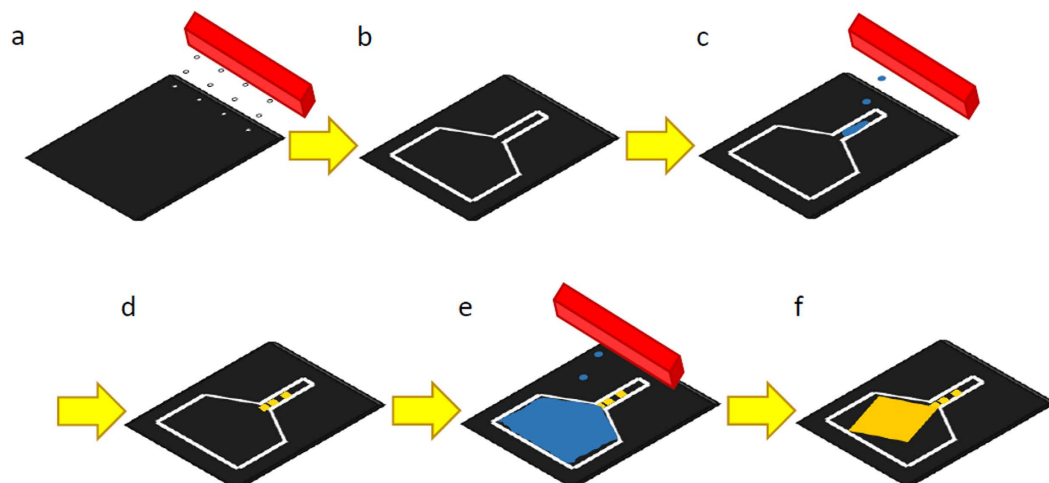


**Figure 1.** The method of inkjet printing of a single crystal. First,  $\text{AlCl}_3$  confinement frame is printed in the desired funnel-like shape (steps a,b). Then, several drops are printed into the narrow part of the frame that acts as the NCR (step c). As the solution evaporates, microcrystals are formed (step d). Following this, the solution is printed into the GCR, until it reaches the microcrystal (step e). The growth of a single crystal commences at the dividing line of the two regions (step f).

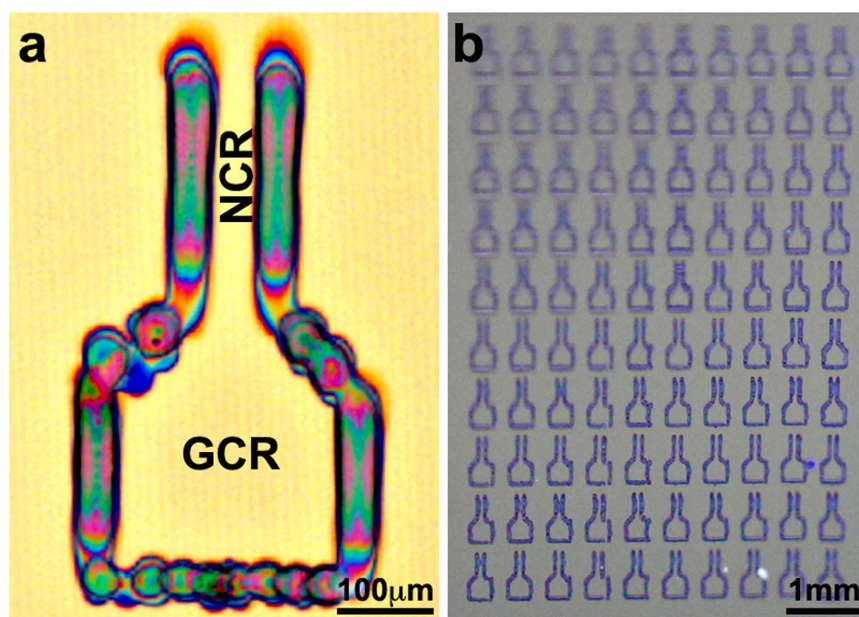


**Figure 2.** Inkjet-printed  $\text{AlCl}_3$  confinement frames on  $\text{SiO}_2/\text{Si}$ . (a) A single frame, height of  $325 \pm 41$  nm. (b) An array of  $\text{AlCl}_3$  frames.

materials<sup>27</sup>. Since we aimed to initiate the crystallization process at a specific site, we printed and tested confinement frames with a variety of geometrical shapes and sizes (see Supplementary Fig. S1). All frames were composed of a nucleation controlled region (NCR) connected to a growth controlled region (GCR). Figure 2a shows the optimal geometry of the printed frame. This structure was selected for two reasons: Firstly, to obtain a better separation between growth and nucleation processes, and secondly, to direct the flow of the solution towards the formed nucleus. The latter should minimize the dependency on the diffusion rate of perylene molecules in the solution towards the forming crystal, and lower the chances of nucleation and growth at undesired locations in the growth region. In this funnel-like shape of the frame, the NCR is narrower compared to the GCR, causing a capillary flow of the solution from the GCR towards the NCR.

Initial experiments on  $\text{SiO}_2/\text{Si}$  and polyethylene terephthalate (PET) substrates showed that the perylene solution, which was printed into the GCR, did not spread sufficiently fast into the NCR. Thus, upon solvent evaporation, instead of forming a single nucleus, several small needle-like perylene crystals were observed (Fig. 3a). Therefore, an active approach of forming a single nucleus was necessary. This was achieved by gradual deposition of the organic solution at a specific location in the NCR by precise printing of single droplets, enabling the



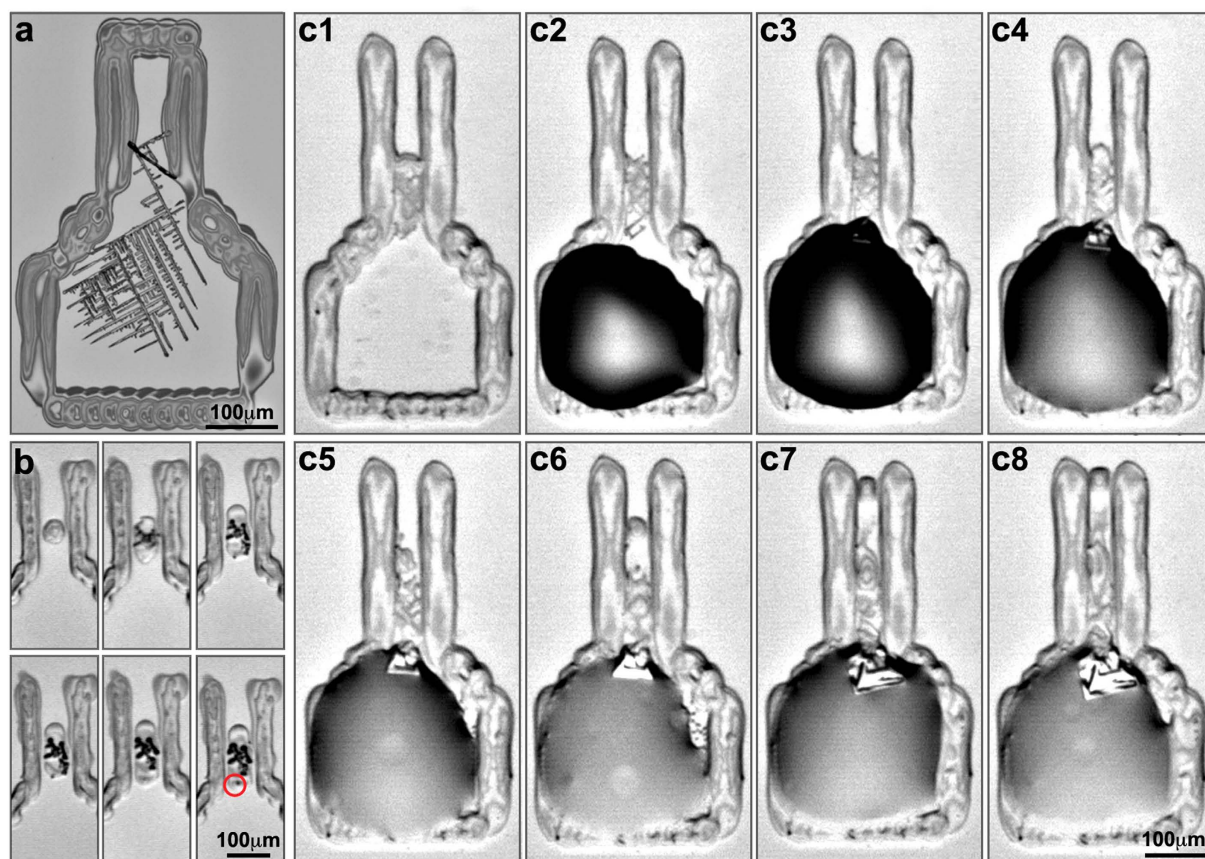


**Figure 3. The growth process of a crystal.** (a) Multi-crystalline needles of perylene, formed due to the absence of a single nucleus. (b) Formation of a nucleus in the NCR. Marked with a red circle is the microcrystal that reached the NCR-GCR dividing line and was later used as a nucleus for crystal growth. (c) Gradual growth of a crystal in the dividing line of the NCR and the GCR: Ink is deposited in the GCR and gradually spreads toward the microcrystal located in the NCR. Following is the growth of the single crystal in the GCR. (c2-c8) The directional flow of the solution from the GCR to the NCR is shown as the solution moves from the GCR to the edge of the NCR over time.

formation of a nucleus close to the GCR (Fig. 3b). In the majority of cases, a thick line of microcrystals were formed along the NCR, due to the spreading of the deposited solution along the walls of the sleeve-shaped region. In many cases, a single microcrystal reached the dividing line between the NCR and GCR, and could be used as a nucleus for the subsequent growth step which would take place within the GCR. After a nucleus has been formed, the perylene solution was further printed in the lower part of the GCR, to gradually fill the whole frame, thus initiating the growth of a single crystal at the desired location (Fig. 3c).

During the process we have encountered several challenges. Occasionally, the nucleus was formed more than 30 μm above the NCR-GCR dividing line. In those cases, the deposited solution in the GCR did not reach the nucleus sufficiently fast, resulting in the formation of several microcrystals dispersed within the confinement. Moreover, in cases when the growth started farther up in the NCR, its strong directional influence resulted in formation of a long needle-like crystal connected to a rectangular crystal at its end (see Supplementary Fig. S2). Also, despite of the directional flow of the solution from the GCR to the NCR, in many cases a single crystal was detached from the NCR and drifted to other parts of the GCR (Fig. 4a and Supplementary Fig. S3). However, as long as no additional nuclei drifted away, a single crystal was indeed formed at the center of the frame (Fig. 4b,c). The high quality and uniformity of the single crystals were investigated by a polarized optical microscope; Fig. 5 demonstrates the uniform darkening of the crystal due to the rotation of the polarizing lens.

Following the printing and crystallization process, the samples were washed with cold isopropyl alcohol to remove the excess solvent (see Supplementary Fig. S2). As can be seen in Fig. 4b,c the excess of nuclei remained in the nucleation region, or were washed away by the isopropyl alcohol. Preliminary experiments showed that the deposited aluminum salt dissolves when exposed to water, however, at this stage we could not completely remove the frames without physically damaging the organic crystals. To determine the yield of the process, three independent printing experiments were conducted. In each experiment, an array of about 40 frames was printed. Following that, the perylene ink was printed to form single crystals (Supplementary Fig. S4), according to the procedure described in the experimental section. A success was considered as follows: obtaining only one single crystal, which is located in the growth control region, with a minimal top-side surface area of 2,500 μm<sup>2</sup>. The calculated yield of the process was 32 ± 8%.

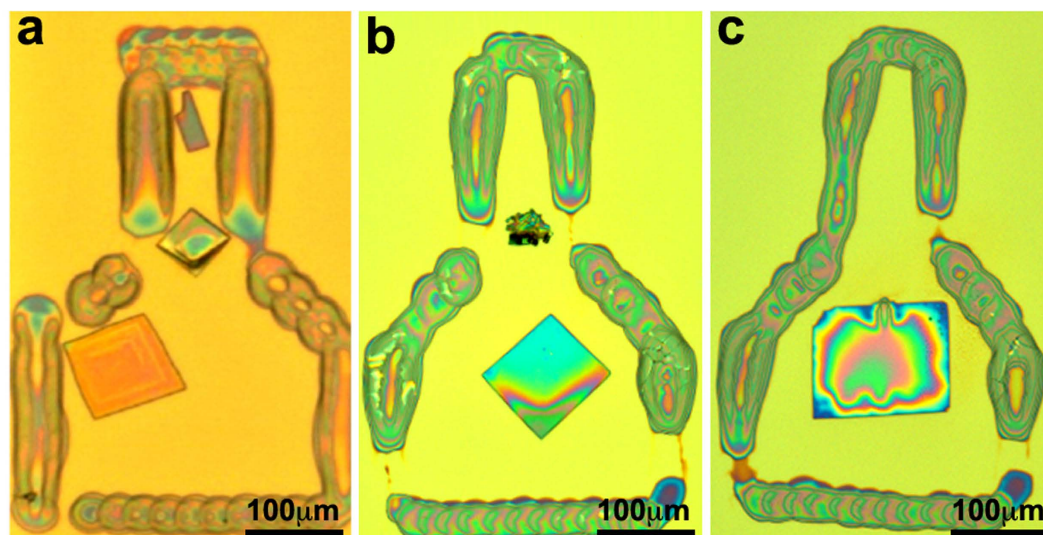


**Figure 4.** Three single crystals in  $\text{AlCl}_3$  confinement frames following their washing with isopropyl alcohol. (a) Two crystals grown, one at the NCR-GCR dividing line and one in the GCR. This was caused due to the drift of a nucleus from the NCR to the GCR during the growth step. (b) A single crystal grown inside the  $\text{AlCl}_3$  confinement frame. Here, the excess nuclei are gathered in the NCR following the washing with isopropyl alcohol. (c) A single crystal, located in the center of the confinement frame due to its drift from the NCR-GCR dividing line during its growth. The excess nuclei in this case were washed away by the isopropyl alcohol.

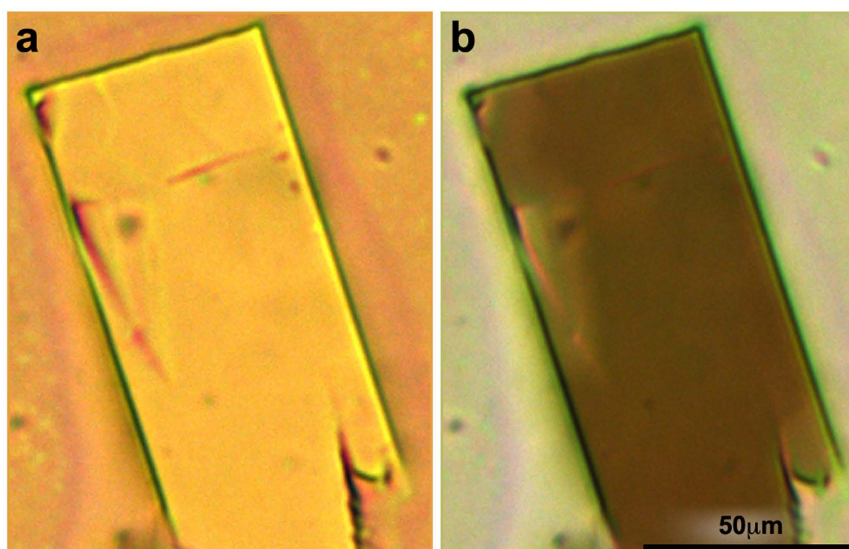


**Figure 5.** Microscope imaging of the single crystal in the confined frame on PET with two polarizers. Darkening occurred at a  $50^\circ$ .

**Device fabrication and characterization.** The size of the printed perylene single crystal was typically  $\sim 100 \mu\text{m} \times 100 \mu\text{m}$  (Fig. 4), which was suitable to make a field-effect transistor. Individual single-crystal perylene transistors have been made as shown in Fig. 6, in a top-contact, bottom-gate configuration. Copper grid was used as the mask for making the symmetrical electrodes (Au thin film,  $\sim 100 \text{ nm}$ ) by thermal evaporation, performed directly on the single crystals present within the frame. All transistors were fabricated and characterized in air, under ambient conditions. Typical p-type characteristic was observed in perylene single crystal field-effect transistor, having a mobility of  $\sim 4.0 \times 10^{-4} \text{ cm}^2 \text{ V}^{-1} \text{ s}^{-1}$ . This value is in the same range reported previously for perylene single crystal devices made by solution growth methods<sup>28</sup>.

It should be emphasized that the focus of the paper is to show for the first time that by using inkjet printing, which is a digital wet deposition process, we could induce crystallization at specific locations, without using any photolithographic processes. The process was demonstrated for an organic semiconductor, and therefore we performed a limited number of experiments on device fabrication. Making a high quality transistors was very challenging, due to factors such as residual solvents and the large thickness of the crystals ( $208 \pm 80 \text{ nm}$ ) compared to

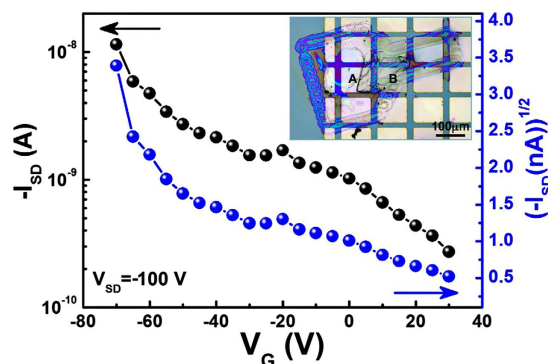


**Figure 6.** Transfer curve of individual perylene single crystal field-effect transistor. The inset is the optical image of the corresponding device, the channel is bridged between A and B.

those fabricated from vapor phase, which showed two or three orders of magnitude higher mobility<sup>27</sup>. Another possibility for the observed low transistor performance of the discussed device could be unintentional doping of the grown perylene crystal by hydrated  $\text{AlCl}_3$ . Therefore, we performed energy dispersive X-ray analysis (EDXA) on four crystals to evaluate presence of Al or Cl (analysis performed on crystals close to and far from the frame). In all cases we could not find presence of Al and Cl, as shown in Supplementary Fig. S5. It is worth noticing that many polycrystalline perylene devices showed no field-effect activity at all.

## Conclusions

We have developed an all-additive manufacturing method for the controlled formation of a large number of individual single crystals of organic functional materials, at pre-designed locations. For the first time, we utilized the printer not only for solution deposition but also for the fabrication of a confining frame that enables the controlled growth of a single crystal within a specific region. This is the first step towards an all-inkjet printing process for production of single crystal-based devices. Moreover, since all processes take place under mild conditions, it will open a way for a variety of substrates and organic materials including semiconductors that could not be used until now. Currently, further work is being conducted to gain better control over the location of the single crystals, along with combining the controlled crystallization process with fabricating arrays of full devices including printed metallic electrodes. In addition, since the mobility of the printed crystals is lower than PVD grown crystals, further work should be done regarding controlling the crystal thickness and the selection of organic semiconducting materials with which the interaction of solvent residues will not reduce the mobility. The process described here presents a proof of concept for a wet deposition organic circuit technology in which individual steps have been developed and the assembly of these steps into a full production process is still required. It should be mentioned that by using a similar procedure described for printing on silicon wafers, we were able to grow single crystals also on PET, which is important for plastics electronics, although further optimization is required to increase the yield. We expect that by utilizing inkjet printing both for fabricating the crystallization vessel and for solution deposition, organic single crystal of various functional materials will become more accessible and their electronic and optical properties may be utilized in applications such as electronic papers or textiles.

## Methods

**Inkjet printing lithography of  $\text{AlCl}_3$  confinement frames.** The ink was a 5%wt solution of  $\text{AlCl}_3 \cdot 6\text{H}_2\text{O}$  ( $\geq 99\%$ , Fluka) in a 1:1 mixture of dionized water and diethylene glycol butyl ether ( $\geq 99\%$ , Aldrich). The substrates were polyethylene terephthalate, PET, (125  $\mu\text{m}$  thickness, Jolybar Israel) and n-doped Silicon wafers with a 200 nm layer of  $\text{SiO}_2$  (Dashro Trade). The substrates were pre-cleaned by sonication, first in an ethanol (96%, Bio-lab) bath followed by an isopropyl alcohol (CP, Bio-Lab) bath and finally dried with a stream of  $\text{N}_2$ . Inkjet printing of the confinement frames was carried out using an Omnijet100 printer (Unijet, Korea), with a Dimatix 1 picoliter printing head. **Printing on  $\text{SiO}_2/\text{Si}$ :** The substrates temperature during printing was 60 °C. Printing was conducted at 800 Hz, and 1000 dpi. The waveform consisted of a 2  $\mu\text{s}$  rise time to 30 Volts, another rise time of 6  $\mu\text{s}$  to 40 volts and a 3  $\mu\text{s}$  fall time to 0 volts. Each confinement frame consisted of 5 layers. **Printing on PET:** Same as on  $\text{SiO}_2/\text{Si}$  with the following changes: The substrates temperature during printing was 65 °C. Printing was conducted at 500 Hz. Each confinement frame consisted of 10 printed layers. The thickness measurements were conducted by a Dektak 150 profiler (Veeco, USA). Elemental analysis was performed by using SEM microscope (XHR Magellan 400L) equipped with Energy-dispersive X-ray (EDX) probe (Oxford X-MAX, Oxford Instruments).

**Perylene crystal growth.** The perylene ink was prepared by dissolving 5.6 mg of perylene ( $\geq 99.5\%$ , Aldrich) in a mixture of 1 g of isophorone (98%, Acros) and 1 g of propylene glycol phenyl ether ( $\geq 93\%$ , Aldrich). After 30 minutes of sonication, the saturated solution was left at room temperature overnight and then filtered. 1 mL of the ink was loaded into the cartridge with a 10 pL Dimatix printing head. **Printing on  $\text{SiO}_2/\text{Si}$ :** The substrates temperature during printing was 35 °C. The printing head temperature was 27 °C. Printing of single drops was conducted at 1000 Hz. First, three drops were printed into the middle of the NCR, and the printed solution was kept for several minutes, to enable formation of the nucleus. Once a nucleus was formed, 100 drops



were printed in the bottom third of the GCR, followed by two additional repetitions of 50 drops each at the same location. The solvent was allowed to evaporate at the same temperature and a single crystal was formed after a few minutes. Following the formation of the crystals, the substrate was gently washed with cold isopropyl alcohol and dried with N<sub>2</sub>. **Printing on PET:** Same as on SiO<sub>2</sub>/Si with the following changes: The substrates temperature during printing was 35 °C. First, nine drops were printed into the middle of the NCR. Once a sufficient nucleus formed, four repetitions of 50 drops were printed into the bottom third of the GCR.

**Device fabrication and characterization.** Organic field-effect transistors based on the individual planar perylene single crystals were fabricated. A thin-bar copper grid was used as a mask for gold electrodes by thermal evaporation. The grid was directly put on the top surface of perylene single crystals and a scotch tape was used to stick the two surfaces together. Following that, the device was put into vacuum for thermal evaporation of gold thin films, which acted as the source and drain electrodes. The heavily-doped n-type silicon wafer was used as a gate electrode. *I-V* characteristics of perylene single-crystal FETs were measured using a Keithley 4200-SCS and a micromanipulator probe station in a shielded box at room temperature in air. To verify that the aluminum frame does not contribute to the charge transport property, blank measurements of the devices comprising solely the frame and the electrodes were conducted as well.

**Image acquisition.** Photos of the printing and crystallization processes were taken with the built-in camera of the Omnijet 100 printer. Photos of the grown crystals were taken with a MicroPublisher 5.0 RTV camera (QImaging, Canada) on top of a CX41 optical microscope (Olympus).

## References

1. Therriault, D., White, S. R. & Lewis, J. A. Chaotic mixing in three-dimensional microvascular networks fabricated by direct-write assembly. *Nat. Mater.* **2**, 265–271 (2003).
2. Kitson, P. J., Marshall, R. J., Long, D. L., Forgan, R. S. & Cronin, L. 3D Printed High-Throughput Hydrothermal Reactionware for Discovery, Optimization, and Scale-Up. *Angew. Chem. Int. Ed.* **53**, 12723–12728 (2014).
3. Kitson, P. J. *et al.* 3D printing of versatile reactionware for chemical synthesis. *Nat. Protoc.* **11**, 920–936 (2016).
4. Molina-Lopez, F., Briand, D. & de Rooij, N. F. All additive inkjet printed humidity sensors on plastic substrate. *Sensor. Actuat. B-Chem.* **166**, 212–222 (2012).
5. Ostfeld, A. E., Deckman, I., Gaikwad, A. M., Lochner, C. M. & Arias, A. C. Screen printed passive components for flexible power electronics. *Sci. Rep.* **5**, 15959 (2015).
6. Allard, S., Forster, M., Souhace, B., Thiem, H. & Scherf, U. Organic semiconductors for solution-processable field-effect transistors (OFETs). *Angew. Chem. Int. Ed.* **47**, 4070–4098 (2008).
7. Liao, C. *et al.* Flexible Organic Electronics in Biology: Materials and Devices. *Adv. Mater.* **27**, 7493–7527 (2015).
8. Jacob, M. Organic Semiconductors: Past, Present and Future. *Electronics* **3**, 594–597 (2014).
9. Seki, S., Saeki, A., Sakurai, T. & Sakamaki, D. Charge carrier mobility in organic molecular materials probed by electromagnetic waves. *Phys. Chem. Chem. Phys.* **16**, 11093–11113 (2014).
10. Dong, H., Fu, X., Liu, J., Wang, Z. & Hu, W. 25th Anniversary Article: Key Points for High-Mobility Organic Field-Effect Transistors. *Adv. Mater.* **25**, 6158–6182 (2013).
11. Coropceanu, V. *et al.* Charge transport in organic semiconductors. *Chem. Rev.* **107**, 926–952 (2007).
12. Jiang, H. & Kloc, C. Single-crystal growth of organic semiconductors. *MRS Bull.* **38**, 28–33 (2013).
13. Aizenberg, J., Black, A. J. & Whitesides, G. M. Control of crystal nucleation by patterned self-assembled monolayers. *Nature* **398**, 495–498 (1999).
14. Briseno, A. L. *et al.* Patterning organic single-crystal transistor arrays. *Nature* **444**, 913–917 (2006).
15. Diao, Y. *et al.* Solution coating of large-area organic semiconductor thin films with aligned single-crystalline domains. *Nat. Mater.* **12**, 665–671 (2013).
16. Zheng, W. *et al.* Patterning two-dimensional chalcogenide crystals of Bi<sub>2</sub>Se<sub>3</sub> and In<sub>2</sub>Se<sub>3</sub> and efficient photodetectors. *Nat. Commun.* **6**, 6972, doi: 10.1038/ncomms7972 (2015).
17. Gentili, D., Valle, F., Albonetti, C., Liscio, F. & Cavallini, M. Self-Organization of Functional Materials in Confinement. *Acc. Chem. Res.* **47**, 2692–2699 (2014).
18. Goto, O. *et al.* Organic Single-Crystal Arrays from Solution-Phase Growth Using Micropattern with Nucleation Control Region. *Adv. Mater.* **24**, 1117–1122 (2012).
19. Valle, F. *et al.* Stable Non-Covalent Large Area Patterning of Inert Teflon-AF Surface: A New Approach to Multiscale Cell Guidance. *Adv. Eng. Mater.* **12**, B185–B191 (2010).
20. Gentili, D. *et al.* Growth and Manipulation of Organic Semiconductors Microcrystals by Wet Lithography. *Adv. Funct. Mater.* **26**, 2387–2393 (2016).
21. Kang, B., Lee, W. H. & Cho, K. Recent Advances in Organic Transistor Printing Processes. *ACS Appl. Mater. Interfaces* **5**, 2302–2315 (2013).
22. Tekin, E., Smith, P. J. & Schubert, U. S. Inkjet printing as a deposition and patterning tool for polymers and inorganic particles. *Soft Matter* **4**, 703–713 (2008).
23. Minemawari, H. *et al.* Inkjet printing of single-crystal films. *Nature* **475**, 364–367 (2011).
24. Kim, Y. H., Yoo, B., Anthony, J. E. & Park, S. K. Controlled Deposition of a High-Performance Small-Molecule Organic Single-Crystal Transistor Array by Direct Ink-Jet Printing. *Adv. Mater.* **24**, 497–502 (2012).
25. Shaw, L. & Bao, Z. The Large-Area, Solution-Based Deposition of Single-Crystal Organic Semiconductors. *Isr. J. Chem.* **54**, 496–512 (2014).
26. Kwak, D., Lim, J. A., Kang, B., Lee, W. H. & Cho, K. Self-Organization of Inkjet-Printed Organic Semiconductor Films Prepared in Inkjet-Etched Microwells. *Adv. Funct. Mater.* **23**, 5224–5231 (2013).
27. Jiang, H. *et al.* Atomically Flat, Large-Sized, Two-Dimensional Organic Nanocrystals. *Small* **9**, 990–995 (2013).
28. Liao, Q., Zhang, H., Zhu, W., Hu, K. & Fu, H. Perylene crystals: tuning optoelectronic properties by dimensional-controlled synthesis. *J. Mater. Chem. C* **2**, 9695–9700 (2014).

## Acknowledgements

This research was partially supported by the Singapore National Research Foundation under the CREATE program: Nanomaterials for Energy and Water Management and by the Israel Nanotechnology Initiative under the FTA program.

## Author Contributions

H.O. led and was involved in all aspects of the project beside the fabrication and characterization of the OFET. J.H. led the OFET fabrication and electrical measurements. M.S. and K.C. were in charge and advised on all parts of the project.

## Additional Information

**Supplementary information** accompanies this paper at <http://www.nature.com/srep>

**Competing financial interests:** The authors declare no competing financial interests.

**How to cite this article:** Halevi, O. *et al.* Additive manufacturing of micrometric crystallization vessels and single crystals. *Sci. Rep.* **6**, 36786; doi: 10.1038/srep36786 (2016).

**Publisher's note:** Springer Nature remains neutral with regard to jurisdictional claims in published maps and institutional affiliations.



This work is licensed under a Creative Commons Attribution 4.0 International License. The images or other third party material in this article are included in the article's Creative Commons license, unless indicated otherwise in the credit line; if the material is not included under the Creative Commons license, users will need to obtain permission from the license holder to reproduce the material. To view a copy of this license, visit <http://creativecommons.org/licenses/by/4.0/>

© The Author(s) 2016

## Supplementary information

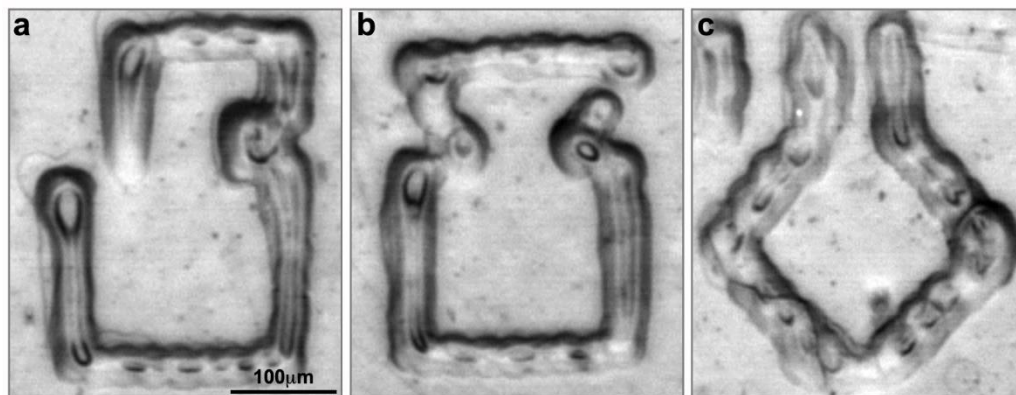
### Additive manufacturing of micrometric crystallization vessels and single crystals

*Oded Halevi<sup>1,2</sup>, Hui Jiang<sup>2</sup>, Christian Kloc<sup>2\*</sup>, Shlomo Magdassi<sup>1\*</sup>*

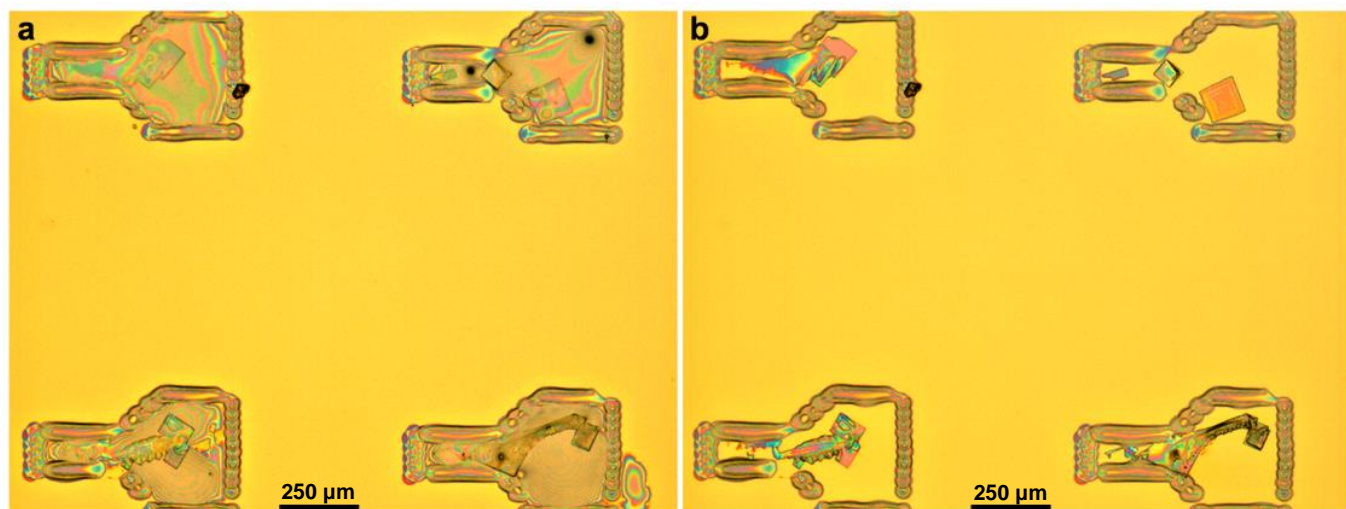
<sup>1</sup> Casali Center of Applied Chemistry, Institute of Chemistry  
The Hebrew University of Jerusalem Jerusalem, 91904, Israel,

<sup>2</sup> School of Material Science and Engineering  
Nanyang Technological University, 639798, Singapore

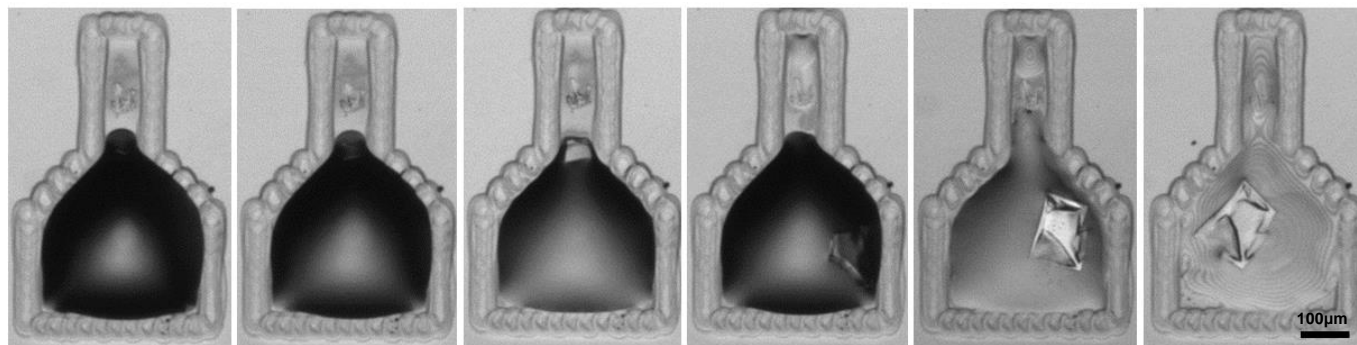
\* Correspondence to magdassi@mail.huji.ac.il



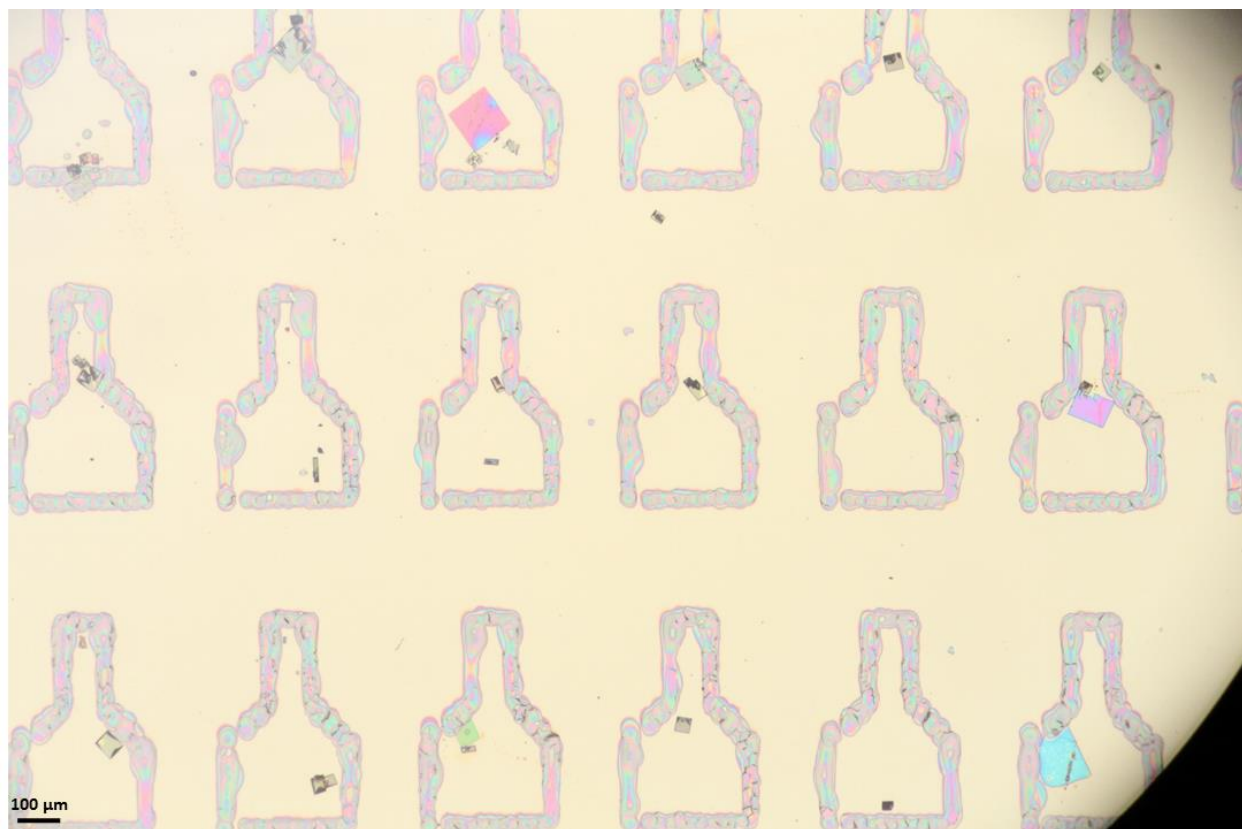
Supplementary Figure S1: Various geometries of confinement frames on PET.



**Supplementary Figure S2: An array of perylene crystals on Si/SiO<sub>2</sub> demonstrating the strong directional influence of the NCR on their growth.** In the case of the two bottom frames, the growth commenced deep in the NCR, which resulted in a long needle-like crystal from which additional crystals were developed in the GCR. (a) Before washing with isopropyl alcohol. (b) After washing with isopropyl alcohol.

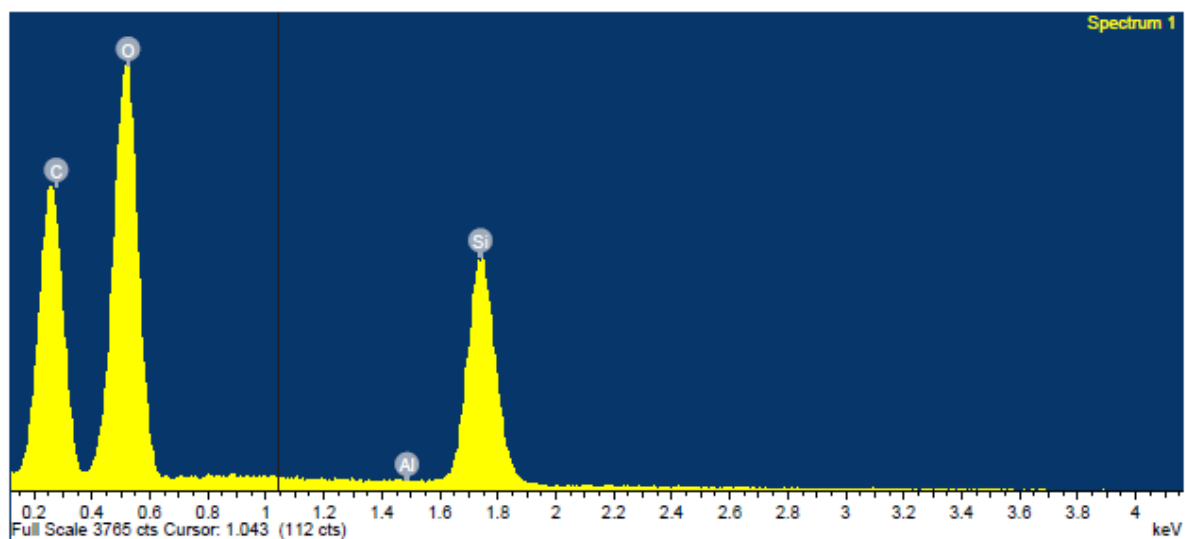


**Supplementary Figure S3: The drift of a crystal from the NCR-GCR dividing line during growth.**



**Supplementary Figure S4: An array of confinement frames with single crystals.**





Spectrum processing :  
No peaks omitted

Processing option : All elements analyzed (Normalised)  
Number of iterations = 4

Standard :  
C CaCO3 1-Jun-1999 12:00 AM  
O SiO2 1-Jun-1999 12:00 AM  
Al Al2O3 1-Jun-1999 12:00 AM  
Si SiO2 1-Jun-1999 12:00 AM

Element	App Conc.	Intensity Corrn.	Weight%	Weight% Sigma	Atomic%
C K	297.27	1.3323	31.60	0.26	43.17
O K	569.90	2.1114	38.23	0.24	39.21
Al K	0.00	1.1686	0.00	0.00	0.00
Si K	232.76	1.0926	30.17	0.23	17.63
Totals			100.00		

Supplementary Figure S5: EDXA spectrum of perylene crystals inside an  $\text{AlCl}_3$  frame.

### 3. Discussion and Conclusions

This section will discuss the results and contributions of each chapter, concluding its total scientific impact, and its implications regarding the printing technology as a tool in the chemist's arsenal.

#### 3.1. Discussion and Summary

In the first and second chapters we focused on heterogeneous mixtures of inorganic particles, such as MOFs and zeolites, with organic polymers. The objective was to gain control over the macrostructure while maintaining their functionality and overcoming their chemical and mechanical limitations. In **paper 1**, which discusses the 3D-printing of the Cu-BTC MOF, we have encountered several challenges. It was necessary to prevent the blockage of the pores and maintain the crystal structure of the MOF, as well as to enhance its hydrolytic stability in the printed structure. We have made use of several chemical principles to overcome these challenges, for example, dispersing the MOF in a liquid monomer without additives and causing a phase separation of the MOF from the polymer during printing. This approach resulted in a polymeric-rich phase and a MOF-rich phase, which enabled the accessibility of the MOF's pores. Also, a hydrophobic polymeric matrix was formed, which protected the MOF's copper centers from the water molecules and increased its stability in aqueous solutions.

As mentioned in the introduction, despite the huge number of potential applications, there are limited examples of the actual utilization of MOFs for commercial and industrial purposes. A core mission of our work in this part was to promote the compatibility of MOFs for various environmental and chemical scenarios, and assist their transition from the research laboratories to the industry. The progress demonstrated in this work is already showing its contribution to MOFs utilization, as the 3D-printed structures are now being tested by our collaborators for various applications such as columns for hydrogen purification (Figure 1).

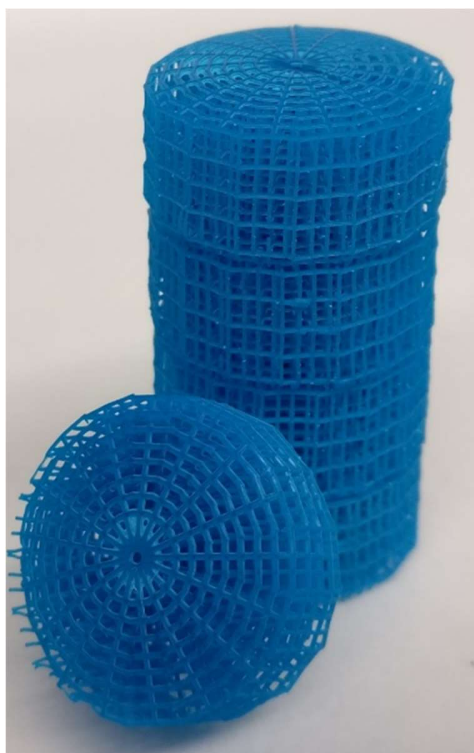


**Figure 1.** 3D-printed MOF columns that are currently being investigated for hydrogen purification.

In **paper 2**, we focused on printing zeolites in confined structures. As zeolites are already being used widely in the industry, 3D-printing can contribute to their better and more efficient utilization in existing applications and open the door to new potential applications that could not be addressed by these materials so far. An example for such application is the decontamination of nuclear waste water. Although zeolite 4A and chabazite are already being used for this purpose, there are several limitations and disadvantages as a result of their fine powder form. Here, compared with the previous paper, a significantly higher loading was required, and there was no issue of water sensitivity. Therefore, different chemical considerations were taken into account, such as controlling the porosity of the polymeric matrix and formulating a 3D-printable ink that would result in a uniform distribution of the zeolite particles across the printed structure. The printed 3D zeolite structures had the same total  $^{137}\text{Cs}^+$  and  $^{90}\text{Sr}^{2+}$  ion exchange capacity as the pristine zeolites,

without the disadvantages of the powders. This is the first example of a 3D-printed zeolite structure for ion exchange purposes, and we believe that the advantages arising from this method will lead to its adaptation in other ion exchanging zeolites systems.

In the third chapter (**paper 3**) we developed a new concept for utilization of soluble coordination metal complexes as monomeric building blocks to print 3D object of coordination polymers (CPs). We utilized the 3D-printer as a synthesis tool, gaining control over the structure of the material both in the macro- and molecular levels. This concept is presented here for the first time.

In addition, compared with the printed MOF-embedded polymer reported in **paper 1**, the coordination polymer in **paper 3** is both the matrix and the active material. Therefore, an inorganic complex with polymerizable ligands, nickel tetra-acrylamide, was synthesized as the monomer, and was formulated as a 3D-printable ink. This complex was then printed with the DLP printer to form the desired coordination polymer. The nickel coordination polymer, and similar CPs that can be printed by the same method, may have various potential applications in the future, such as 3D sensors of small-molecules and reaction vessels with built-in catalysts. We believe that this research work opens the door to the fabrication of a whole new group of materials as functional 3D structures.

In chapter 4 (**paper 4**), our objective was to develop an inkjet-printing method for the formation of OSCs single crystals in predesigned locations. For this purpose, we have utilized the inkjet 2D-printer to control the intermolecular self-assembly process of crystallization. An all-inkjet printing method based on the printing of confined structures as crystallization vessels was developed. In order to achieve control over the process, the nucleation and growth steps were separated over both time and location. The key challenge in this work was to gain control over the formation of a single nucleus in a specific location, and it was achieved by printing hydrophilic confining frames with specific geometry and size.

### 3.2. Insights and Perspectives

In this work, we utilized the printer as a chemistry laboratory tool, similar to the reaction vessel, stirrer, the distillation kit and any other labware. We have used it for synthesis, crystallization, and as a fabrication tool, according to the scientific needs of each project, demonstrating its powerful capabilities and benefits.

We have achieved structural control by printing, across three different levels of resolution: (1) the micro- and nano-metric levels (**papers 1-4**), as the morphologies of the printed objects were designed and tailored; (2) the intermolecular level, as the crystallization process in **paper 4** was controlled over time and location; and in **paper 2** the solvent-solute interactions were exploited to form porous structures. (3) The molecular level (**paper 3**), by synthesizing coordination polymers from metal complexes. A central common denominator that is demonstrated throughout this PhD thesis, is the ability to control various structural resolutions and functionality via printing. This required deep understanding of the chemical inter- and intramolecular interactions of the various compounds in this work.

In conclusion, this thesis has several major contributions:

- MOFs have been investigated for more than 20 years, with many resources and large amounts of money invested in this field. The slow progress in application of MOFs in the industry, made some members of the scientific community believe (off the record) that there was a MOF bubble waiting to burst sometime in the near future. Motivated by our love to inorganic chemistry, we believe that our work helps to reduce the risks of that happening, as it pushes the MOFs towards applicability. Furthermore, one of the common arguments against MOFs is their relatively low environmental stability. The work we presented is an example of how clever design and choice of materials can assist in overcoming the MOFs limitations and enhance their applicability.
- In chapter 3, we have opened the door for a new class of materials. Future design of monomers with specific polymerizable ligands and metal ions may result in having both the properties attributed to coordination polymers, and to conventional 3D-printed polymeric structures. A promising future research is printing CPs with unsaturated coordination sites

on the metal center, which will enable the binding of electron donors and therefore increase the chemical activity of the polymer.

- Among the chapters that are part of this PhD thesis, we demonstrated one of the first examples of 3D-printed MOFs (**paper 1**), and one of the first cases of inkjet-printing for the controlled growth of single crystals in predesigned locations (**paper 4**). Also, **paper 2** shows the first example, in which zeolites are 3D-printed for ion-exchange purposes, and in **paper 3** it is the first example of using the 3D-printer to synthesize coordination polymers.

Future academic research based on this PhD thesis should focus on:

- Printing structures with more than one MOF/Zeolite compound, for parallel or conjugated processes, such as catalysis by one, followed by separation of the product by the second compound.
- Investigating hybrid structures that combine MOF and Zeolite in one structure can be very interesting as well, benefiting from the advantages of each family of materials.
- Following **paper 3**, further investigation of the porosity and its tailoring will take place. It is important to gain control over the pores size and the total surface area for future applications.
- Synthesis through printing of conjugated CPs for the formation of conducting 3D-structures and for energy storage applications.

This work also contributes to the overall world-wide effort of advanced manufacturing (Industry 4.0), as it sets a clear example for how printing techniques can be developed and extended in order to enhance the applicability of functional materials. As the principles of industry 4.0 set the guidelines for the future industry, automation and data collection are the main trends. The 2D- and 3D-printing methods and materials developed in this work fit these trends very well:

- Chapters 1 to 3 - These chapters demonstrate that 3D-printing of porous and adsorptive materials enable the customization of their shapes and even chemical features. So far, the traditional powder or beads-filled columns forced a specific mode of operation: transport of the fluid or the gas phases through the particles beds in columns. Now

customized shapes can be fabricated in a relatively short time. Therefore, optimizations of the adsorptive shapes and structures can be done through repeating cycles of 3D-printing, experimental analysis and further modification of the shapes based on the accumulated data. Through this process, new methods can be developed that may replace the traditional flow-column methodology, and increase the efficiency of the desired process. Further demonstration of the capabilities and knowledge that were developed and acquired throughout these chapters, can be found in our work together with the lab of Prof. Felix Zamora and Prof. Pilar Amo Ochoa from The Autonomous University of Madrid. In this work, 3D polymeric structures embedded with a solvatochromic 1D copper CP were 3D-printed, forming a 3D colorimetric water sensor<sup>69</sup> (appendix I).

- Chapter 4 - So far, crystallization of OSC was performed mostly in solutions, which makes it very difficult to automate, since careful and delicate selection should be done to isolate the single crystals before further fabrication. We believe that the 2D-printing method of single crystals fabrication (growth) presented here, has the potential, after further development and optimization, to be integrated in an all-automated device fabrication process. An important aspect of chapter 4 is how simple materials that are sometimes overlooked, as the aluminum chloride salt, can be exploited to gain control over and manipulate complicated chemical processes. Moreover, this chapter is an example of how printing enables us precise control as an additive fabrication method.

In order for this work to be successfully integrated into the industry 4.0 vision, there are several additional challenges and limitations to overcome towards this goal. In order to upscale this work for industrial use, for nuclear plants, water purification facilities etc., there will be a need to significantly increase the dimensions of the printed MOF/Zeolite structures. Technology-wise, there is a growing effort in the industry to develop large-scale printers, and several such technologies are already available in the market. Materials-wise, we believe that the main challenge would be to maintain the control over the phase-separation, which is crucial in order to keep the availability and functionality of the embedded compounds in the printed polymeric structures.

In conclusion, we explored the printing as an additional toolbox for chemistry and materials research. We hope that this work will push forward the utilization of printing and additive manufacturing for this purpose, and will inspire others in the field of functional materials.





## 4. References

1. Bandyopadhyay A, Bose S, Das S. 3D Printing of Biomaterials. *Mrs Bulletin* **40**, 108-112 (2015).
2. Fisher T. Welcome to the Third Industrial Revolution The Mass-Customisation of Architecture, Practice and Education. *Architectural Design* **85**, 40-45 (2015).
3. Rayna T, Striukova L. From rapid prototyping to home fabrication: How 3D Printing is Changing Business Model Innovation. *Technological Forecasting and Social Change* **102**, 214-224 (2016).
4. Zein I, Hutmacher DW, Tan KC, Teoh SH. Fused Deposition Modeling of Novel Scaffold Architectures for Tissue Engineering Applications. *Biomaterials* **23**, 1169-1185 (2002).
5. Zhang MS, *et al.* Dual-Responsive Hydrogels for Direct-Write 3D Printing. *Macromolecules* **48**, 6482-6488 (2015).
6. Gardan J. Additive Manufacturing Technologies: State of the Art and Trends. *International Journal of Production Research* **54**, 3118-3132 (2016).
7. Tekin E, Smith PJ, Schubert US. Inkjet Printing as a Deposition and Patterning Tool for Polymers and Inorganic Particles. *Soft Matter* **4**, 703-713 (2008).
8. Grouchko M, Kamyshny A, Magdassi S. Formation of Air-Stable Copper-Silver Core-Shell Nanoparticles for Inkjet Printing. *Journal of Materials Chemistry* **19**, 3057-3062 (2009).
9. Davis ME. Ordered Porous Materials for Emerging Applications. *Nature* **417**, 813-821 (2002).
10. Dias JM, Alvim-Ferraz MCM, Almeida MF, Rivera-Utrilla J, Sanchez-Polo M. Waste Materials for Activated Carbon Preparation and Its Use in Aqueous-Phase Treatment: A review. *Journal of Environmental Management* **85**, 833-846 (2007).
11. Cheung O, Bacsik Z, Liu QL, Mace A, Hedin N. Adsorption Kinetics for CO<sub>2</sub> on Highly Selective Zeolites NaKA and Nano-NaKA. *Applied Energy* **112**, 1326-1336 (2013).
12. Jensen C, Buck D, Dilger H, Bauer M, Phillipp F, Roduner E. Maximum Hydrogen Chemisorption on KL Zeolite Supported Pt Clusters. *Chemical Communications* **49**, 588-590 (2013).
13. Qin JH, *et al.* Aqueous- and Vapor-Phase Detection of Nitroaromatic Explosives by a Water-Stable Fluorescent Microporous MOF Directed by an Ionic Liquid. *Journal of Materials Chemistry A* **3**, 12690-12697 (2015).

14. Yu Y, Zhang XM, Ma JP, Liu QK, Wang P, Dong YB. Cu(I)-MOF: Naked-Eye Colorimetric Sensor for Humidity and Formaldehyde in Single-Crystal-to-Single-Crystal Fashion. *Chemical Communications* **50**, 1444-1446 (2014).
15. Seo JS, *et al.* A Homochiral Metal-Organic Porous Material for Enantioselective Separation and Catalysis. *Nature* **404**, 982-986 (2000).
16. Zheng Y, Li X, Dutta PK. Exploitation of Unique Properties of Zeolites in the Development of Gas Sensors. *Sensors* **12**, 5170-5194 (2012).
17. Misaelides P. Application of Natural Zeolites in Environmental Remediation: A Short Review. *Microporous and Mesoporous Materials* **144**, 15-18 (2011).
18. Johnson EBG, Arshad SE. Hydrothermally Synthesized Zeolites Based on Kaolinite: A Review. *Applied Clay Science* **97-98**, 215-221 (2014).
19. Langmi HW, *et al.* Hydrogen Storage in Ion-Exchanged Zeolites. *Journal of Alloys and Compounds* **404**, 637-642 (2005).
20. Stakebake JL, Fritz J. Characterization of Natural Chabazite and 5A Synthetic Zeolites .2. Adsorption Properties and Porosity. *Journal of Colloid and Interface Science* **100**, 33-40 (1984).
21. Musyoka NM, Petrik LF, Hums E, Kuhnt A, Schwieger W. Thermal Stability Studies of Zeolites A and X Synthesized from South African Coal Fly Ash. *Research on Chemical Intermediates* **41**, 575-582 (2015).
22. Ghasemi Z, Sourinejad I, Kazemian H, Rohani S. Application of Zeolites in Aquaculture Industry: A Review. *Reviews in Aquaculture* **10**, 75-95 (2018).
23. Yilmaz B, Muller U. Catalytic Applications of Zeolites in Chemical Industry. *Topics in Catalysis* **52**, 888-895 (2009).
24. Vermeiren W, Gilson JP. Impact of Zeolites on the Petroleum and Petrochemical Industry. *Topics in Catalysis* **52**, 1131-1161 (2009).
25. Furukawa H, Cordova KE, O'Keeffe M, Yaghi OM. The Chemistry and Applications of Metal-Organic Frameworks. *Science* **341**, 974 (2013).
26. Farha OK, *et al.* Metal-Organic Framework Materials with Ultrahigh Surface Areas: Is the Sky the Limit? *Journal of the American Chemical Society* **134**, 15016-15021 (2012).

27. Li B, Wen HM, Zhou W, Chen BL. Porous Metal-Organic Frameworks for Gas Storage and Separation: What, How, and Why? *Journal of Physical Chemistry Letters* **5**, 3468-3479 (2014).
28. Chughtai AH, Ahmad N, Younus HA, Laypkov A, Verpoort F. Metal-Organic Frameworks: Versatile Heterogeneous Catalysts for Efficient Catalytic Organic Transformations. *Chemical Society Reviews* **44**, 6804-6849 (2015).
29. Chernikova V, Yassine O, Shekhah O, Eddaoudi M, Salama KN. Highly Sensitive and Selective SO<sub>2</sub> MOF Sensor: The Integration of MFM-300 MOF as a Sensitive Layer on a Capacitive Interdigitated Electrode. *Journal of Materials Chemistry A* **6**, 5550-5554 (2018).
30. Frameworks for commercial success. *Nature Chemistry* **8**, 987-987 (2016).
31. Faust T, Farha O, Hernandez B. MOFs Move to Market. *Nature Chemistry* **8**, 990-991 (2016).
32. Singh MP, Dhumal NR, Kim HJ, Kiefer J, Anderson JA. Influence of Water on the Chemistry and Structure of the Metal Organic Framework Cu<sub>3</sub>(btc)<sub>2</sub>. *Journal of Physical Chemistry C* **120**, 17323-17333 (2016).
33. Howarth AJ, *et al.* Chemical, Thermal and Mechanical Stabilities of Metal-Organic Frameworks. *Nature Reviews Materials* **1**, 15018 (2016).
34. Biradha K, Ramana A, Vittal JJ. Coordination Polymers Versus Metal-Organic Frameworks. *Crystal Growth & Design* **9**, 2969-2970 (2009).
35. Du PY, Gu W, Gao S, Liu X. A Bimodal 2D Silver Coordination Polymer: Turn-On Sensing of Cd-II and Sensitization of Lanthanide Ions. *Inorganic Chemistry Communications* **60**, 47-50 (2015).
36. *Hybrid Organic-Inorganic Interfaces: Towards Advanced Functional Materials*. John Wiley and Sons (2017).
37. Benmansour S, Gomez-Garcia CJ. A Heterobimetallic Anionic 3,6-Connected 2D Coordination Polymer Based on Nitranilate as Ligand. *Polymers* **8**, (2016).
38. Jiang H, *et al.* Atomically Flat, Large-Sized, Two-Dimensional Organic Nanocrystals. *Small* **9**, 990-995 (2013).
39. Zeis R, Siegrist T, Kloc C. Single-Crystal Field-Effect Transistors Based on Copper Phthalocyanine. *Applied Physics Letters* **86**, 022103 (2005).

40. Coropceanu V, Cornil J, da Silva Filho DA, Olivier Y, Silbey R, Bredas J-L. Charge Transport in Organic Semiconductors. *Chemical Reviews* **107**, 926-952 (2007).
41. Kang B, Lee WH, Cho K. Recent Advances in Organic Transistor Printing Processes. *Acs Applied Materials & Interfaces* **5**, 2302-2315 (2013).
42. Dong G, Li H, Chen V. Challenges and Opportunities for Mixed-Matrix Membranes for Gas Separation. *Journal of Materials Chemistry A* **1**, 4610-4630 (2013).
43. Friebe S, Diestel L, Knebel A, Wollbrink A, Caro J. MOF-Based Mixed-Matrix Membranes in Gas Separation - Mystery and Reality. *Chemie Ingenieur Technik* **88**, 1788-1797 (2016).
44. Sun DT, Gasilova N, Yang S, Oveisi E, Queen WL. Rapid, Selective Extraction of Trace Amounts of Gold from Complex Water Mixtures with a Metal-Organic Framework (MOF)/Polymer Composite. *Journal of the American Chemical Society* **140**, 16697-16703 (2018).
45. Ge L, Zhou W, Rudolph V, Zhu Z. Mixed Matrix Membranes Incorporated with Size-Reduced Cu-BTC for Improved Gas Separation. *Journal of Materials Chemistry A* **1**, 6350-6358 (2013).
46. Bastani D, Esmaeili N, Asadollahi M. Polymeric Mixed Matrix Membranes Containing Zeolites as a Filler for Gas Separation Applications: A Review. *Journal of Industrial and Engineering Chemistry* **19**, 375-393 (2013).
47. Zhang Y, Feng X, Yuan S, Zhou J, Wang B. Challenges and Recent Advances in MOF-Polymer Composite Membranes for Gas Separation. *Inorganic Chemistry Frontiers* **3**, 896-909 (2016).
48. Lirio S, Liu W-L, Lin C-L, Lin C-H, Huang H-Y. Aluminum Based Metal-Organic Framework-Polymer Monolith in Solid-Phase Microextraction of Penicillins in River Water and Milk Samples. *Journal of Chromatography A* **1428**, 236-245 (2016).
49. Zhang YL, *et al.* Fabrication of Porous Zeolite/Chitosan Monoliths and Their Applications for Drug Release and Metal Ions Adsorption. *Carbohydrate Polymers* **117**, 657-665 (2015).
50. Jin P, *et al.* Hierarchically Porous MOF/Polymer Composites via Interfacial Nanoassembly and Emulsion Polymerization. *Journal of Materials Chemistry A* **6**, 20473-20479 (2018).
51. Fu QS, *et al.* Preparation of Ice-Templated MOF-Polymer Composite Monoliths and Their Application for Wastewater Treatment with High Capacity and Easy Recycling. *Acs Applied Materials & Interfaces* **9**, 33979-33988 (2017).

52. Viklund C, Svec F, Frechet JMJ, Irgum K. Monolithic, "Molded", Porous Materials with High Flow Characteristics for Separations, Catalysis, or Solid-Phase Chemistry: Control of Porous Properties During Polymerization. *Chemistry of Materials* **8**, 744-750 (1996).
53. Li YY, Tolley HD, Lee ML. Monoliths from Poly(ethylene glycol) Diacrylate and Dimethacrylate for Capillary Hydrophobic Interaction Chromatography of Proteins. *Journal of Chromatography A* **1217**, 4934-4945 (2010).
54. Santora BP, Gagne MR, Moloy KG, Radu NS. Porogen and Cross-Linking Effects on the Surface Area, Pore Volume Distribution, and Morphology of Macroporous Polymers Obtained by Bulk Polymerization. *Macromolecules* **34**, 658-661 (2001).
55. Tsurumi J, *et al.* Solution-Processed Single-Crystalline Organic Transistors on Patterned Ultrathin Gate Insulators. *Organic Electronics* **15**, 1184-1188 (2014).
56. Dong HL, Fu XL, Liu J, Wang ZR, Hu WP. 25th Anniversary Article: Key Points for High-Mobility Organic Field-Effect Transistors. *Advanced Materials* **25**, 6158-6182 (2013).
57. Jiang H, Kloc C. Single-Crystal Growth of Organic Semiconductors. *Mrs Bulletin* **38**, 28-33 (2013).
58. Schweicher G, Olivier Y, Lemaury V, Geerts YH. What Currently Limits Charge Carrier Mobility in Crystals of Molecular Semiconductors? *Israel Journal of Chemistry* **54**, 595-620 (2014).
59. Minemawari H, *et al.* Inkjet Printing of Single-Crystal Films. *Nature* **475**, 364-367 (2011).
60. Minas C, Carnelli D, Tervoort E, Studart AR. 3D Printing of Emulsions and Foams into Hierarchical Porous Ceramics. *Advanced Materials* **28**, 9993-9999 (2016).
61. Li HJ, Tan C, Li L. Review of 3D Printable Hydrogels and Constructs. *Materials & Design* **159**, 20-38 (2018).
62. Kajiyama S, Kikkawa J, Hoshino J, Okubo M, Hosono E. Assembly of Na<sub>3</sub>V<sub>2</sub>(PO<sub>4</sub>)<sub>3</sub> Nanoparticles Confined in a One-Dimensional Carbon Sheath for Enhanced Sodium-Ion Cathode Properties. *Chemistry-a European Journal* **20**, 12636-12640 (2014).
63. Liu HN, Webster TJ. Enhanced Biological and Mechanical Properties of Well-Dispersed Nanophase Ceramics in Polymer Composites: From 2D to 3D Printed Structures. *Materials Science & Engineering C-Materials for Biological Applications* **31**, 77-89 (2011).
64. Li TT, Wang LF. Bending Behavior of Sandwich Composite Structures with Tunable 3D-Printed Core Materials. *Composite Structures* **175**, 46-57 (2017).

65. Layani M, Cooperstein I, Magdassi S. UV Crosslinkable Emulsions with Silver Nanoparticles for Inkjet Printing of Conductive 3D Structures. *Journal of Materials Chemistry C* **1**, 3244-3249 (2013).
66. Halevi O, Tan JMR, Lee PS, Magdassi S. Hydrolytically Stable MOF in 3D-Printed Structures. *Advanced Sustainable Systems* **2**, 1700150 (2018).
67. Halevi O, Chen TY, Lee PS, Magdassi S, Hriljac JA. Nuclear wastewater decontamination by 3D-Printed hierarchical zeolite monoliths. *RSC Advances* **10**, 5766 (2020).
68. Halevi O, Jiang H, Kloc C, Magdassi S. Additive Manufacturing of Micrometric Crystallization Vessels and Single Crystals. *Scientific Reports* **6**, 36786 (2016).
69. Maldonado N, *et al.* 3D Printing of a Thermo- and Solvatochromic Composite Material Based on a Cu(II)-Thymine Coordination Polymer with Moisture Sensing Capabilities. *Advanced Functional Materials* **29**, 1808424 (2019).

## **5. Appendices**





### **5.1. Appendix I - 3D Printing of Thermo- and Solvatochromic Composite Material Based on a Cu(II)-Thymine Coordination Polymer with Moisture Sensing Capabilities**

Published<sup>69</sup>: Maldonado N., Vegas V.G., Halevi O., Martinez J.I., Lee. P.S., Magdassi S., Wharmby M.T., Platero-Prats A.E., Moreno C., Zamora F., Amo-Ochoa P. 3D Printing of Thermo- and Solvatochromic Composite Material Based on a Cu(II)-Thymine Coordination Polymer with Moisture Sensing Capabilities. *Advanced Functional Materials* **29**, 1808424 (2019).



# 3D Printing of a Thermo- and Solvatochromic Composite Material Based on a Cu(II)–Thymine Coordination Polymer with Moisture Sensing Capabilities

Noelia Maldonado, Verónica G. Vegas, Oded Halevi, Jose Ignacio Martínez, Pooi See Lee, Shlomo Magdassi, Michael T. Wharmby, Ana E. Platero-Prats, Consuelo Moreno, Félix Zamora,\* and Pilar Amo-Ochoa\*

*This paper is dedicated to Esteban and Miguel Zamora-Amo*

This work presents the fabrication of 3D-printed composite objects based on copper(II) 1D coordination polymer (CP1) decorated with thymine along its chains with potential utility as an environmental humidity sensor and as a water sensor in organic solvents. This new composite object has a remarkable sensitivity, ranging from 0.3% to 4% of water in organic solvents. The sensing capacity is related to the structural transformation due to the loss of water molecules that CP1 undergoes with temperature or by solvent molecules' competition, which induces significant change in color simultaneously. The CP1 and 3D printed materials are stable in air over 1 year and also at biological pHs (5–7), therefore suggesting potential applications as robust colorimetric sensors. These results open the door to generate a family of new 3D printed materials based on the integration of multifunctional coordination polymers with organic polymers.

materials for 3D printing are necessary.<sup>[2]</sup> Indeed, materials that are feasible for 3D printing are rather limited; the classical organic polymers with good processability capabilities such as nylon, polypropylene, or polycarbonate are among the most popular ones.<sup>[3]</sup> While these organic polymers show excellent mechanical and thermal properties, as well as suitable processability under printing conditions, they typically lack functionalities (e.g., electrical/thermal conductivity, luminescence, magnetism, self-healing, etc.) required for various potential applications. Therefore, either the discovery of new functional materials for 3D printing or the integration of known functional materials with printable organic polymers to form

suitable functional composites<sup>[4]</sup> is a subject of high research and technological interest.<sup>[5]</sup>

In this field, coordination polymers (CPs) are well-developed multifunctional materials that are based on the assembly of two building blocks, metal entity and organic

## 1. Introduction

3D printing is an emerging technology that is expected to bring an industrial revolution in goods manufacturing.<sup>[1]</sup> However, in order to realize these expectations, new functional

N. Maldonado, V. G. Vegas, Dr. A. E. Platero-Prats, Dr. C. Moreno, Dr. F. Zamora, Dr. P. Amo-Ochoa  
Departamento de Química Inorgánica  
Universidad Autónoma de Madrid  
28049 Madrid, Spain  
E-mail: felix.zamora@uam.es; pilar.amo@uam.es

O. Halevi, Prof. P. S. Lee, Prof. S. Magdassi  
Casali Center for Applied Chemistry  
Institute of Chemistry  
The Hebrew University of Jerusalem  
91904 Jerusalem, Israel

O. Halevi, Prof. P. S. Lee, Prof. S. Magdassi  
School of Materials Science and Engineering  
Nanyang Technological University  
Singapore 639798, Singapore


O. Halevi, Prof. P. S. Lee, Prof. S. Magdassi  
CREATE NTU-HUJ Programme Enterprise Wing  
Singapore 138602, Singapore

Dr. J. I. Martínez  
Departamento de Nanoestructuras  
Superficies  
Recubrimientos y Astrofísica Molecular  
Instituto de Ciencia de Materiales de Madrid (ICMM-CSIC)  
28049 Madrid, Spain

Dr. M. T. Wharmby  
Deutsches Elektronen-Synchrotron (DESY)  
Notkestraße 85, 22607 Hamburg, Germany

Dr. F. Zamora, Dr. P. Amo-Ochoa  
Institute for Advanced Research in Chemical Sciences (IAdChem)  
Universidad Autónoma de Madrid  
28049 Madrid, Spain

Dr. F. Zamora  
Condensed Matter Physics Center (IFIMAC)  
Universidad Autónoma de Madrid  
28049 Madrid, Spain

 The ORCID identification number(s) for the author(s) of this article can be found under <https://doi.org/10.1002/adfm.201808424>.

DOI: 10.1002/adfm.201808424

ligands, which define both the molecular architecture and properties of the final material. CP nanostructuring is a relatively new subject, which enables new uses for CPs but also their integration with other materials to produce a new family of (nano)composites. Indeed, very recently, the potential of nanolayers and nanofibers of CPs to form multifunctional ultrathin films was demonstrated.<sup>[6]</sup> However, despite the high potential for the use of CPs and their porous forms, metal–organic frameworks (MOFs), their use to form new functional materials suitable for 3D printing is limited to just a few examples based on dynamic coordination bonds<sup>[7]</sup> and embedding of MOFs within organic and inorganic matrices.<sup>[5b,8]</sup>

Currently, the interest in recognition, quantification, and monitoring of important daily-life chemical species is increasing in different fields such as health, food quality control, and environmental protection, among others. Inexpensive in situ fast detection on-site sensors that respond in a simple and rapid fashion are highly desired. Therefore, it is of current research interest to develop simple and robust sensors with on-site features and to further improve the sensing performance regardless of environmental fluctuations.<sup>[9]</sup> A commonly accepted principle for the design of chemosensors is that they must be able to detect substances and produce an easily measurable response, such as a change of color, fluorescence, or any other macroscopic property.<sup>[10]</sup> CPs are excellent candidates for this purpose due to their structural flexibility and dynamic structures, as well as their capability to generate stimuli-responsive materials.<sup>[11,12]</sup>

In this work, we have fabricated water sensors by printing photopolymerization 3D objects. The printed 3D objects contain embedded nanofibers of the nontoxic,<sup>[13]</sup> thermo- and solvatochromic copper(II) 1D coordination polymer grafted with thymine (TAcOH) as a terminal ligand and 4,4'-bipyridine (4,4'-bipy) as a bridging ligand between the metal centers (CP1). This structure includes a coordinated water molecule and two solvation water molecules (Figure 1). These water molecules are easily released upon soft heating or moderate vacuum to produce new related CPs. This is a reversible process that recovers the initial state by the exposure of the materials to water. The water

release produces a significant color change in the CP from blue to violet (Figure 2) that enables using this compound as a robust moisture humidity sensor<sup>[14]</sup> in both air and organic solvents, such as methanol (MeOH), ethanol (EtOH), acetonitrile (ACN, CH<sub>3</sub>CN), and tetrahydrofuran (THF). In fact, the present non-porous CP is a rare example showing such sensing capability.<sup>[15]</sup> In addition, by forming dispersions of CP1 within photopolymerizable monomers, and a solvent, we have been able to 3D-print different stable composite architectures using a digital light processing (DLP) 3D printer (Scheme S1b, Supporting Information) or an extruding 3D printer (Scheme S1a, Supporting Information). Furthermore, we have shown the ability of these printed materials to detect moisture in air and solvents.

## 2. Results and Discussion

The direct reaction between Cu(NO<sub>3</sub>)<sub>2</sub> with 4,4'-bipy and TAcOH in water at room temperature leads to the formation of a colloid based on nanofibers of [Cu(TAcO)<sub>2</sub>(4,4'-bipy)(H<sub>2</sub>O)]<sub>n</sub> · 2H<sub>2</sub>O (CP1).<sup>[13]</sup> The thermal stability of CP1 powder has been investigated by differential scanning calorimetry (DSC) and thermogravimetric analysis (TGA) coupled to mass spectroscopy<sup>[16]</sup> under O<sub>2</sub> (Figures S1 and S2, Supporting Information). Its thermal study shows a first step at 60 °C, indicative of the loss of one water molecule, and a second step at 135 °C, indicative of the loss of two water molecules (Figure S1, Supporting Information). The heating of CP1 powder at 60 °C (30 min) results in a significant reversible color change from blue to violet, due to formation of the intermediate material (named CP1-H<sub>2</sub>O, Figure 2, middle; diffuse reflectance spectra, Figure S6a,b and Table S1, Supporting Information) suggesting that the water molecule lost in the first step could be the one coordinated to copper. This is a reversible step since cooling CP1-H<sub>2</sub>O in air, the color changes from violet to blue, indicating the change to CP1. To demonstrate the stability and reproducibility of this process, more than 20 heating cycles at 60 °C and air cooling of CP1 have been performed (Figure S7,

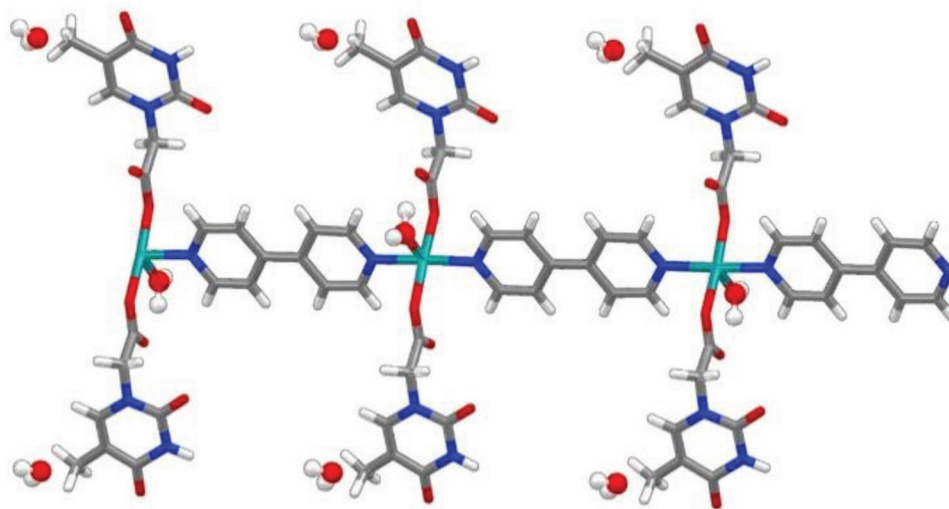


**Figure 1.** View of a chain of [Cu(TAcO)<sub>2</sub>(H<sub>2</sub>O)(4,4'-bipy)]<sub>n</sub> · 2H<sub>2</sub>O. Oxygen atoms are in red, copper atoms are in green, nitrogen atoms are in blue, carbon atoms are in gray, and hydrogen atoms are in white.

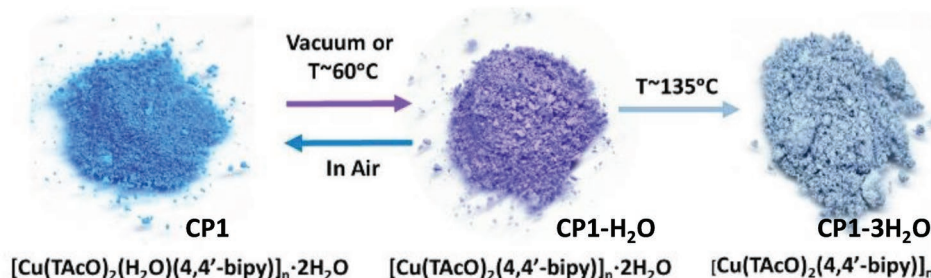


**Figure 2.** Photographs of the corresponding powders in the transformation process mediated by either temperature or vacuum from **CP1** to **CP1-H<sub>2</sub>O** and from **CP1-H<sub>2</sub>O** to **CP1-3H<sub>2</sub>O**.

Supporting Information). Increasing temperature up to 135 °C for 30 min, an irreversible color change from violet, **CP1-H<sub>2</sub>O**, to grayish blue is also observed, **CP1-3H<sub>2</sub>O** (Figure 2, right).

The thermochromism of **CP1** is a reversible process at 60 °C, probably due to the dissociation of the weakly bonded water molecule from the coordination sphere, which facilitates a simple structural reorganization. In principle, the release of a water molecule coordinated to a metal center seems to be more energetically unfavorable than solvated water molecules; however, this process is supported by X-ray powder diffraction data (Figure 3, green line; Figures S3–S5, Supporting Information) and theoretical modeling (see below and Figures S8–S10 in the Supporting Information). Thus, the reversible process of water incorporation into **CP1-H<sub>2</sub>O** implies the coordination of a water molecule back to the copper sphere, regenerating the initial structure **CP1**, upon exposure of **CP1-H<sub>2</sub>O** to the moisture of the atmosphere (**CP1-H<sub>2</sub>O** under argon does not change to **CP1**). The structural changes in **CP1** seem to be dramatic and irreversible at 135 °C, according to the total loss of the water molecules present in the structure. This agrees with a much pronounced structural change, as is observed in the powder X-ray diffraction data (Figure 3; Figures S3 and S5, Supporting Information) and theoretical modeling (see below

and Figures S8–S10 in the Supporting Information). We have also studied the behavior of **CP1** at 25 °C in vacuum from 1 h to 4 days, observing a similar color change from blue to violet after 1 h, and to grayish blue after 4 days in vacuum. X-ray powder data were collected for **CP1** at 25 °C in vacuum after 1 h and after 4 days, as well as after heating at 60 and 135 °C for 30 min. Each diffractogram confirmed the structural changes (Figure 3; Figures S3–S5, Supporting Information).

## 2.1. Computational Studies

In order to understand the obtained experimental data (TGA and the color changes) from the theoretical point of view, we have carried out a density functional theory (DFT)-based calculation to compute the transition-state energy barrier for the release of the coordinated water molecule from the structure of the **CP1** (with all the coordinated and solvation water molecules). For that purpose, we have made use of the climbing-image nudged elastic band (CI-NEB) approach to get a converged minimum energy path (MEP) taking as first step the optimized all-water-molecules **CP1** geometry and an optimized final state with the coordination water molecule removed from the structure, with a total number of intermediate image states of 20, which were free to relax along the procedure. This calculation yields a transition-state barrier of  $\Delta E = 0.63$  eV (Figure 4). On the other hand, the rate for this process has been computed by looking at normal modes possessing amplitudes that make the coordinated water molecule detach from the structure. The rate is then obtained by multiplying the Boltzmann factor (providing the probability to pick up a thermal fluctuation at temperature  $T$  to overcome the barrier after “fluctuation”,  $\Delta E$ ) and the number of attempts to pass the barrier given by the frequency of the relevant mode: in this case of around  $450\text{ cm}^{-1}$ ,  $\Gamma = e^{-[\Delta E/(k_B T)]}$ . In the present case, the values obtained, according to the Boltzmann statistics, are consistent with the loss of the coordination water molecule at 60 °C within minutes, as observed experimentally. In line with the previous data, each solvation water is bound within the system with energy of 1.16 eV. This value is calculated by a difference of total energies between the system with solvation waters, the system without solvation waters, and  $n$  times the energy of the water molecules, present in the unit cell. Therefore, to remove the solvation waters, a thermal energy exceeding this cohesion enthalpy is necessary, 1.16 eV per molecule. This can also help to justify the greatest difficulty in losing the solvation water versus the coordination water.

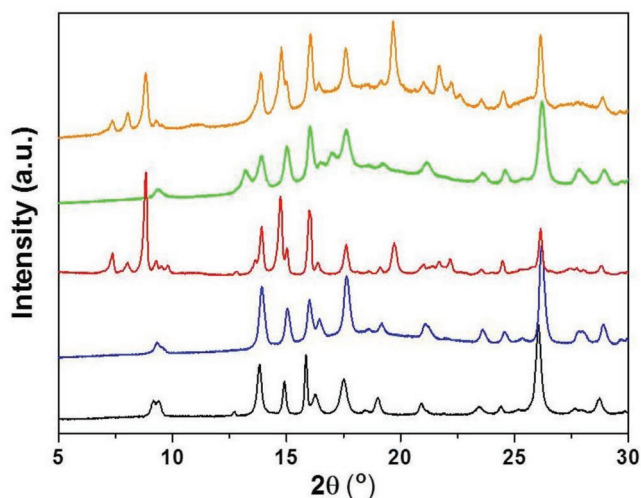


**Figure 3.** X-ray powder diffraction patterns of **CP1** as bulk powder under ambient conditions (black line), **CP1** after 1 h under vacuum (blue line), **CP1** after 4 days under vacuum (red line), **CP1** after heating in argon atmosphere at 60 °C for 30 min (green line), and **CP1** after heating at 135 °C for 30 min (orange line).

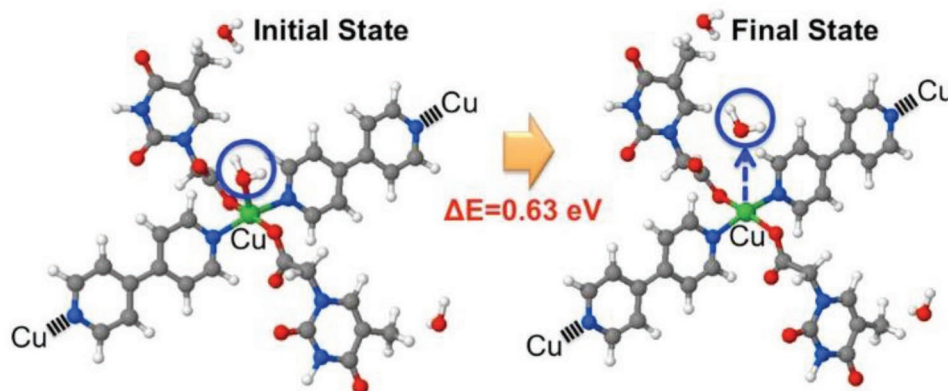


**Figure 4.** Optimized initial and final states for the computation of the transition-state energy barrier for the release of the coordinated water molecule from the CP1 structure within the CI-NEB approach.

## 2.2. Pair Distribution Function Studies

In addition, to probe the atomic structure of CP1 after heat treatments and to explore the local structural implications linked to dehydration, we have applied pair distribution function (PDF) analysis based on synchrotron X-ray total scattering data. PDF experiments were carried out on both CP1 and CP1-H<sub>2</sub>O samples.

The PDFs for the CP1 systems are dominated by atom–atom correlations involving the strongly scattering Cu atoms (Figure 5). The main PDF contribution is observed at  $\approx 2.0$  Å, which contains correlations from overlapping Cu–N and Cu–O distances associated with the binding 4,4'-bipy and TAcO ligands, respectively. PDF data collected on CP1-H<sub>2</sub>O did not show any significant change in the peak at  $\approx 2.0$  Å,

demonstrating that the coordination mode of the ligands to copper remains unaltered during this process.

Interestingly, PDF data collected on the CP1-H<sub>2</sub>O sample heated at 60 °C showed a subtle decrease in intensity of the PDF peak at  $\approx 2.3$  Å compared to the pristine system. This bond distance is associated with the water molecule bound to the copper as well as carbon–carbon correlations within the ligands. Quantitative analyses of this PDF peak suggested the loss of the Cu–O bonds linked to the dehydration of the copper centers, in agreement with TGA and theoretical calculation data. This result would suggest a change of coordination number from 5 to 4 after the heat treatment, which explains the color change experimentally observed.<sup>[14]</sup> Despite the structural transitions, the powder diffraction shows no substantial changes (Figure 3, green line).<sup>[17]</sup> After heating at 135 °C, the local structure of CP1 remains unaltered while major changes are observed at long-range scale. This is also in agreement with the structural transition determined by X-ray powder diffraction analyses (Figure 3; Figure S5, Supporting Information).

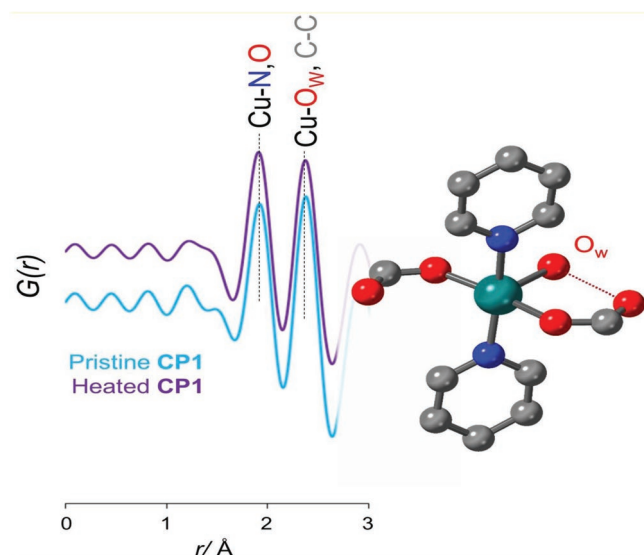


**Figure 5.** Experimental PDFs for CP1 (pristine) and CP1-H<sub>2</sub>O (heated) samples before and after heating at 60 °C, indicating the two peaks linked to the binding of the 4,4'-bipy and TAcO ligands ( $\approx 2.0$  Å) and the water molecule ( $\approx 2.3$  Å). The dash line in the structure indicates hydrogen bonding between the water molecule and one oxygen atom of the TAcO ligands.

## 2.3. First-Principles Calculations

Moreover, in order to investigate the structural and electronic evolution of the CP1 induced by the sequential loss of the coordinated and solvation water molecules with increasing temperature, we have carried out a series of first-principles calculations. As a starting point, we have taken the geometry and lattice as obtained from the low-temperature powder X-ray diffraction experiment, where CP1 has a water molecule coordinated to the Cu atom and two solvation water molecules in the vicinity of the terminal –CH<sub>3</sub> groups of the ligands (Figure 1). Once the structure with all the water molecules is relaxed, the resulting structure does not show substantial changes (Figures S9 and S10, Supporting Information), which indicates the confident performance of our theoretical approach. In a next threefold step, we have removed from the resulting structure i) the coordination water molecule, ii) the two solvation water molecules, and iii) the coordination and solvation water molecules simultaneously. All three geometries (i, ii, and iii) were again fully relaxed (Figures S9 and S10, Supporting Information) in order to



compare changes with the all-water-molecules case. Consistently with the experimental evidence, the changes in the structure are not very pronounced for optimized cases (i) and (ii), where the most noticeable changes are observed in the Cu–N and Cu–O distances decreasing <4% for structure (i), and a slight torsion of the  $-\text{CH}_3$  terminating groups in the ligands <4°. However, for case (iii), where all the water molecules have been removed before optimizing the structure, the Cu–N and Cu–O distances decrease by around 6% and a rotation of around 8° of the 4,4'-bipyridine units forming the chains is observed.

We have already performed a comparison between the experimental diffractogram for the CP1 and the simulated power X-ray diffractograms from the DFT-optimized structures with all water molecules, no solvation water molecules, no coordination water molecule, and any water molecules (Figure S10, Supporting Information). Interestingly, the slight geometrical changes observed in all the optimized structures seem not to be sufficiently pronounced to have a clear influence on their correspondingly simulated powder X-ray diffractograms (Figure S10, Supporting Information). This finding seems to be consistent with the experimental observations (Figure 3), where the structure of the compounds remains almost locally unaltered, not much affecting the diffractogram profile. On the other hand, major structural changes are experimentally observed at long-range scale, which, unfortunately, cannot be captured by our theoretical studies. This behavior also agrees with the previous related literature reporting on similar systems.<sup>[17]</sup>

For the sake of completeness, we have carried out an exhaustive analysis of the computed density of states (DOS) of the different models that we propose in this study (Figure S9, Supporting Information). Figure 6a shows the computed total density of electronic states (in arbitrary units) as a function of the energy referenced to the Fermi energy (in eV) for the CP1 compound: i) with all the coordinated and solvation water molecules, ii) just with the two solvation water molecules, iii) just with the coordination water molecules, and iv) with no water molecules. In a first inspection of this figure, we can appreciate that the morphological computed DOS profile of the different systems is essentially very similar.

On the other hand, Figure 6c shows the computed density of electronic states for case (i) of Figure 6a projected onto the solvation water molecules, the coordination water molecules, the Cu atoms, the full ligand, and the full structural chain (Cu atom + 4,4'-bipyridine units). From this figure, the most important information one can extract is the origin and location of the electronic states involved in the first permitted optical transition lying within the visible range, corresponding to the Cu atoms at the Fermi level and the first unoccupied state belonging to the ligands, located at around 2.8 eV above the Fermi level. In order to locate and identify these states in the total density of states, Figure 6b shows the same DOS profiles as in cases (i)–(iv) of Figure 6a magnified in a reduced energy window between –2 and 6 eV. In this figure, it is possible to identify the low-lying optical transitions between the aforementioned states. The energy difference between these states for case (i) is around 2.7 eV (with all the coordinated and solvation water molecules), while this energy is slightly higher for case (ii) of around 2.9 eV (just with the solvation water molecules

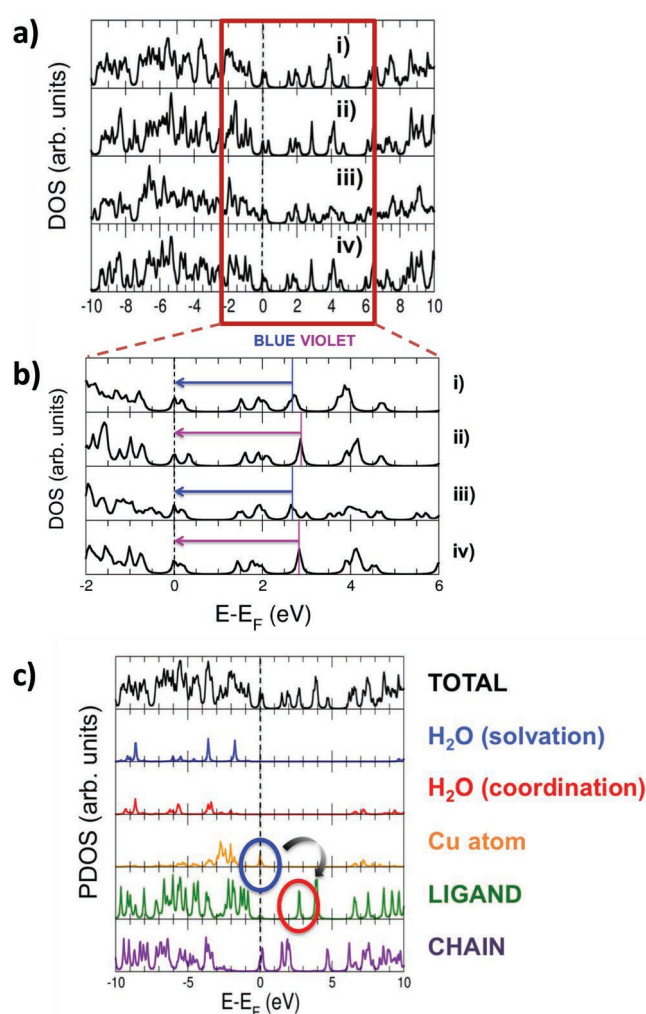


**Figure 6.** a) Computed total density of electronic states (in arbitrary units) as a function of the energy referenced to the Fermi energy (in eV) for the CP1 compound: i) with all the coordinated and solvation water molecules, ii) just with the two solvation water molecules, iii) just with the coordination water molecules, and iv) with no water molecules. b) DOS profiles of panels (i)–(iv) of part (a) shown in a reduced energy window between –2 and 6 eV; low-lying optical transitions are indicated in blue and violet colors according to their corresponding energy. c) Computed density of electronic states for case (i) of part (a) projected onto the solvation water molecules, the coordination water molecules, the Cu atoms, the full ligand, and the full structural chain (Cu atom + 4,4'-bipyridine units); the two electronic states involved in the first permitted optical transition lying within the visible range (Cu atom → ligands) are highlighted by colored ovals.

and the coordinated water molecules removed). This could also justify the experimental observation that the first type of water molecules lost by the CP1, corresponding to the coordinated ones, induce a color change from blue to violet (increasing the photon energy). This is also reinforced by the fact that the energy between both states for case (iii) (just with coordinated water molecules) is equal to that for case (i) with no significant variation in the transition energy. On the other hand, the system at a higher temperature, when all the water molecules are gone, has a violet gray color. This behavior is also observed



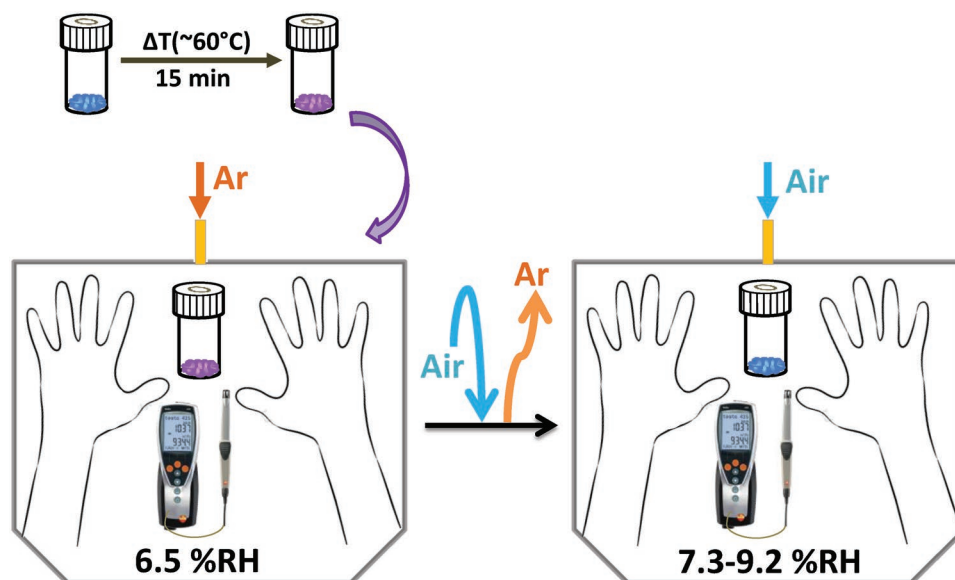


**Figure 7.** Outline of the experiment carried out in a dry box at 25 °C to detect the capacity of the **CP1-H<sub>2</sub>O** as a sensor of relative humidity of the air.

in the DOS profile for case (iv) of Figure 6b, yielding the same transition energy between these two states as for case (ii) (of around 2.9 eV). The fact that the energy difference between both specific states is very close to those corresponding to the blue and violet photon energies can be seen here just as a mere anecdote, since the values obtained from conventional DFT must be taken cautiously (conventional DFT underestimates gaps, and within our theory level we are missing excitonic effects). Nonetheless, we can trust the relative positioning of the levels, which in this case agrees with the experimental evidence.

## 2.4. Humidity Sensor

The determination of low quantities of water in organic solvents or in the atmosphere is of importance for numerous industrial and scientific applications.<sup>[12]</sup> The most common analytical procedure for water detection in solvents is the Karl Fischer titration. This method has some disadvantages such as the requirement for special equipment, complicated sample manipulations, and trained lab staff.<sup>[18]</sup> Therefore, visual sensing devices with low detection limits and sensitivities similar to those provided by the Karl Fischer titration are a reasonable alternative for humidity detection in solvents. There have been some studies on composite materials,<sup>[19]</sup> electrolytes, polymers,<sup>[20]</sup> and fluorescent materials<sup>[21]</sup> that have been utilized to detect low amounts of water in solvents.<sup>[22]</sup> However, there are just few examples of porous coordination polymers (MOFs)<sup>[11b,12,23]</sup> and almost none that we know based on nonporous coordination polymers.

In order to study the atmospheric relative humidity (RH) detection capacity of dehydrated violet **CP1-H<sub>2</sub>O**, the sample was placed in a dry box under an argon atmosphere and exposed to controlled relative humidity ranging from 6.5% RH (relative humidity inside the dry box at 25 °C) to a gradually

increased 9.2% RH. A change in color from violet to blue was observed at 7% RH due to rehydration of **CP1-H<sub>2</sub>O** to **CP1** (Figure 7).

### 2.4.1. Water Detection Limit of **CP1** and **CP1-H<sub>2</sub>O** in Dry Organic Solvents

We have studied the detection capacity of **CP1** and **CP1-H<sub>2</sub>O** materials under wet conditions. For these experiments, we have soaked both **CP1** and **CP1-H<sub>2</sub>O** in a variety of dry organic solvents to test the changes in color at room temperature and under atmospheric conditions. In these experiments, EtOH (99.5%), MeOH (99.9%), CH<sub>3</sub>CN (99.8%), and THF (99.9%) (Figure 8) were tested. In all cases, the changes are reversible and take few minutes (from 1 to 15 min).

Thus, when **CP1** is soaked in dry MeOH or EtOH, the material immediately changes its color from blue to violet (1 min) (diffuse reflectance spectra, Figure S6c,d and Table S1, Supporting Information). Once the organic solvent is removed, just upon allowing it to evaporate in air, the RH of the ambient ( $\approx 20\%$ ) is able to interchange the solvent molecules and turn it back to the blue **CP1** in less than 2 min. We assume that soaking **CP1** in MeOH produces a ligand exchange between the copper-coordinated water molecule and the MeOH that is reversed in the presence of water molecules of the ambient to **CP1**. This reversible process has also been tested using EtOH, THF, and ACN with similar results (Figure 8).

In order to confirm the ligand exchange in **CP1** after soaking in dry organic solvents, we have confirmed that after immersion of **CP1** for 2 min in EtOH at 25 °C the color changes from blue to violet and the X-ray powder diffractogram also changes significantly (Figure 9).

The solvatochromism property of the **CP1** may be due to the dissociation of the weakly bonded water molecule from

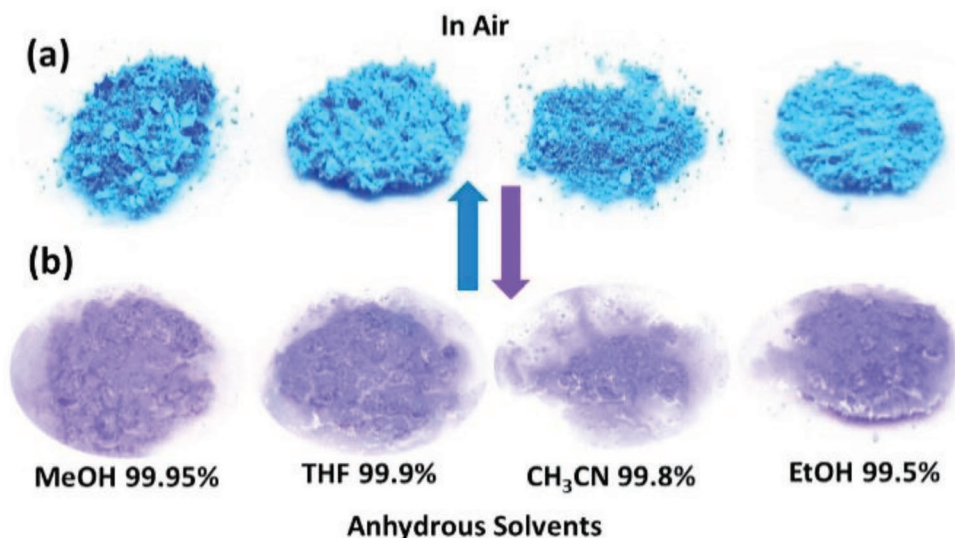


**Figure 8.** Photographs of a) CP1 in air and b) CP1 after soaking for 1–5 min in different dry organic solvents.

the coordination sphere, which facilitates the approach of the solvent molecules above and below the plane to the copper(II) center.<sup>[24]</sup> This is corroborated by conducting the experiment in dry organic solvents starting from the violet CP1-H<sub>2</sub>O, obtaining similar results (Table 1).

To study the capacity of water detection in dry organic solvents of CP1 and CP1-H<sub>2</sub>O, the bulk materials were exposed to different organic almost dry solvents, ethanol 99.5%, methanol 99.95%, tetrahydrofuran 99.9%, and acetonitrile 99.8%. All the experiments were carried out at room temperature. A well-known volume of solvent was added over an amount of the coordination polymer. In case of CP1, when the compound changed its color to violet, water was added in small volumes ( $\approx 5 \mu\text{L}$ ) until the coordination polymer changed to blue again. Finally, the limit of detection (LOD) was calculated in

percentage (Table 1). In case of CP1-H<sub>2</sub>O, which starts as a violet material, we did not observe any initial color change and after 30 min water was added in small volumes until the coordination polymer changed to blue again. The results show that CP1 is more sensitive to water than CP1-H<sub>2</sub>O.

## 2.5. 3D Printing of Compound CP1

For practical applications of CP1, 3D printing techniques have been utilized to form a variety of architectures (Figure 10). In order to form a 3D printable ink, while taking into account the low toxicity of CP1 toward cells<sup>[13]</sup> and its stability at physiological pH, considering the idea that it can also be applied in biologically related devices, CP1 was dispersed within a biodegradable monomer, dipropylene glycol diacrylate (DPGDA, SR-508). In addition to SR-508, another monomer, ethoxylated trimethylolpropane triacrylate (SR-9035), a solvent, diethylene glycol methyl ether (DM), and photoinitiators (Irgacure 819 and 184) were added to form the stable polymerizable 3D printable ink. By utilizing 3D printing to embed the CP1 powder within a matrix (CP1@3D), it is easier to handle, while the mechanical properties of the printed object can be tailored according to the chosen monomers. Two formulations were composed to give CP1@3D structures with 10 and 40 wt% of CP1. These were 3D printed using a DLP printer and an extruding printer, respectively. The extruding printer was used for the 40 wt% formulation due to the high viscosity of the ink that did not enable its printing via DLP. The samples were printed in different shapes (Figure 10a–c) with a maximum level of resolution of 200  $\mu\text{m}$ , achieved with the DLP printer. The printed composites were characterized by X-ray powder diffraction (Figure S11, Supporting Information) and scanning electron microscopy (SEM) (Figure 10d–f). The 3D printed objects contain the nano- and submicrometric fibers of the starting polymer (CP1), distributed homogeneously within the polymeric matrix (Figure 10d–f).

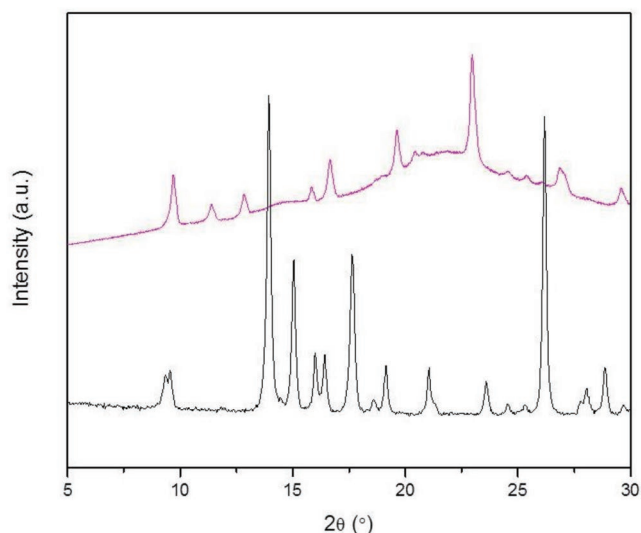


**Figure 9.** X-ray powder diffraction patterns of CP1 at 25 °C (black line) and the same compound after soaking in dry EtOH (violet line).

**Table 1.** Data obtained from the water detection limits of **CP1** and 3D printed material (**CP1@3D**) in the presence of different dry solvents.

Solvent	Solvent aliquot [mL]	<b>CP1</b> weight [g]	Water volume added [mL]	<b>CP1</b> LOD (%)	<b>CP1@3D</b> weight [g]	Water volume added [mL]	<b>CP1@3D</b> LOD [%]	<b>CP1-H<sub>2</sub>O</b> weight [g]	Water volume added [mL]	<b>CP1-H<sub>2</sub>O</b> LOD [%]
MeOH 99.95%	2	0.0040	0.085	4.7	0.0098	0.085	4.8	0.0086	0.11	6.0
EtOH 99.5%	2	0.0036	0.02	1.7	0.0084	0.01	1.0	0.0084	0.05	3.2
THF 99.9%	5	0.0097	0.01	0.3	0.0084	0.015	0.4	0.0082	0.02	0.5
ACN 99.8%	5	0.0043	0.01	0.4	0.0118	0.01	0.4	0.0085	0.02	0.7

### 2.5.1. Sensing Studies on **CP1@3D**

To evaluate the water detection limit of the activated 3D printed composite objects, **CP1@3D**, and compare it with **CP1** and **CP1-H<sub>2</sub>O**, similar experiments have been carried out with **CP1@3D** using different dry organic solvents, i.e., ethanol 99.5%, methanol 99.95%, tetrahydrofuran 99.9%, and acetonitrile 99.8% (Figure 11). The data obtained (Table 1) show that the new 3D printed objects (**CP1@3D**) have a detection capacity very similar to that of **CP1**, with the advantage that we can adapt its form to any shape of device.

The color change of the **CP1@3D** from blue to violet has been obtained always even after 20 heating cycles at 60 °C and air cooling; powder X-ray diffraction spectra confirm the stability of the compound (Figure S7, Supporting Information).

As for the powdered samples, we performed the study in a dry box in order to evaluate the ability to detect the relative humidity of the air with the 3D printed material. In this case, the printed material seems to be more sensitive than the **CP1**, detecting relative humidity below 6.5%. This is probably due to the fact that the new 3D printed material is a composite composed of an organic matrix of glycolic nature, with certain hygroscopic character and porosity. This evidence could explain that the color change from violet to blue occurs faster for **CP1@3D** than for pristine **CP1-H<sub>2</sub>O**.

## 3. Conclusions

We have previously shown the potential biological interest of  $[\text{Cu}(\text{TAcO})_2(4,4'\text{-bipy})(\text{H}_2\text{O})]_n \cdot 2\text{H}_2\text{O}$  because of the presence of the thymine moiety along the chains of this coordination polymer and the simple way to produce nanofibers of this material in a one-pot procedure.<sup>[13]</sup> Now we show the ability of **CP1** to selectively lose water molecules from its structure and generate two new CPs. In the first step, at moderate temperature (60 °C) or under vacuum, **CP1** releases one water molecule with a significant change in color, from blue to violet, reversibly, giving rise to the formation of **CP1-H<sub>2</sub>O**. Although it is counterintuitive, the first water molecule that is released in this process is the one coordinated to the copper atom in **CP1**. This process has been carefully analyzed with the help of theoretical calculations and advanced X-ray techniques.

We have confirmed the use of this reversible thermochromic transformation, from **CP1** to **CP1-H<sub>2</sub>O**, to detect moisture in air and solvents. In addition, the easy preparation of **CP1** in colloidal form as nanofibers has enabled its formulation as inks that can be 3D printed. This enables us to fabricate **CP1@3D** in a variety of architectures, useful for detection of moisture in several organic solvents. It is remarkable that 3D printing of **CP1@3D** may allow the production of almost any desired shape required for a given application and fabricate different devices.

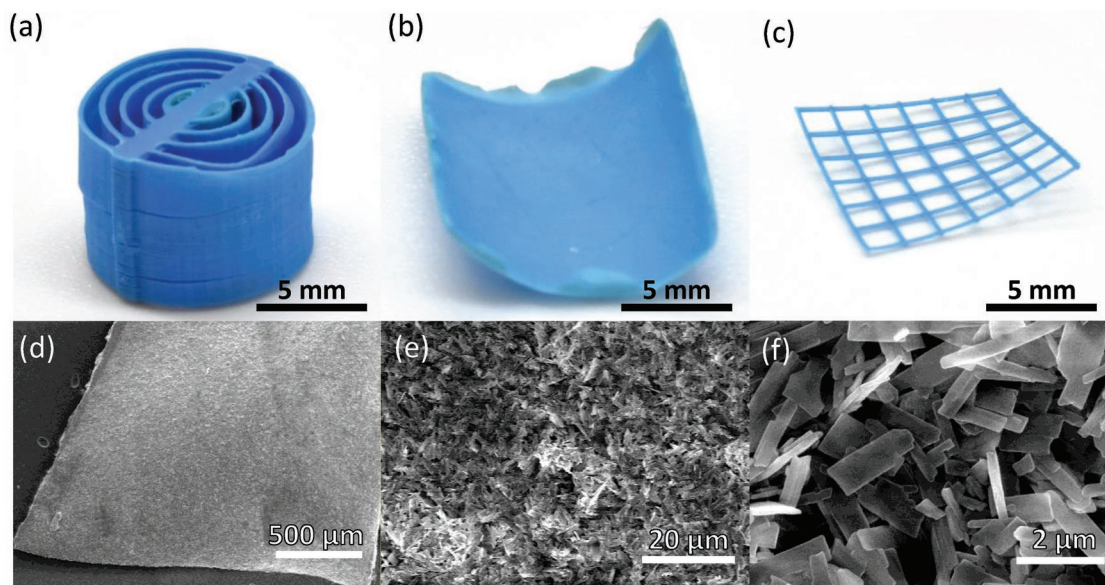


**Figure 10.** a–c) Different 3D printed **CP1@3D** architectures. d–f) SEM images of the 3D printed material by extruding printer, **CP1** crystals with the polymeric matrix (**CP1@3D**), and the 40 wt% **CP1** sample.



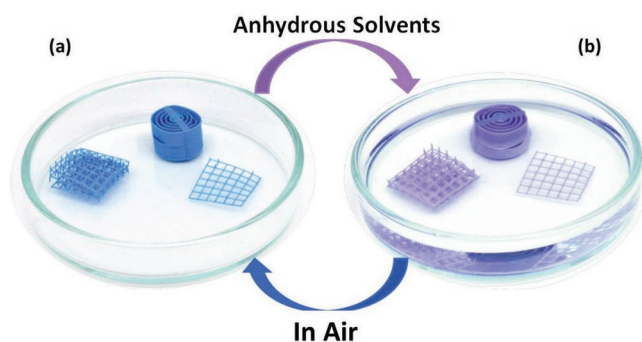


**Figure 11.** a) Different architectures of the 3D printed material (**CP1@3D**) in air at 25 °C (blue color). b) **CP1@3D** introduced in dry solvents such as ethanol, methanol, tetrahydrofuran, or acetonitrile showing the characteristic violet color.

This work shows the first 3D printed composite objects created from a nonporous coordination polymer and opens the door to the use of this large family of compounds that are easy to synthesize and exhibit interesting magnetic, conductive, and optical properties, in the field of functional 3D printing.

## 4. Experimental Section

**Materials and Methods:** All reagents and solvents were purchased from standard chemical suppliers: thymine-1-acetic (TAcOH) acid 98%, Sigma-Aldrich; 4,4'-bipy 98%, Sigma-Aldrich; copper nitrate trihydrate extra pure, Scharlab; potassium hydroxide, Scharlab; DPGDA (SR-508), Sartomer; ethoxylated trimethylolpropane triacrylate (SR-9035), Sartomer; DM ≥99.0%, Sigma-Aldrich; Irgacure 819, BASF; Irgacure 184, BASF; EtOH (99.5%), MeOH (99.95%), CH<sub>3</sub>CN (99.8%), and THF (99.9%) and used as received.

IR spectra were recorded on a PerkinElmer 100 spectrophotometer using a PIKE Technologies MIRacle Single Reflection Horizontal ATR Accessory from 4000 to 600 cm<sup>-1</sup>.

Elemental analysis was performed on an elementary microanalyzer LECO CHNS-932. It works with controlled doses of O<sub>2</sub> and a combustion temperature of 1000 °C.

Powder X-ray diffraction was collected using two different equipments. The first one was a PANalytical X'Pert PRO MPD  $\theta/2\theta$  secondary monochromator and detector with fast X'Celerator, which was used to general assays. The second one was a PANalytical X'Pert PRO ALPHA1  $\theta/2\theta$  primary monochromator and detector with fast X'Celerator, which was used to analyze immersed samples in a solvent or under an inert atmosphere. The immersed samples were prepared on a silicon sample holder and covered with a sheet of Kapton and the samples under nitrogen were prepared on a silicon sample holder too with polycarbonate sealing cap. Theoretical X-ray powder diffraction patterns were calculated using Mercury Cambridge Structural Database (CSD) version 3.10 software from the Crystallographic Cambridge Database. The samples were analyzed with scanning  $\theta/2\theta$ .

TGA was performed on a TGA Q500 Thermobalance with an evolved gas analysis furnace and mass spectrometer Thermostat Pfeiffer of Tecnovac, to analyze gases that are given off from the sample. The powder sample was analyzed using a Pt sample holder and O<sub>2</sub> flow as purge gas of 90 mL min<sup>-1</sup> with a heating ramp from room temperature to 1000 °C at 10 °C min<sup>-1</sup>.

DSC was performed on a Discovery DSC. The sample was analyzed using hermetic aluminum pans from 20 to 200 °C in a N<sub>2</sub> atmosphere with two heating rate of 5 and 10 °C min<sup>-1</sup>.

Field emission scanning electron microscopy images were recorded on a Philips XL30 S-FEG field emission scanning electron microscope and on Carl Zeiss SUPRA 55 scanning electron microscope.

Diffuse reflectance studies were conducted on a StellarNet spectrophotometer model Blue-Wave, with internal slot of 25  $\mu$ m and diffraction network of 600 lines mm<sup>-1</sup>, equipped with fiberglass both for illumination and for capturing the reflected light. With diffuse reflectance probe R400-7-VISNIR and StellarNet lamp light source model SL1 and white RS50 reflectance pattern from StellarNet. Range of wavelengths was 350–2200 nm.

The diffuse reflectance measurements were taken in a 45°/45° illumination/detection configuration, with respect to the sample surface. Each measurement consisted of an average of 5 spectra of 200 ms; five different measurements were made, so that each signal was composed of the average of 25 spectra of 200 ms. The software used to make the measurements was SpectraWiz program & apps, from StellarNet. Diffuse reflectance measurements were represented by two graphs, the reflectance (% diffuse reflectance) and the remission function ( $F(\text{diffuse reflectance})$ ) versus wavelength. The remission function was determined by the Kubelka–Munk equation. The collected data were treated with Origin 9.0 to get to the graphic representations that appear in Figure S6 in the Supporting Information.

Synchrotron X-ray total scattering data suitable for PDF analyses were collected at the P02.1 beamline at PETRA III using 60 keV (0.207 Å) X-rays. Samples were loaded into borosilicate capillaries and sealed using epoxy. Data were collected using an amorphous silicon-based PerkinElmer area detector. Geometric corrections and reduction to 1D data used DAWN Science software.<sup>[25]</sup> PDFs were obtained from the data within PDFget3<sup>[26]</sup> within xPDFsuite to a  $Q_{\text{max}} = 17 \text{ Å}^{-1}$ . Cu–N, O correlations of interest were quantified by fitting Gaussian functions.

**Theoretical Modeling and Computational Details:** All the first-principles simulations were performed by using DFT as implemented in the CASTEP simulation package.<sup>[27]</sup> Exchange–correlation interactions were accounted by the generalized gradient approximation within the Perdew–Burke–Ernzerhof functional,<sup>[28]</sup> which were based on a total energy pseudopotential plane-wave framework.<sup>[29]</sup> The Vanderbilt ultrasoft pseudopotential scheme was adopted to model the ion–electron interactions, and the valence atomic configurations considered were the following: H, 1s<sup>1</sup>; C, 2s<sup>2</sup>2p<sup>2</sup>; N, 2s<sup>2</sup>2p<sup>3</sup>; O, 2s<sup>2</sup>2p<sup>4</sup>; and Cu, 3d<sup>10</sup>4s<sup>1</sup>. The cutoff energy was set to 380 eV; an optimal  $k$ -point mesh of  $6 \times 3 \times 1$  and a self-consistent field of  $1 \times 10^{-6}$  eV per atom were used for geometry optimizations using the Monkhorst–Pack scheme.<sup>[30]</sup> Full geometry optimizations, where all the atoms were free to relax, were carried out before single-point energy calculations and the final net force acting on each atom was less than  $0.05 \text{ eV Å}^{-1}$ ; the final stress on the atoms was below 0.05 GPa. Transition-state barriers were computed within the CI-NEB approach,<sup>[31]</sup> where the initial and final steps, as well as a sufficient number of intermediate images (20 in this case), were permitted to fully relax to achieve a converged MEP. To check the reliability of the results, additional test calculations with a higher plane-wave cutoff energy and a denser  $k$ -point grid were performed, yielding no significant changes for both geometric and electronic structures, and obtaining differences between total energies <0.02%, which justifies the validity of our calculations. The theoretical crystal–powder diffractograms were simulated from the DFT-optimized structures by using the MERCURY package.<sup>[32]</sup>

**Synthesis of [Cu(TAcO)<sub>2</sub>(4,4'-bipy)(H<sub>2</sub>O)]<sub>n</sub>·2H<sub>2</sub>O (**CP1**) and **CP1@135 °C**:** The synthesis of coordination polymer **CP1** has already been reported by Vegas et al.<sup>[13]</sup>

**CP1@135 °C** was obtained by heating **CP1** during 20 min at 135 °C; the newly emerged structure was characterized by IR selected data (cm<sup>-1</sup>): 3165 (w), 3050 (w), 2823 (w), 1689 (s), 1612 (s), 1630 (m), 1463 (m), 1418 (m), 1377 (m), 1300 (m), 1278 (m), 1246 (m), 1228 (m); and elementary analysis for C<sub>24</sub>H<sub>22</sub>CuN<sub>6</sub>O<sub>8</sub>, Calcd. (Found): %C, 49.2 (48.9); %N, 14.3 (14.2); %H, 3.8 (3.9).

**Preparation of the Printing Formulation:** 1) 10 wt%—[Cu(TAcO)<sub>2</sub>(4,4'-bipy)(H<sub>2</sub>O)]<sub>n</sub>·2H<sub>2</sub>O (2 g) was mixed with DPGDA (9 g), Sr-9035 (9 g), and DM (4 g) as a solvent. To form a homogeneous dispersion, the mixture was sonicated with a tip sonicator (Sonics Vibra-cell, 500 W) for 45 min (1 s on, 2 s off) and 50% amplitude. Following

this, photoinitiators, Irgacure 819 (0.16 g) and Irgacure 184 (0.32 g), were dissolved in the dispersion. 2) 40 wt%—[Cu(TAcO)<sub>2</sub>(4,4'-bipy)(H<sub>2</sub>O)]<sub>n</sub>·2H<sub>2</sub>O (2.26 g) was mixed with DPGDA (1.65 g), SR-9035 (1.65 g), and DM (4.44 g) as a solvent. To form a homogeneous dispersion, the mixture was mixed with a homogenizer (IKA T25) for 5 min and 5000 rpm. Following this, photoinitiators, Irgacure 819 (0.07 g) and Irgacure 184 (0.14 g), were dissolved in the dispersion.

**3D Printing of [Cu(TAcO)<sub>2</sub>(4,4'-bipy)(H<sub>2</sub>O)]<sub>n</sub>·2H<sub>2</sub>O (CP1@3D) Embedded with Polymeric Structures:** The models containing 10 wt% [Cu(TAcO)<sub>2</sub>(4,4'-bipy)(H<sub>2</sub>O)]<sub>n</sub>·2H<sub>2</sub>O were printed with a DLP 3D printer (Asiga Pico2) (Scheme S1a, Supporting Information). The models containing 40 wt% [Cu(TAcO)<sub>2</sub>(4,4'-bipy)(H<sub>2</sub>O)]<sub>n</sub>·2H<sub>2</sub>O were printed with an extruding 3D printer (Hyrel System 30M) (Scheme S1b, Supporting Information). In both printers, the polymerization was initiated by UV light, with a wavelength of 400–405 nm. Following the printing process, the objects were washed with isopropyl alcohol to remove the unpolymerized residues.

## Supporting Information

Supporting Information is available online from the Wiley Online Library or from the author.

## Acknowledgements

N.M. and V.G.V. contributed equally to this work. The authors thank financial support from the Spanish Ministerio de Economía y Competitividad (MAT2016-77608-C3-1-P, MAT2016-75883-C2-2-P) and the National Research Foundation, Prime Minister's Office, Singapore, under its Campus for Research Excellence and Technological Enterprise (CREATE) programme. O.H. acknowledges the support for Ph.D. students from The Hebrew University of Jerusalem. J.I.M. acknowledges the financial support by the "Ramón y Cajal" Program of MINECO (Grant RYC-2015-17730) and the EU via the ERC-Synergy Program (Grant ERC-2013-SYG-610256 NANOCOSMOS). A.E.P.-P. acknowledges a TALENTO grant (2017-T1/IND5148) from Comunidad de Madrid. The authors acknowledge DESY (Hamburg, Germany), a member of the Helmholtz Association HGF, for the provision of experimental facilities. Parts of this research were carried out at beamline P02.1 PETRA III under the proposal I-20170717 EC. V.G.V. thanks to the Ministry of Education, Youth and Sports, the Madrid Community and the European Social Fund. The authors thank Deseada Diaz Barrero, from Autonoma University of Madrid, Applied Physics Department, for the study of diffuse reflectance of the compound presented here.

## Conflict of Interest

The authors declare no conflict of interest.

## Keywords

3D printing, coordination polymers, sensing, solvato-thermochromic, water detection

Received: November 27, 2018

Revised: January 31, 2019

Published online: February 14, 2019

- [1] a) L. Pugliese, S. Marconi, E. Negrello, V. Mauri, A. Peri, V. Gallo, F. Auricchio, A. Pietrabissa, *Updates Surg.* **2018**, 70, 381; b) M. Kuehnelt, T. Froehlich, R. Fuessl, M. Hoffmann, E. Manske, I. W. Rangelow, J. Reger, C. Schaeffell, S. Sinzinger, J. P. Zoellner,

- Meas. Sci. Technol.* **2018**, 29, 114002; c) Z. Zhu, S. Z. Guo, T. Hirdler, C. Eide, X. Fan, J. Tolar, M. C. McAlpine, *Adv. Mater.* **2018**, 30, 1707495; d) H. Yuan, K. Xing, H. Y. Hsu, *Bioengineering* **2018**, 5, 57; e) W. Gutierrez-Sandi, T. Lemos-Pires, G. Carlo Galiano-Murillo, J. Alejandro Madrigal-Lobo, *Tecnol. Marcha* **2018**, 31, 131.
- [2] a) K. D. Roehm, S. V. Madhally, *Biofabrication* **2017**, 10, 015002; b) S. T. Bendtsen, M. Wei, *J. Biomed. Mater. Res. A* **2017**, 105, 3262; c) H. Ma, J. Luo, Z. Sun, L. Xia, M. Shi, M. Liu, J. Chang, C. Wu, *Biomaterials* **2016**, 111, 138.
- [3] a) E. J. Mott, M. Busso, X. Luo, C. Dolder, M. O. Wang, J. P. Fisher, D. Dean, *Mater. Sci. Eng. C* **2016**, 61, 301; b) A. Al Mousawi, F. Dumur, P. Garra, J. Toufaily, T. Hamieh, F. Goubard, B. Thanh-Tuan, B. Graff, D. Gigmes, J. P. Fouassier, J. Lalevee, *J. Polym. Sci., Part A: Polym. Chem.* **2017**, 55, 1189; c) S. J. Lee, D. Lee, T. R. Yoon, H. K. Kim, H. H. Jo, J. S. Park, J. H. Lee, W. D. Kim, I. K. Kwon, S. A. Park, *Acta Biomater.* **2016**, 40, 182.
- [4] X. Li, Y. Wang, Z. Wang, Y. Qi, L. Li, P. Zhang, X. Chen, Y. Huang, *Macromol. Biosci.* **2018**, 18, 1800068.
- [5] a) P. Li, H. Yu, N. Liu, F. Wang, G. B. Lee, Y. Wang, L. Liu, W. J. Li, *Biomater. Sci.* **2018**, 6, 1371; b) O. Halevi, J. M. R. Tan, P. S. Lee, S. Magdassi, *Adv. Sustainable Syst.* **2018**, 2, 1700150.
- [6] a) J. Troyano, O. Castillo, J. I. Martínez, V. Fernández-Moreira, Y. Ballesteros, D. Maspocho, F. Zamora, S. Delgado, *Adv. Funct. Mater.* **2018**, 28, 1704040; b) J. Conesa-Egea, J. Gallardo-Martínez, S. Delgado, J. I. Martínez, J. Gonzalez-Platas, V. Fernández-Moreira, U. R. Rodríguez-Mendoza, P. Ocón, F. Zamora, P. Amo-Ochoa, *Small* **2017**, 13, 1700965; c) J. Conesa-Egea, N. Nogal, J. I. Martínez, V. Fernández-Moreira, U. R. Rodríguez-Mendoza, J. González-Platas, C. J. Gómez-García, S. Delgado, F. Zamora, P. Amo-Ochoa, *Chem. Sci.* **2018**, 9, 8000.
- [7] a) J. C. Lai, L. Li, D. P. Wang, M. H. Zhang, S. R. Mo, X. Wang, K. Y. Zeng, C. H. Li, Q. Jiang, X. Z. You, J. L. Zuo, *Nat. Commun.* **2018**, 9, 2725; b) L. Shi, H. Carstensen, K. Hoelzl, M. Lunzer, H. Li, J. Hilborn, A. Ovsianikov, D. A. Ossipov, *Chem. Mater.* **2017**, 29, 5816.
- [8] a) H. Thakkar, S. Eastman, Q. Al-Naddaf, A. A. Rownaghi, F. Rezaei, *ACS Appl. Mater. Interfaces* **2017**, 9, 35908; b) M. C. Kreider, M. Sefa, J. A. Fedchak, J. Scherschligt, M. Bible, B. Natarajan, N. N. Klimov, A. E. Miller, Z. Ahmed, M. R. Hartings, *Polym. Adv. Technol.* **2018**, 29, 867.
- [9] J. Deng, F. Wu, P. Yu, L. Mao, *Appl. Mater. Today* **2018**, 11, 338.
- [10] O. S. Wenger, *Chem. Rev.* **2013**, 113, 3686.
- [11] a) H. Hosokawa, T. Mochida, *Langmuir* **2015**, 31, 13048; b) S. S. Nagarkar, S. K. Ghosh, *J. Chem. Sci.* **2015**, 127, 627; c) S.-i. Noro, N. Yanai, S. Kitagawa, T. Akutagawa, T. Nakamura, *Inorg. Chem.* **2008**, 47, 7360.
- [12] A. Douvali, A. C. Tsepis, S. V. Eliseeva, S. Petoud, G. S. Papaefstathiou, C. D. Malliakas, I. Papadas, G. S. Armatas, I. Margiolaki, M. G. Kanatzidis, T. Lazarides, M. J. Manos, *Angew. Chem., Int. Ed.* **2015**, 54, 1651.
- [13] V. G. Vegas, R. Lorca, A. Latorre, K. Hassanein, C. J. Gómez-García, O. Castillo, Á. Somoza, F. Zamora, P. Amo-Ochoa, *Angew. Chem., Int. Ed.* **2017**, 56, 987.
- [14] M. G. Amiri, H. Golchoubian, *J. Mol. Struct.* **2018**, 1165, 196.
- [15] a) A. Kobayashi, H. Hara, S.-i. Noro, M. Kato, *Dalton Trans.* **2010**, 39, 3400; b) H. Hara, A. Kobayashi, S.-i. Noro, H. C. Chang, M. Kato, *Dalton Trans.* **2011**, 40, 8012; c) A. Dey, A. Garai, V. Gude, K. Biradha, *Cryst. Growth Des.* **2018**, 18, 6070.
- [16] C. Näther, J. Greve, I. Jeß, *Chem. Mater.* **2002**, 14, 4536.
- [17] A. E. Platero-Prats, A. Mavrandonakis, L. C. Gallington, Y. Liu, J. T. Hupp, O. K. Farha, C. J. Cramer, K. W. Chapman, *J. Am. Chem. Soc.* **2016**, 138, 4178.
- [18] C. Harris, *Talanta* **1972**, 19, 1523.
- [19] a) Y. Sadaoka, M. Matsuguchi, Y. Sakai, *Sens. Actuators A: Phys.* **1991**, 26, 489; b) Y. Itagaki, S. Nakashima, Y. Sadaoka, *Sens. Actuators*

- B: *Chem.* **2009**, 142, 44; c) S. Sohrabnezhad, A. Pourahmad, M. A. Sadjadi, *Mater. Lett.* **2007**, 61, 2311; d) N. A. Luechinger, S. Loher, E. K. Athanassiou, R. N. Grass, W. J. Stark, *Langmuir* **2007**, 23, 3473; e) D. Bridgeman, J. Corral, A. Quach, X. Xian, E. Forzani, *Langmuir* **2014**, 30, 10785.
- [20] E. Kim, S. Y. Kim, G. Jo, S. Kim, M. J. Park, *ACS Appl. Mater. Interfaces* **2012**, 4, 5179.
- [21] J. C. Tellis, C. A. Strulson, M. M. Myers, K. A. Kneas, *Anal. Chem.* **2011**, 83, 928.
- [22] a) C. P. L. Rubinger, C. R. Martins, M. A. De Paoli, R. M. Rubinger, *Sens. Actuators B: Chem.* **2007**, 123, 42; b) Y. Li, M. J. Yang, N. Carnaioni, G. Casalbore-Miceli, *Sens. Actuators B: Chem.* **2001**, 77, 625; c) K. S. Chou, T. K. Lee, F. J. Liu, *Sens. Actuators B: Chem.* **1999**, 56, 106; d) M. M. F. Choi, O. Ling Tse, *Anal. Chim. Acta* **1999**, 378, 127; e) Z. Wang, J. Zhang, J. Xie, C. Li, Y. Li, S. Liang, Z. Tian, T. Wang, H. Zhang, H. Li, W. Xu, B. Yang, *Adv. Funct. Mater.* **2010**, 20, 3784; f) M. M. Hawkeye, M. J. Brett, *Adv. Funct. Mater.* **2011**, 21, 3652.
- [23] a) K. Müller-Buschbaum, F. Beuerle, C. Feldmann, *Microporous Mesoporous Mater.* **2015**, 216, 171; b) Y. Yu, J. P. Ma, Y. B. Dong, *CrystEngComm* **2012**, 14, 7157; c) Z. Hu, B. J. Deibert, J. Li, *Chem. Soc. Rev.* **2014**, 43, 5815.
- [24] H. Golchoubian, R. Samimi, *Polyhedron* **2017**, 128, 68.
- [25] M. Basham, J. Filik, M. T. Wharmby, P. C. Y. Chang, B. El Kassaby, M. Gerring, J. Aishima, K. Levik, B. C. A. Pulford, I. Sikharulidze, *J. Synchrotron Radiat.* **2015**, 22, 853.
- [26] C. L. F. P. Juhás, T. Davis, S. J. L. Billinge, *J. Appl. Crystallogr.* **2013**, 46, 560.
- [27] M. D. Segall, J. D. L. Philip, M. J. Probert, C. J. Pickard, P. J. Hasnip, S. J. Clark, M. C. Payne, *J. Phys.: Condens. Matter* **2002**, 14, 2717.
- [28] J. P. Perdew, K. Burke, M. Ernzerhof, *Phys. Rev. Lett.* **1996**, 77, 3865.
- [29] D. Vanderbilt, *Phys. Rev. B* **1990**, 41, 7892.
- [30] H. J. Monkhorst, J. D. Pack, *Phys. Rev. B* **1976**, 13, 5188.
- [31] B. J. Berne, G. Cicotti, D. F. Coker, *Classical and Quantum Dynamics in Condensed Phase Simulations*, World Scientific, Singapore **1998**.
- [32] C. F. Macrae, I. J. Bruno, J. A. Chisholm, P. R. Edgington, P. McCabe, E. Pidcock, L. Rodriguez-Monge, R. Taylor, J. van de Streek, P. A. Wood, *J. Appl. Crystallogr.* **2008**, 41, 466.



# ADVANCED FUNCTIONAL MATERIALS

## Supporting Information

for *Adv. Funct. Mater.*, DOI: 10.1002/adfm.201808424

3D Printing of a Thermo- and Solvatochromic Composite  
Material Based on a Cu(II)–Thymine Coordination Polymer  
with Moisture Sensing Capabilities

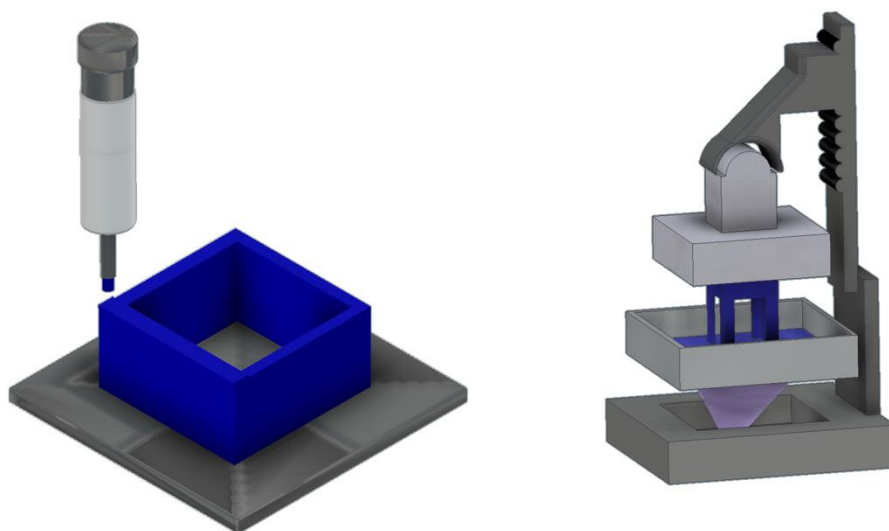
*Noelia Maldonado, Verónica G. Vegas, Oded Halevi, Jose  
Ignacio Martínez, Pooi See Lee, Shlomo Magdassi, Michael  
T. Wharmby, Ana E. Platero-Prats, Consuelo Moreno, Félix  
Zamora,\* and Pilar Amo-Ochoa\**



## Supporting Information

**3D printing of a thermo- and solvato-chromic composite material based on a Cu(II)-thymine coordination polymer with moisture sensing capabilities**

Noelia Maldonado, Verónica G. Vegas, Oded Halevi, Jose Ignacio Martinez, Pooi See Lee Shlomo Magdassi, Michael T. Wharmby, Ana E. Platero-Prats, Consuelo Moreno, Félix Zamora\* and Pilar Amo-Ochoa\*



**Scheme S1.** Operating scheme of a Digital Light Processing (DLP) printer. (a) Extruder 3D-printer (Hyrel System 30M). (b) Digital light processing (DLP) 3D-printer (Asiga Pico2)..

Its thermal study (**Figure S1**), shows a 1<sup>st</sup> stage at 60 °C probably indicative of the loss of one coordinated water molecule (obsd 2.58%, calcd 2.75%, the ionic current indicates that there is only water). At 135 °C we can observe a 2<sup>nd</sup> stage also indicative of the loss of probably two lattice solvation water molecules (obsd 5.47%, calcd 5.62%). The observed values are somewhat different than those calculated. However, in several DTA-TG experiments these values always differ slightly, which can be regarded to the preparation of the material.<sup>[16]</sup> From 140 °C to 500 °C, the next stages correspond to the loss of organic ligands, TAcO and 4,4'-bipy, as CO<sub>2</sub> and H<sub>2</sub>O gas.

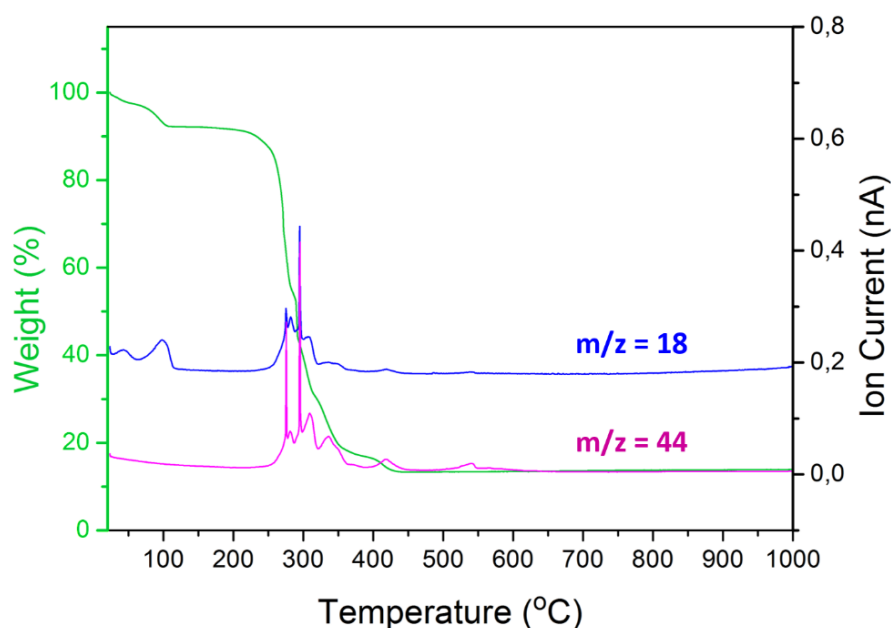


**Figure S1.** Thermal stability study of **CP1**. Signs of the thermogram: Green curve: represents the stages of the losses produced. Blue and pink curve: represent the ion currents corresponding to the masses 18 (blue) and 44 (pink) associated with each loss of the previous curves. Only those two are represented from a range of 0 to 200 u.m.a because there are no more significant signals.

In addition, DSC measurement, (**Figure S2**) was performed to clarify the order in which the water molecules leave the **CP1**, looking for a substantial difference in the bond breaking energies of the dehydration reaction and the possibility to obtain extra information from the structural change that occurs at 135 °C. For it, two assays were realized at different heating rates, (5 and 10 °C/min) from room temperature to 200 °C. It observes (Figure S2) that the first thermal event coincides with the TGA first step and this enthalpy is less than the second thermal event which also coincides with the TGA second step. These events occur at different temperatures depending on the heating rate, indicating the lability of the bond in the coordination water molecule.

However, these data don't allow to distinguish what molecules of water leave first, because the shape of the second event peak and the recovery of the baseline at the end indicate that this phenomenon contains overlapping between the energy of two water molecules loss and the energy reaction when a new structure emerges, which happens when the solvation water molecules are lost and depends on it kinetically and thermodynamically.

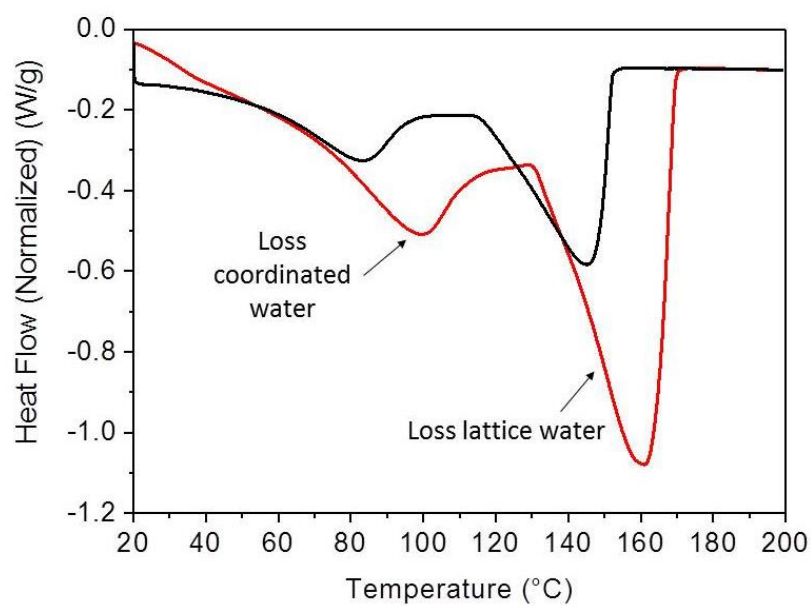


**Figure S2.** DSC curves of **CP1** at different heating rates.

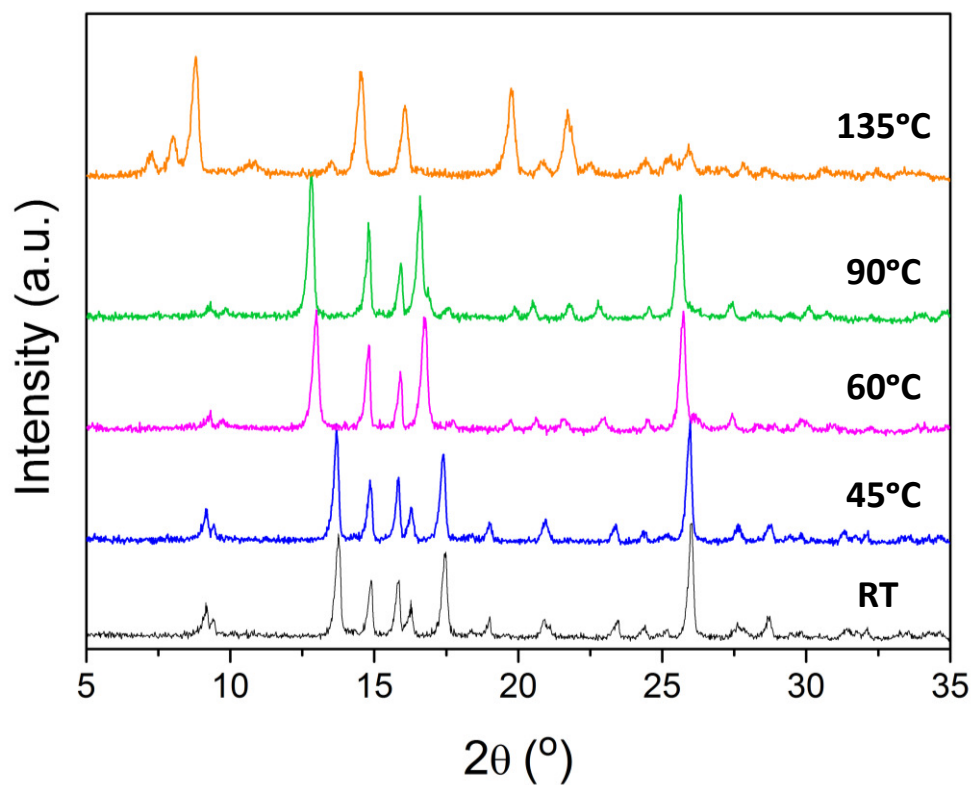


**Figure S3.** Powder XRD of **CP1** at different temperatures.

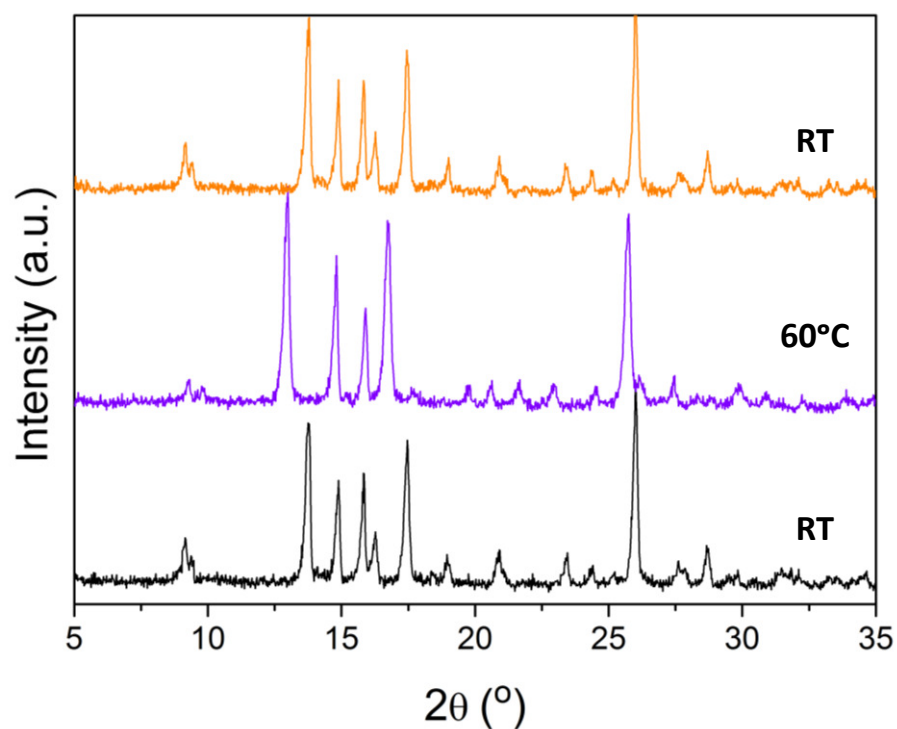


**Figure S4.** Powder XRD of **CP1** (black line) and **PC1-H<sub>2</sub>O** (purple line) and the reversibility process (orange line).

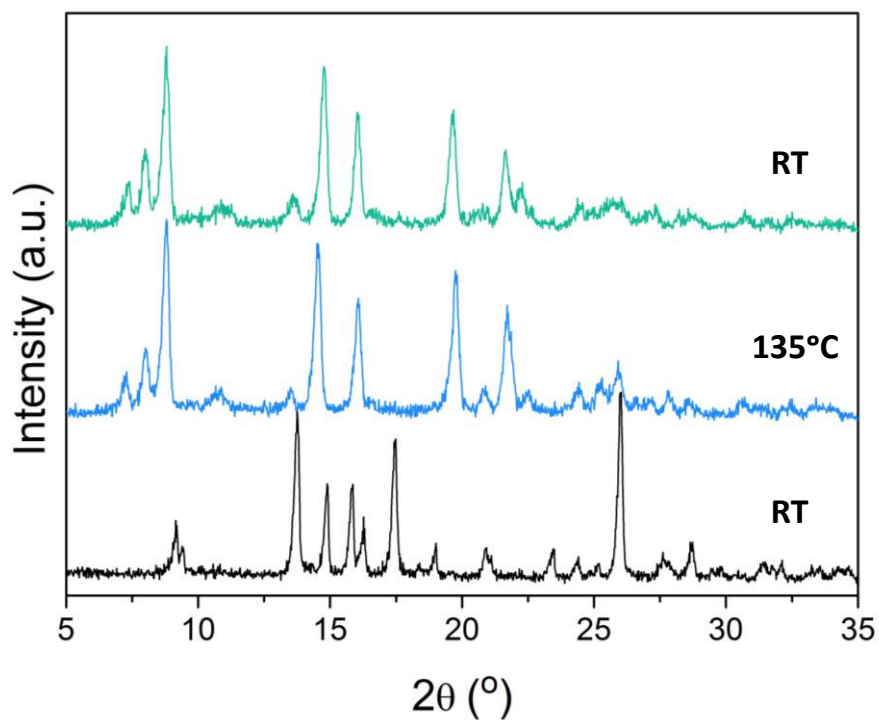


**Figure S5.** Powder XRD of **CP1** at 25 °C (black line) and 135 °C (blue line) showing the irreversibility of this process (green line).

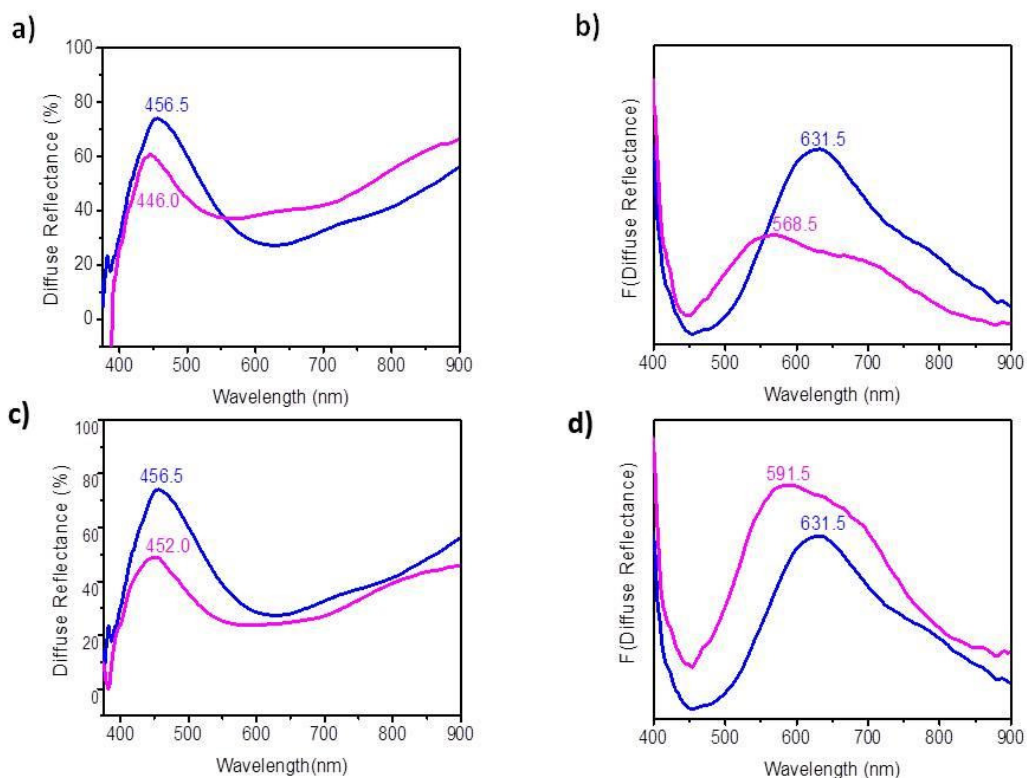


**Figure S6:** Diffuse reflectance (**a, c**) and the Kubelka-Munk (**b, d**), remission function spectrum obtained for **CP1**, before (initial, blue line) and after (final, violet line) be heated at 66.6 °C (**a** and **b**) and before (initial, blue line) and after (final, violet line) be immersed in dry methanol (MeOH) at 25 °C (**c** and **d**).

		Maximum Wavelength of Diffuse Reflectance (nm)		Maximum Wavelength of Kubelka-Munk (nm)	
	Change	Initial	Final	Initial	final
CP1	MeOH	456.5	452.0	631.5	591.5
CP1	66.6 °C	456.5	446.0	631.5	568.5

**Table S1:** Comparison of maximum wavelengths of both, the diffuse reflectance spectra and the Kubelka-Munk remission function of **CP1**, before (initial) and after (final) heating at 66.6 °C and before (initial) and after (final) being immersed in dry methanol (MeOH) at 25 °C.

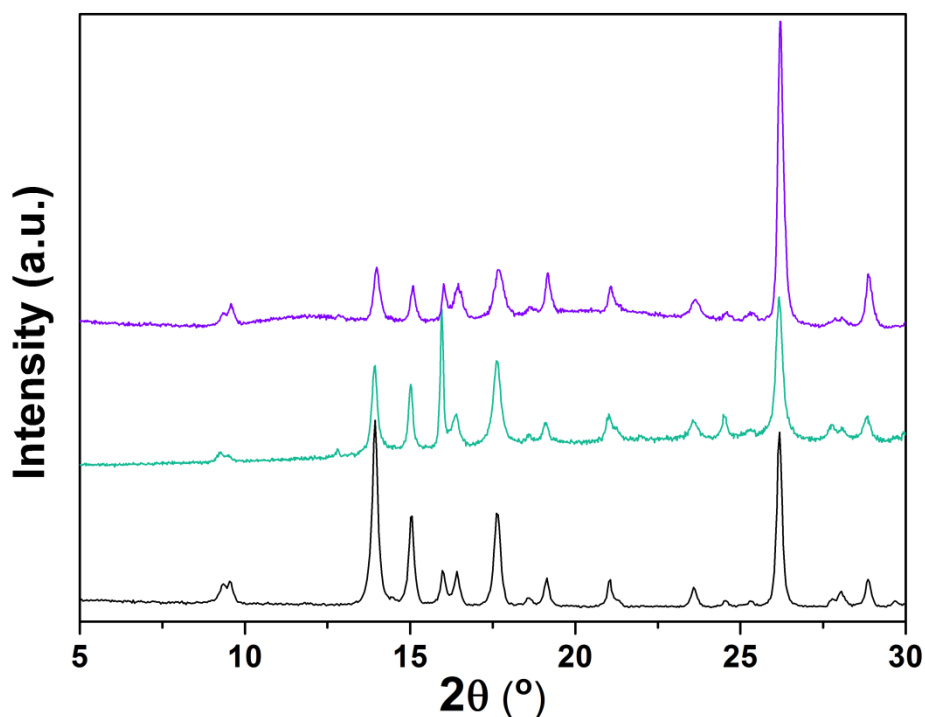


**Figure S7.** Simulated **CP1** (black line), experimental **CP1** (green line) and printed **CP1@3D** (purple line), X-ray powder diffractograms after 20 cycles applying 60°C and cooling o air.

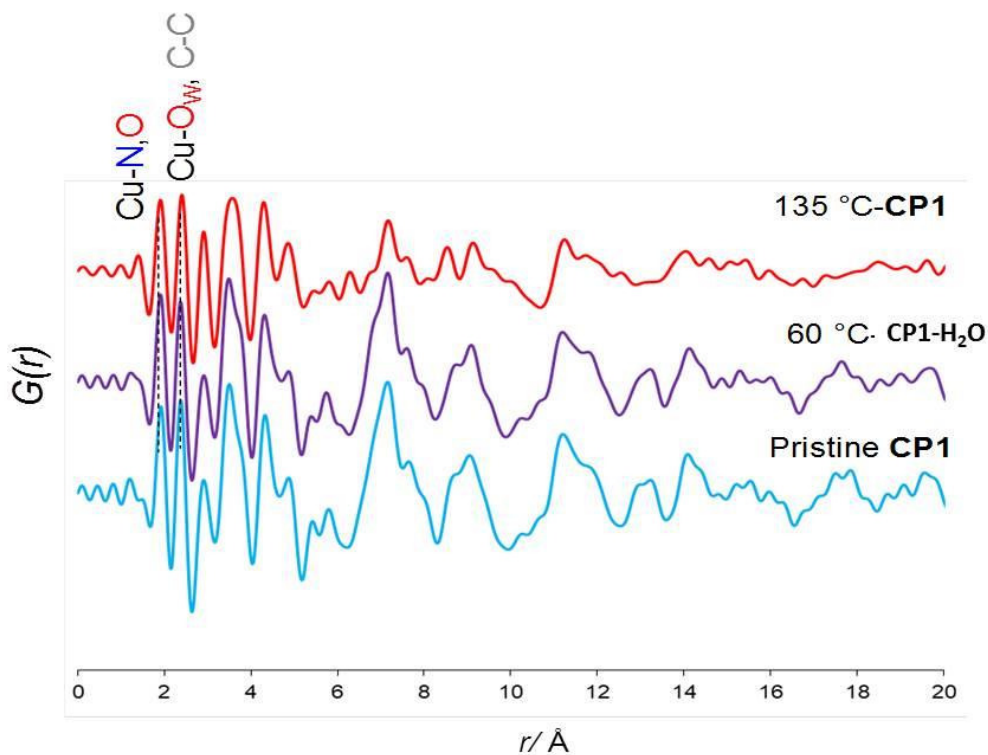


**Figure S8.** Experimental PDFs for **CP1** samples before and after heating at 60 and 135 °C, indicating the two peaks linked to the binding of the 4,4-bipy and TAcO ligands ( $\sim 2.0$  Å) and the water molecule ( $\sim 2.3$  Å).

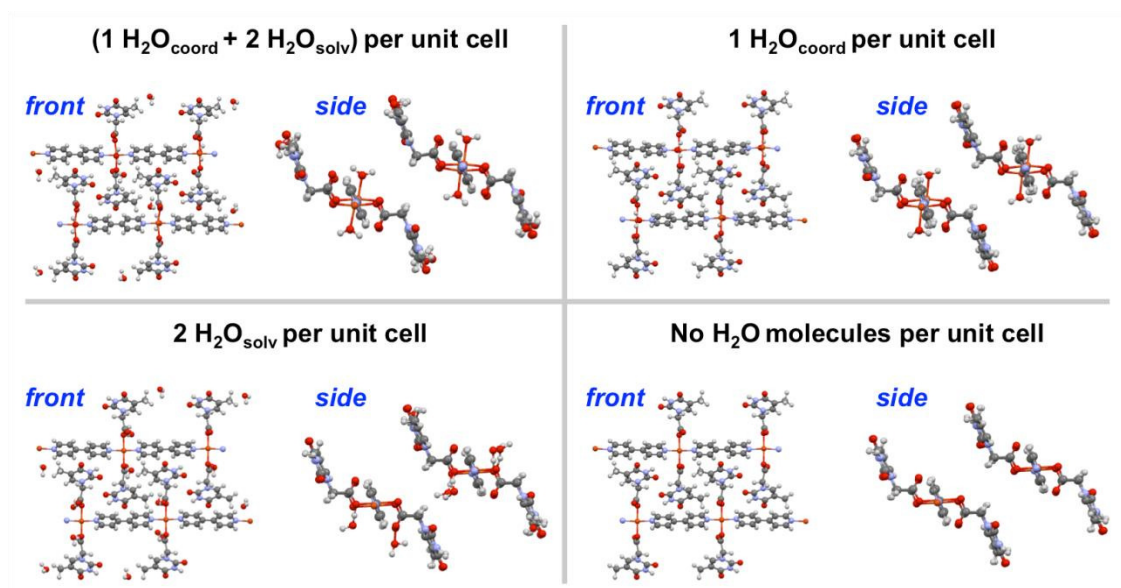


**Figure S9.** Front and side views of the computed optimal geometries for the compound **CP1**: (top-left) with 1 coordination and 2 solvation water molecules per unit cell, (top-right) with 1 coordination water molecule per unit cell, (bottom-left) with 2 solvation water molecules per unit cell, and (bottom-right) with no water molecules.



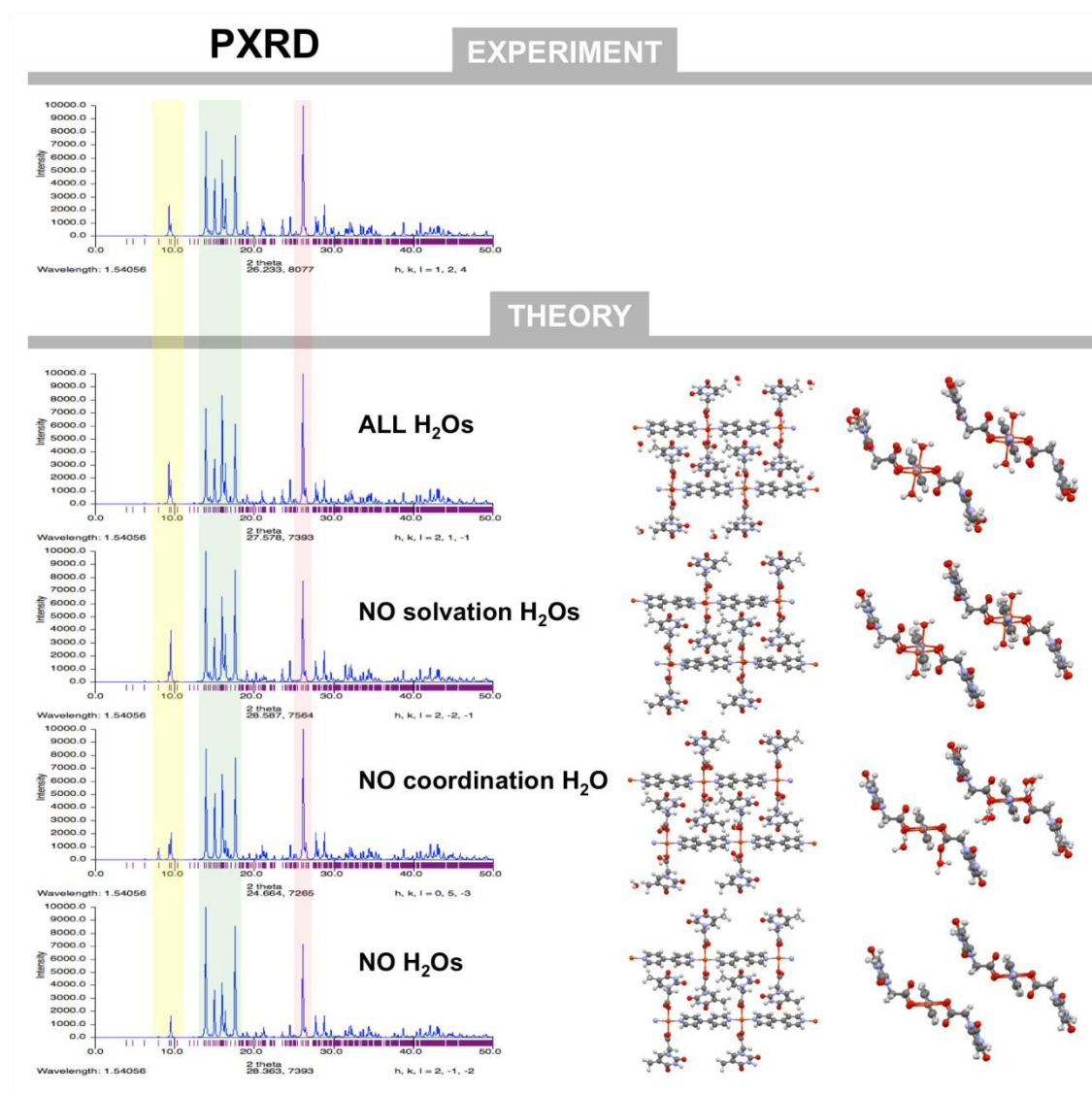


**Figure S10.** (Top panel) Experimental diffractogram for the **CP1** compound with 1 coordination and 2 solvation water molecules per unit cell. (Bottom panel) Simulated PXRD diffractograms from the DFT-optimized structures; front and side views of the structures have been included for each corresponding diffractogram. Color-shadowed stripes, overlapping all the PXRD spectra, have been also added highlighting the most representative regions.



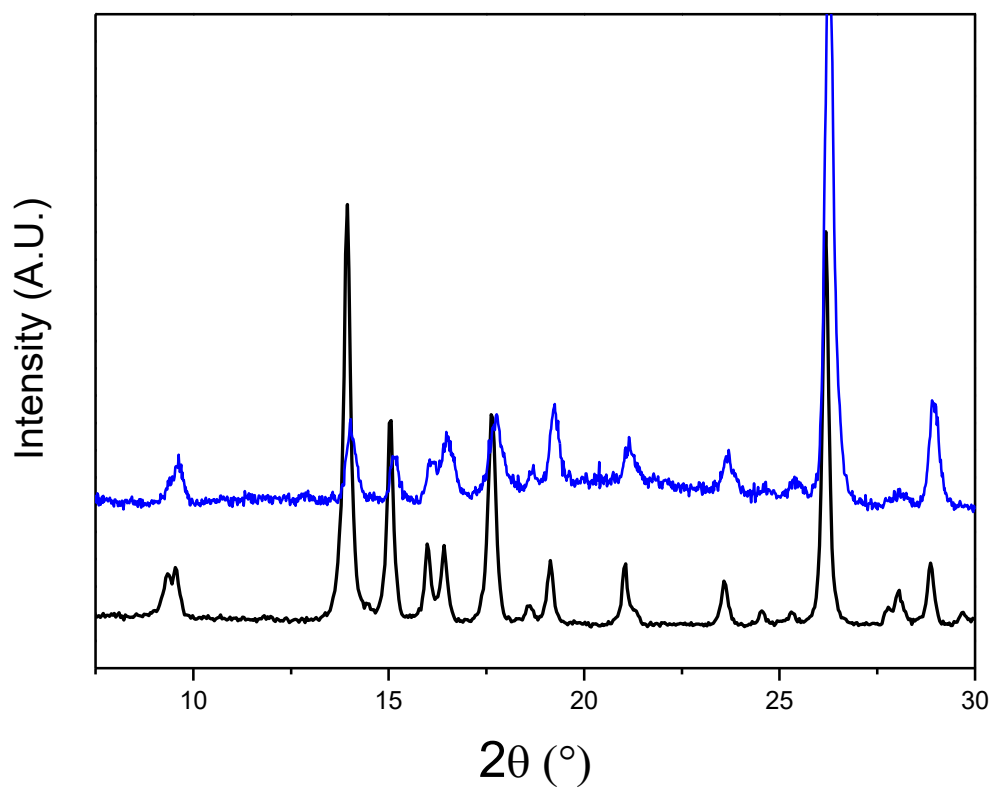


**Figure S11.** Powder X-ray diffractograms of the powder **CP1** (dark line) and the printed **CP1@3D** (blue line).

## תקציר

בשנים האחרונות, התחום העוסק בדפוזיציה (הנחה) נשלטת ומבוקרת של חומרים פונקציונליים נחקר והתפתח רבות. בתחום זה נכללות גם הדפסות הדו- והתלת-מימד (2D- and 3D-printing), אשר באמצעותן ניתן לייצר הדפסים ומבנים מוגדרים ותחומים של חומרים פונקציונליים, המיועדים לשימוש במגוון יישומים רחב. עד היום, מאמץ רב נעשה בפיתוח תהליכים ושיטות דפוזיציה מרמת הננו ועד המאקרו, וזאת משום שישנם חומרים רבים אשר הפונקציונליות שלהם מתאפשרת כאשר הם מצויים במבנים מסודרים ספציפיים. לדוגמא, גבישים יחידים, שכבות בהתארגנות-עצמית, או מבנים מולקולריים תלת-מימדיים.

קבוצת חומרים פונקציונאליים מעניינת היא החומרים הנקבוביים, אשר מאופיינים בערכי שטח פנים גבוהים ביותר, כתוצאה מקיומם של חללים בסדרי גודל של אנגסטרומים וננומטרים. שטח הפנים הגבוה מאפשר לעשות שימוש בחומרים אלה בתחומים כגון ספיחה של גזים ומולקולות קטנות לצרכי אחסון, זיהוי וגילוי, טיהור מים, חילופי-יונים, זירוז תגובות כימיות. במגוון החומרים שנכללים בקבוצה זו ניתן למצוא את הזאוליטים וה-metal organic frameworks (MOFs).

אחת מקבוצות החומרים הנקבוביים המבטיחות ביותר הינה ה-MOFs, אשר מהווה תת-קבוצה של הפולימרים הקואורניטיביים. חומרים אלו מורכבים מרשתות מולקולריות, אשר בנויות מיוני מתכות, המשמשים כ"צמתים", ומולקולות אורגניות אשר משמשות כ"לינקרים". על אף ההתקדמות המשמעותית במחקר וגילוי של תרכובות MOF חדשות בעשרים שנים האחרונות, השימוש שלהן בתעשייה עדיין לא נפוץ, עקב היציבות המוגבלת של תרכובות אלו בתנאים כימיים ופיזיקליים שונים. לעומתם, הזאוליטים, אשר מבוססים על רשתות aluminosilicates המאוכלסות עם יונים שונים, מציגים עמידות גבוהה בתנאים שונים, ולכן כבר נעשה בהם שימוש רב בתעשייה למגוון מטרות. עם זאת, גם חומרים אלה מציגים מספר אתגרים, שכן הם מצויים בצורת אבקה, אשר מקשה על התאמתם לחלק מהיישומים.

זאוליטים ו-MOFs הינם לרוב בתצורה גבישית, ובעלי סידור מולקולרי מחזורי. תכונה זו מאפשרת את יצירת הנקבוביות בעלות הגדלים הקבועים, ותורמת רבות לפונקציונליות של חומרים אלו. ניתן למצוא חומרים רבים נוספים אשר מציגים תכונות מעניינות ופונקציונליות כאשר הם בצורת גבישים. דוגמא לכך היא קבוצת המולקולות האורגניות הקטנות המוליכות-למחצה. קבוצת חומרים זו מאופיינת במוליכות-למחצה גבוהה יותר כאשר הם בצורת גבישים יחידים, לעומת בצורת מיקרו- או ננוחלקיקים. תהליכי גיבוש לרוב דורשים זמן ומערכות יציבות עם מינימום תזוזה והפרעות. עקב כך, הניסיון לבצע תהליכים אלו בצורה נשלטת באמצעות הדפסה הנו מאתגר מאוד, שכן הדפסה הינה לרוב תהליך מהיר אשר דורש תזוזה תמידית של המערכת.

המטרה המרכזית של מחקר זה הייתה לפתח חומרים ושיטות להדפסה ודפוזיציה של חומרים פונקציונליים במבנים תחומים ומוגדרים ברמות המיקרו והמאקרו. על ידי זאת, ניתן יהיה להתגבר על חלק מהמגבלות של החומרים הפונקציונליים ולאפשר שימוש משמעותי יותר שלהם ביישומים שונים. לכן, מטרת המחקר כוללת היבטים של חקר חומרים, הדפסות תלת-מימד והדפסות דו-מימד.

## על כן, מטרת המחקר הן:

1. פיתוח חומרים ושיטות להדפסות תלת-מימד של חומרים פונקציונליים נקבוביים, כגון MOFs וזאוליטים, תוך שמירה על הפונקציונליות.
2. חקר חומרים ושיטה לשימוש במדפסת תלת-מימד ככלי לסינתזה של פולימרים קואורדינטיביים נקבוביים במבנים מוגדרים ותחומים.
3. פיתוח תהליך וחומרים לשימוש במדפסת הזרקת-דיו (inkjet-printing) לגידול גבישים של מולקולות אורגניות קטנות מוליכות למחצה במיקומים מוגדרים.

## תוצרי המחקר כוללים שלושה מאמרים שפורסמו בכתבי עת מדעיים, ומאמר נוסף שמצוי כעת בתהליך הגשה לפרסום.

בשני הפרקים הראשונים, המיקוד היה על תערובות הטרוגניות של חלקיקים איאורגניים של MOFs וזאוליטים, עם פולימרים אורגניים. **במאמר מספר 1**,<sup>66</sup> הוצגה ההדפסה בתלת מימד של ה-MOF הידוע Cu-BTC, אשר במהלכה עלו מספר אתגרים. ראשית, היה צורך למנוע את החסימה של הנקבוביות של ה-MOF ע"י המטריצה הפולימרית, ולשמור על המבנה הגבישי של ה-MOF. בנוסף, היה צורך להגביר את היציבות שלו במים. בכדי להתגבר על אתגרים אלה, לא נעשה שימוש בחומרים פעילי-שטח לייצוב הפורמולציה, על מנת להימנע מחסימת פורות ה-MOF. עקב כך, נבחר מונומר נוזלי עם מבנה דומה (מכיל קבוצות ארומטיות) לזה של מולקולות ה"לינקרים" של ה-MOF, וזאת על מנת להקל על הפיזור האחיד של ה-MOF במונומר. בנוסף, דבר זה איפשר את הנגישות של ה-MOF לסביבה, שכן המנעות משימוש בחומר פעיל-שטח הובילה לכך שבעת הפילמור התרחשה הפרדת פאזות ונוצר מבנה מוצק שבו מרבית ה-MOF מצוי על פני שטח המבנה ומרבית הפולימר מצוי בחלק הפנימי של המבנה. הגברה של יציבות ה-MOF במים התאפשרה על ידי שימוש במונומר הידרופובי, אשר לאחר הפילמור יצר מטריצה הידרופובית אשר הגנה על מרכז הנחשת היוני ממולקולות המים ומנעה את ההידרוליזה של ה-MOF לאורך זמן.

**מאמר מספר 2**<sup>67</sup> עסק בהדפסה של זאוליטים במבנים מוגדרים תלת-מימדיים, אשר אפשרו להתגבר על מספר אתגרים שמציבים הזאוליטים שבשימוש בתעשייה כיום, כמו טיפול במים המכילים חומרים רדיואקטיביים בתחנות כח גרעיניות. כיום משתמשים ב-Zeolite 4A ו-Chabazite למטרה זו, אך הם

מעלים מספר קשיים כתוצאה מהמצאותם בצורת אבקות. במאמר זה, לעומת מאמר מספר 1, לא היה קושי של רגישות למים, אולם היה צורך בריכוז משקלי גבוה בהרבה של החומר הפונקציונלי הנקבובי במבנה התלת-מימדי הסופי. לכן, השיקולים הכימיים שנלקחו בחשבון היו שונים מבמאמר הקודם. כמו שליטה בנקבוביות של המטריצה הפולימרית, ופיזור הזאוליט באופן אחיד במבנה התלת-מימדי. מדידות ספיחה שבוצעו הראו שלזאוליטים במבנים המודפסים הייתה יכולת ספיחה של  $^{137}\text{Cs}^+$  ו-  $^{90}\text{Sr}^{2+}$  הזזה לזו של הזאוליטים המקוריים בצורת אבקה. עבודה זו הינה הדוגמא הראשונה של הדפסת תלת-מימד של זיאוליטים לשימוש כמחליפי-יונים.

**במאמר מספר 3**, פותחה גישה חדשה של שימוש בתהליך הדפסה של קומפלקס קואורדינטיבי מסיס המשמש כמונומר לצורך סינתזה של פולימר קואורדינטיבי. בפרק זה נעשה לראשונה שימוש במדפסת תלת-מימד כמכשיר סינתזה והושגה שליטה על המבנה של החומר גם ברמת המאקרו, וגם ברמה המולקולרית. בנוסף, בניגוד לפולימר המוטמע עם MOF במאמר 1, במאמר זה הפולימר הקואורדינטיבי משמש כחומר המבני (המטריצה) והחומר הפעיל בו-זמנית. לשם כך, סונתז קומפלקס איאורגני בעל ליגנד מתפלמרות, nickel tetra-acrylamide, אשר שימש כמונומר, והומס באתאנול להכנת הפורמולציה להדפסה. לאחר הכנת הפורמולציה, הודפס המונומר באמצעות מדפסת תלת-מימד המבוססת על תהליך פוטופולימריזציה מקומי, Digital Light Processing (DLP), לקבלת הפולימר הקואורדינטיבי הרצוי. פולימר זה ונוספים שניתן להכין בשיטה זו עשויים להתאים ליישומים כגון זיהוי מולקולות קטנות, או כחלק מכלי ריאקציה עם קטליזה מובנית.

**במאמר מספר 4**,<sup>68</sup> המטרה הייתה לפתח חומרים ושיטה להדפסה של גבישים במקומות מוגדרים, ולשם כך נעשה שימוש בתמיסות המכילות פרקורסורים לגבישים ובמדפסת דו-מימד בשיטת הזרקת דיו, על מנת לשלוט בהרכבה העצמית הבינמולקולרית שמתרחשת בתהליך הגיבוש. השיטה התבססה על יצירת מבנים תחומים הידרופיליים כאזורי גיבוש, שהודפסו בשלב הקודם להדפסת תמיסת המוליך-למחצה ההידרופובית. בכדי לאפשר שליטה מירבית על תהליך גידול הגביש, הופרדו שלבי הגירעון והגידול של הגביש הבודד באמצעות גיאומטריות שונות של אזור הגיבוש ותזמון הדפסת תמיסת המוליך-למחצה.

לסיכום, תוצרי המחקר המרכזיים הינם:

1. פותחו חומרים ושיטה להדפסת תלת-מימד של מבנים מוגדרים בהם MOFs מוטמעים בתוך מטריצה פולימרית, תוך שמירה על הפונקציונליות והזמינות של ה-MOF והגברת היציבות שלו במים.

2. פותחו ונחקרו חומרים ושיטה להדפסה תלת-מימדית של מבנים מוגדרים בהם זאוליטים מוטמעים בתוך מטריצה פולימרית בריכוז משקלי גבוה יחסית ובזמינות גבוהה, תוך שמירה על יכולת ספיחת יונים ביחס לזאוליט כאבקה.

3. הושגה גישה חדשה לסינתזה באמצעות הדפסת תלת-מימד באמצעות אור של פולימרים קואורדינטיביים נקבוביים כמבנים תלת-מימדיים.

4. פותחה שיטה להדפסה של גבישים יחידים של מולקולות אורגניות קטנות מוליכות-למחצה, תוך שליטה במיקומם על פני הסובסטרט.

המכנה המשותף הבולט ביותר של הפרקים השונים בעבודה זו הוא השגת השליטה על הדפוזיציה והסידור של החומרים הפונקציונליים השונים במבנים תחומים ומוגדרים, בעזרת ההסתמכות על תהליכים כגון הפרדת-פאזות, פוטופולימריזציה ותהליכי גיבוש, המשולבים עם תהליכי הדפסת דו ותלת מימד.

# **הדפסת חומרים פונקציונליים במבנים דו מימדיים ותלת מימדיים**

חיבור לשם קבלת תואר דוקטור לפילוסופיה

מאת

**עודד הלוי**

הוגש לסנט האוניברסיטה העברית

ספטמבר, 2019



עבודה זו נעשתה בהדרכתם

**של פרופ' שלמה מגדסי (HJ) ופרופ' פואי סי לי (NTU)**





# **הדפסת חומרים פונקציונליים במבנים דו מימדיים ותלת מימדיים**

חיבור לשם קבלת תואר דוקטור לפילוסופיה

מאת

**עודד הלוי**

הוגש לסנט האוניברסיטה העברית

ספטמבר 2019